CPFD Modeling of a Novel Internally Circulating Bubbling Fluidized Bed for Chemical Looping Combustion

Christopher McIntyre

A thesis submitted in partial fulfillment of the requirements for the
Master's degree in Applied Sciences

Department of Biological and Chemical Engineering
Faculty of Engineering
University of Ottawa

Abstract

Pressurized chemical looping combustion (PCLC) is a promising next generation carbon capture technology which operates on the fundamentals of oxyfuel combustion to concentrate carbon dioxide in the flue gas stream. Oxygen is supplied through cyclic oxidation and reduction of a solid metal oxide between an air reactor and fuel reactor to prevent the direct contact of fuel and air. CanmetENERGY-Ottawa, in collaboration with Hatch Ltd., is designing a pilot scale PCLC system which uses ilmenite as the oxygen carrier and a novel fluidized bed design called the Plug Flow Internally-recirculating Reactor (PFIR). The PFIR consists of an annular bubbling fluidized region in which particles are circulated by angle jets through two reactive zones separated by baffles. The overall objective of this thesis was to provide key design parameters and insight for the construction of the pilot facility.

Experimental work was first conducted investigating the minimum fluidization velocity (U_{mf}), gas bubble size, and tube-to-bed heat transfer coefficients of different ilmenite particle size distributions (PSDs) at varying pressures up to 2000 kPa. The data was compared to a variety of literature correlations. The Saxena & Vogel (1977) constants for the Wen-Yu type correlations ($Re_{mf} = \sqrt{C_1^2 + C_2 Ar} - C_1$) resulted in the best fit for predicting the U_{mf} of the PSDs with Sauter mean diameters (SMD) less than 109 µm, while the Chitester *et al.* (1984) constants resulted in better predictions for the larger particle size distributions (SMD greater than 236 µm). Gas bubble size was found to be marginally impacted by pressure, with the Mori & Wen (1975) correlation best fitting the data. The heat transfer coefficient was found to also be marginally increased by pressure with the the Molerus *et al.* (1995) correlation matching the atmospheric data.

A computational particle fluid dynamic (CPFD) model of the experimental unit was then created and validated using the obtained data for minimum fluidization velocity and bubble size. The accuracy of the model was found to be dependent on the particle close packing factor input variable, with a value of 0.58 resulting in the best results for each of the ilmenite PSDs modeled.

Finally, a CPFD model was created for a cold flow design of the PFIR to investigate the impacts of different operating parameters on the solids circulation rate and gas infiltration rate between the two reactor zones. This model used the validated parameters of the previous CPFD model to add confidence to the results. The impacts of increasing superficial gas velocity, fluidizing gas jet velocity, bed height, and pressure were all found to increase the solids circulation rate through their respective impacts on the momentum rate of the fluidizing gas. A polynomial function was fit between these two variables resulting in a method to predict the solids circulation rate. Similarly, the rate of gas infiltration between sections was found to be dependent on the solids circulation rate, allowing for a function to be made to predict the gas infiltration at different operating conditions.

Sommaire

La combustion en boucle chimique sous pression (PCLC) est une technologie prometteuse de capture de carbone de nouvelle génération qui fonctionne sur les principes fondamentaux de l'oxycombustion pour concentrer le dioxyde de carbone dans les gaz de combustion. L'oxygène est fourni par oxydation et réduction cyclique d'un oxyde métallique solide entre un réacteur à air et un réacteur à combustible pour empêcher le contact direct du combustible et de l'air. CanmetÉNERGIE-Ottawa, en collaboration avec Hatch Ltd., conçoit un système PCLC à l'échelle pilote qui utilise l'ilménite comme transporteur d'oxygène et une nouvelle conception de lit fluidisé appelée réacteur à recirculation interne à écoulement piston (PFIR). Le PFIR consiste en une région annulaire, fluidisée dans le régime à bulles, dans laquelle les particules sont mises en circulation par des jets angulaires à travers deux zones réactives séparées par des chicanes. L'objectif général de cette thèse était de fournir des paramètres de conception clés et des informations pour la construction de l'installation pilote.

Des travaux expérimentaux ont d'abord été menés pour étudier la vitesse de fluidisation minimale (U_{mf}), la taille des bulles de gaz et les coefficients de transfert de chaleur tube-lit de différentes distributions de tailles d'ilménite (PSD) à des pressions variables (2000 kPa). Les données ont été comparées à diverses corrélations de la littérature. Les constantes de Saxena & Vogel (1977) pour les corrélations de type Wen-Yu ($Re_{mf} = \sqrt{C_1^2 + C_2 Ar} - C_1$) ont donné le meilleur ajustement pour prédire l'U_{mf} des PSD avec des diamètres moyens de Sauter (SMD) moins plus de 109 µm, tandis que Chitester et al. (1984) ont donné de meilleures prédictions pour les distributions de tailles plus grandes (SMD supérieur à 236 µm). On a constaté que la taille des bulles de gaz était légèrement influencée par la pression, la corrélation de Mori et Wen (1975) correspondant le mieux aux données. On a constaté que le coefficient de transfert de chaleur était également légèrement augmenté par la pression avec la corrélation de Molerus et al. (1995) correspondant aux données a pression atmosphérique.

Un modèle de dynamique des fluides et particules (CPFD) de l'unité expérimentale a ensuite été créé et validé en utilisant les données obtenues pour la vitesse de fluidisation minimale et la taille des bulles. La précision du modèle s'est avérée dépendante de la sélection du facteur de compactage des particules, avec une valeur de 0,58 donnant les meilleurs résultats pour chacun des PSD d'ilménite modélisés.

Enfin, un modèle CPFD a été créé pour une conception à écoulement froid du PFIR afin d'étudier les impacts de différents paramètres d'opération sur le taux de circulation des solides et le taux d'infiltration de gaz entre les deux zones du réacteur. Ce modèle utilise les paramètres validés du modèle CPFD précédent pour renforcer la confiance des résultats. Les impacts de l'augmentation de la vitesse du gaz superficiel, de la vitesse du jet de gaz de fluidisation, de la hauteur du lit et de la pression se sont tous avérés augmenter

la vitesse de circulation des solides grâce à leurs impacts respectifs sur le taux de quantité de mouvement du gaz de fluidisation. Une fonction polynomiale a été ajustée entre ces deux variables, ce qui a abouti à une méthode de prédiction du taux de circulation des solides. De même, le taux d'infiltration de gaz entre les deux sections de réacteur s'est avéré dépendant du taux de circulation des solides, ce qui permet de créer une fonction pour prédire l'infiltration de gaz dans différentes conditions d’opération.

Statement of Contributions of Collaborators

I hereby declare that I am the sole author of this thesis. The experimental and numerical work that I completed in this research was inspired by previous work on the design of a pressurized chemical looping combustion (PCLC) pilot facility by CanmetENERGY-Ottawa, and the reactor design patent for the Plug Flow Internally-circulating Reactor (PFIR) by Hatch Ltd. All experimental work, model creation, and post processing of data described in this thesis is my own work. Both my supervisors, Dr. Arturo Macchi and Dr. Poupak Mehrani, provided weekly guidance in this research and contributed to the editing of the journal article presented in Chapter 2 and the manuscripts presented in Chapters 3 and 4. In addition, Dr. Dennis Lu, Dr. Robert Symonds, and Scott Champagne contributed to preparing the journal article presented in Chapter 2. Furthermore, Dr. Robin Hughes provided guidance and contributed on the editing and organization of the manuscripts presented in Chapter 3 and 4. Alex Kokourine also contributed to the creation of the PFIR computational model used to investigate the PFIR geometry presented in Chapter 4. Finally, the PCLC teams at CanmetENERGY-Ottawa and Hatch, Ltd provided regular feedback and thoughts on the results shown in Chapter 4. The modeling software used in this work was purchased from the company CPFD Software, LLC. The staff at CPFD software provided as needed support in model set-up and troubleshooting.

Table of Contents

List of Figures

List of Tables

Acknowledgments

I owe immense gratitude towards my supervisors Dr. Arturo Macchi and Dr. Poupak Mehrani for their guidance and support throughout my degree. They provided me with not only academic guidance, but also valuable professional and life advice. Their mentorship is a gift for which I am deeply appreciative.

I would also like to thank Dr. Robin Hughes and Patrick Boisvert from Natural Resources Canada CanmetENERGY Ottawa for their expertise and advice on my work. Furthermore, the team at Hatch Ltd., Andrew Tohn, Sabrina Francey, Alex Kokourine, and Kamal Adham for their continual support and guidance on this project.

I also owe thanks to my research group members, Milad Taghavivand, Fahad Chowdhury, and Mohsen Isaac Nimvari for their continuous support and help towards this project by aiding in the operation of the experimental unit. Special thanks to Fang Li who originally trained me on the operation of the experimental unit at the beginning of this study.

I also owe gratitude for the help from the staff at the Department of Biological and Chemical Engineering at the University of Ottawa: Franco Ziroldo, Gérard Nina, James Macdermid, Francine Pétrin and Sylvie Saindon, and Chantal Dubé for their kindness and assistance.

I would like to acknowledge the financial supports from the Natural Sciences and Engineering Research Council (NSERC) of Canada, CanmetENERGY-Ottawa, Hatch Ltd, and the MITACs Accelerate program. I also wish to thank the staff at CPFD Software for their help in creating and maintaining the CPFD models.

Chapter 1 Introduction

In 2015 at the 21st session of the Conference of the Parties (COP 21), over 190 nations adopted the Paris Agreement. The goal of the agreement was to limit the rise of global temperatures to 2°C or lower relative to pre-industrial levels by limiting the emissions of green house gas (GHG) emissions and achieve a climate neutral world by 2050 [1]. Implementation of carbon capture, utilization, and sequestration (CCUS) technologies has been shown to be a key aspect of reaching the goals set by the Paris Agreement [2]. CCUS is the process of separating carbon dioxide (CO_2) from industrial emission sources and either utilizing the CO_2 to produce another carbon-based product (ex. methanol), or permanently storing it in carbon sinks (geological formations, exhausted oil and gas wells, etc) thereby preventing it from entering the atmosphere and contributing to the negative effects of climate change. There are three main categories of CCUS technologies for separating CO_2 from industrial combustion processes: Pre-combustion (Figure 1-1A), Post-combustion (Figure 1-1B), and Oxyfuel combustion (Figure 1-1C). Pre-combustion technologies use gasification and water gas shift reactors to generate a mixture of CO_2 and H_2. The CO_2 is separated, allowing the hydrogen to be combusted for power or heat generation. Post-combustion processes use a CO_2 scrubbing unit after the flue gas processing units to separate the CO_2 from the remaining nitrogen. Typically, these scrubbing units employ amines to capture the CO_2. Oxyfuel combustion processes combust the fuel with high purity oxygen supplied by an air separation unit (ASU). This way, the flue gases are not diluted with nitrogen and the CO_2 can be easily separated from the resulting stream.

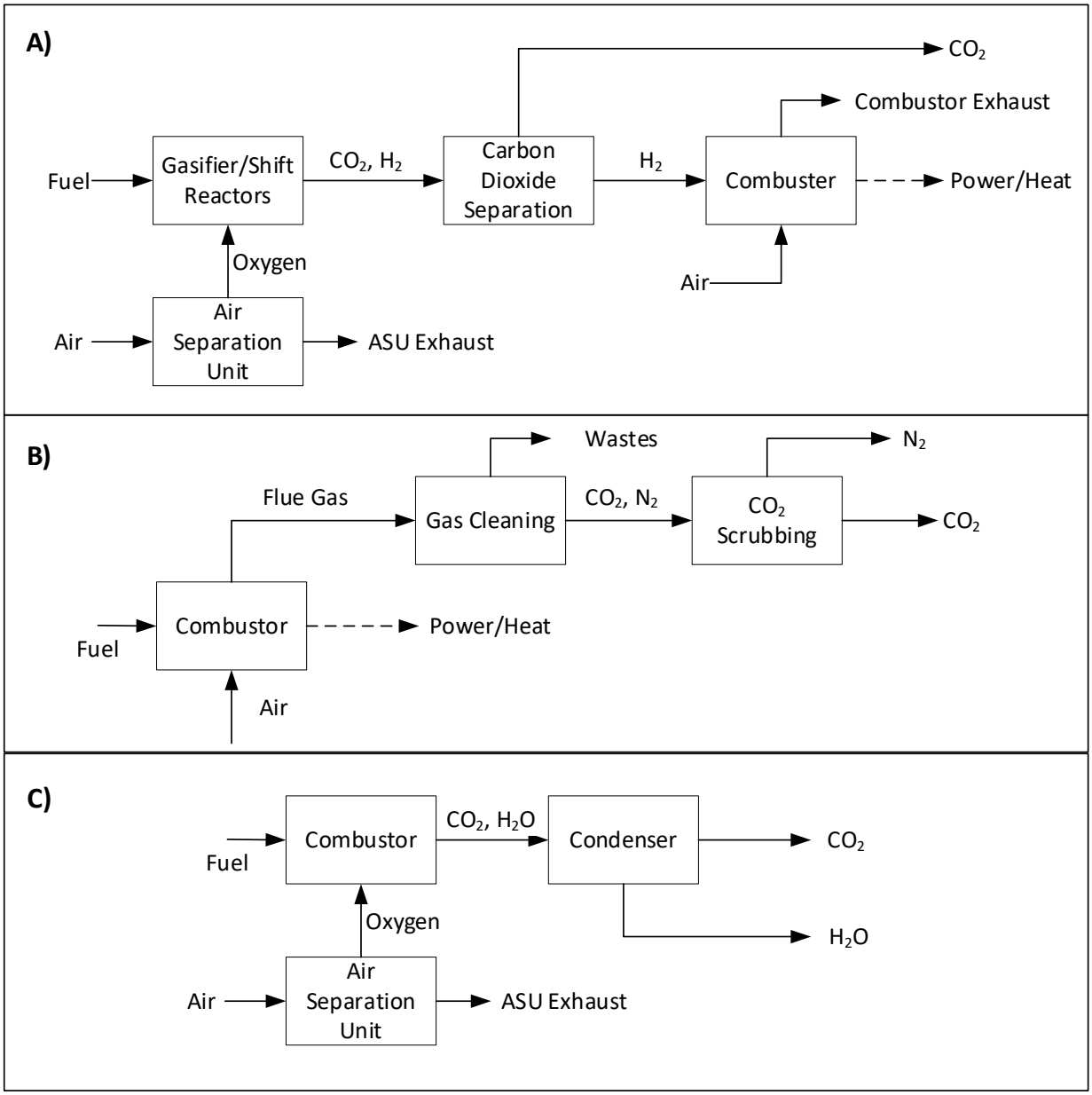

Figure 1-1. Simplified block flow diagrams of the three main types of CCUS technologies. A) Pre-combustion; B) Post-Combustion; and C) Oxyfuel Combustion

1.1 Chemical Looping Combustion

Chemical looping combustion (CLC) is a next generation CCUS technology that operates in a similar fashion to oxyfuel combustion processes. Instead of using an energy intensive ASU which lowers overall energy efficiency, CLC employs a solid metal oxide, called an oxygen carrier (OC), to provide high purity oxygen for combustion [3,4]. This OC is cycled between two reactors, undergoing cyclic oxidation and

reduction steps (Figure 1-2) [5]. In the air reactor, the OC enters in a reduced state and undergoes an oxidation reaction with the incoming air (Reaction 1.1). The now oxidized OC enters the fuel reactor where it takes part in a reduction reaction with the entering fuel (Reaction 1.2). The now reduced OC is looped back into the air reactor to be re-oxidized. The flue gas from the air reactor contains primarily inert nitrogen, while the flue gas from the fuel reactor contains primarily CO_2 and H_2O, which are easily separable through condensation of the water vapour.

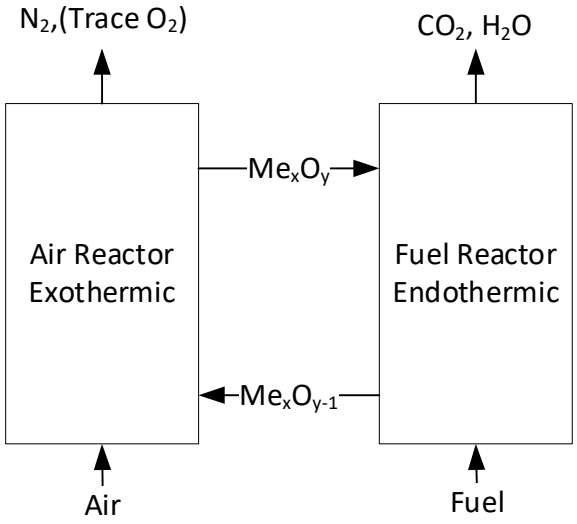

Figure 1-2. Schematic of chemical looping combustion reactors

$$(2n+m)Me_xO_y + C_nH_{2m} \rightarrow (2n+m)Me_xO_{y-1} + mH_2O + nCO_2 \quad (1.1)$$

$$Me_xO_{y-1} + 0.5\ O_2 \rightarrow Me_xO_y \quad (1.2)$$

Oxygen carriers will strongly influence the operating conditions and cost of CLC systems, so selection is an important factor during design. In general, it is important OCs exhibit high redox activity, have high chemical stability over multiple reduction and oxidation reactions, high mechanical strength, and resist agglomeration. Additionally, OCs should be inexpensive and environmentally benign. Natural ores present promising and inexpensive choices for OCs because they can often be used directly without need of additional supports [6,7]. Ilmenite is a naturally occurring ore primarily composed of iron and titanium which exhibits favourable thermodynamic properties, high attrition resistance, high combustion efficiency, and is abundant in Canada making it a promising OC candidate [8–11]. Reaction rates of ilmenite with methane have been shown to be relatively slow at atmospheric pressure but can be greatly improved by increasing the operating pressures between 600 kPa to 1600 kPa [12,13]. Furthermore, pressurized chemical looping combustion (PCLC) has many other techno-economic advantages over CLC [14,15].

Proper gas-solid contacting, solids circulation, and heat transfer are critical to achieve the desired fuel conversions making interconnected circulating fluidized beds (ICFBs) a promising reactor concept for CLC. Significant research has been conducted on these systems for implementation in CLC systems [16–22]. ICFBs consist of two separate reactor vessels connected by external solid transfer legs called loop seals. Cyclones are implemented at the gas outlets to separate entrained solids from the leaving gases. While ICFBs can achieve high solids circulation rates, they have the disadvantage of relatively high capital costs due to their size and complexity.

A new patented reactor concept was proposed by Adham et al. [23,24] following a report from the United States Department of Energy (US DOE) on CCUS recommended that new chemical looping reactor concepts should employ multiple internal stages and non-mechanical gas-solid flow control to improve the operation and cost (capital and operating) reductions of CLC processes [25]. This reactor design (Figure 1-3), called the Plug Flow Internally-circulating Reactor (PFIR) [23,24], consists of two annular reactive zones separated by baffles with underflow slots. Solids are fluidized and circulated through these reactive zones by angled tuyeres located at the bottom of the reactor. A cold flow PFIR unit, and pilot scale PCLC-PFIR system are currently under development by Hatch Ltd. (Mississauga, Ontario, Canada) and Natural Resources Canada CanmetENERGY-Ottawa (Ottawa, Ontario, Canada).

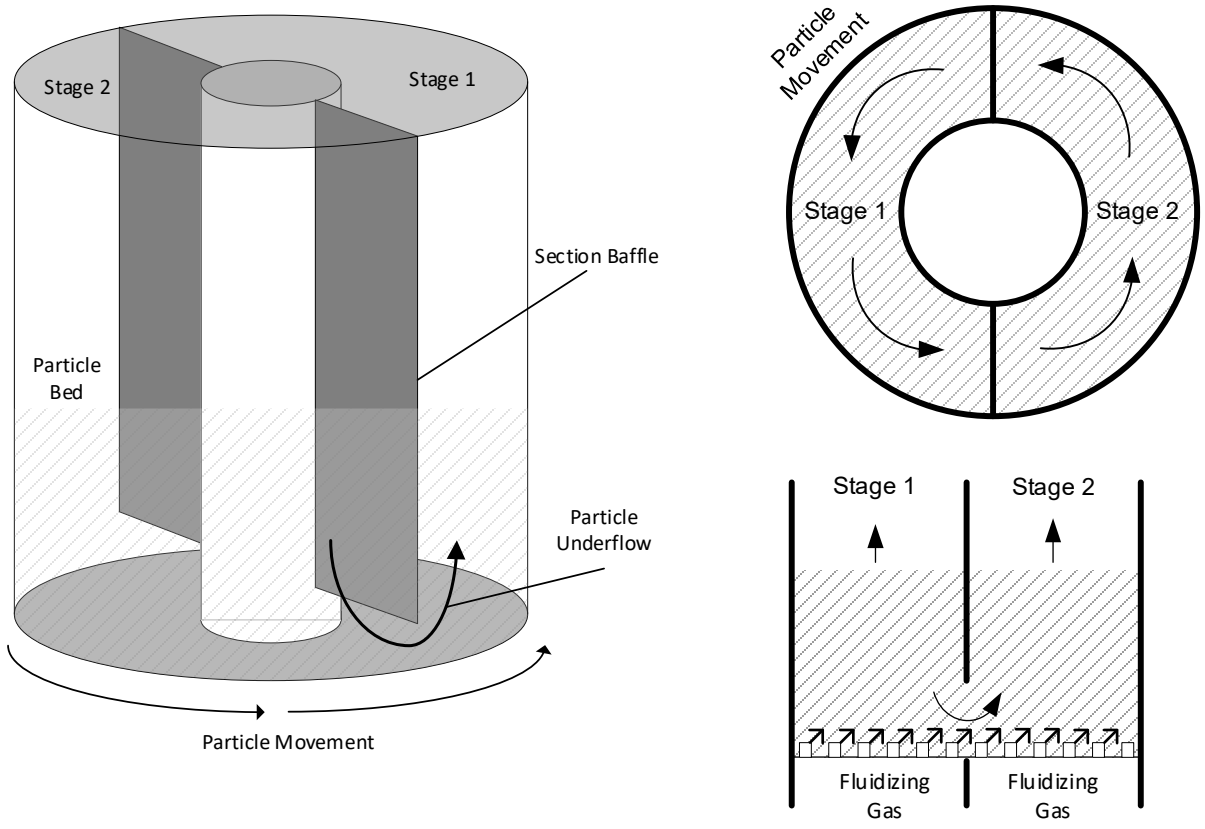

Figure 1-3. Schematic of PFIR geometry. A) 3-dimensional view B) Top-down view C) Side view of stage transition

The design of this pilot scale facility requires knowledge of key design information such as the minimum fluidization velocity, gas bubble characteristics, and tube-to-bed heat transfer coefficients of ilmenite. Furthermore, since the PFIR is a new reactor design concept, the behaviour of the solids circulation rate and potential for gas infiltration between sections remains unknown. Understanding the gas-solids flow of the PFIR is a critical first step in its implementation to prevent avoidable design flaws. The Multi-Phase Particle-in-Cell (MP-PIC) approach, also known as Computation Particle Fluid Dynamics (CPFD) modeling, is an efficient method of modeling larger scale fluidized bed systems making it well suited to investigating the PFIR. CPFD differs from more traditional fluidized bed modeling techniques like the Two-Fluid-Model (TFM) and Discrete Elemental Modeling (DEM) by grouping solids of similar properties (mass, velocity, position, etc.) into computational parcels and treating the solid phase as both discrete entities and a continuum [26–28]. Particle properties are either solved in a Eulerian framework as a

continuum, or in a Lagrangian framework as discrete entities. This way, CPFD modeling reduces the computational load for larger systems, while still maintaining high resolutions of the solid phase.

1.2 Thesis Objectives and Structure

The objective of this thesis is to provide these key design parameters and insight for the construction of the pilot scale PCLC system at CanmetENERGY-Ottawa using ilmenite as the oxygen carrier. The work presented in this thesis is in three parts separated into Chapters 2, 3, and 4. Chapter 1 of this thesis provides background information for the work presented in the later chapters, while Chapter 5 gives a summary of conclusions obtained and suggestions of future work.

Chapter 2 presents published experimental work which explores the high pressure fluidized bed hydrodynamics and tube-to-bed heat transfer coefficient of ilmenite particles. Ilmenite is a relatively dense particle which causes it to fall outside of the validated ranges of many popular fluidized bed design correlations. The work compared experimental values of minimum fluidization velocity, gas bubble size, and tube-to-bed heat transfer coefficients at different operating conditions to a variety of literature correlations in order to determine which correlations would be best applied to designing the PCLC pilot scale system.

Chapter 3 comprises an in-preparation journal manuscript that validates a Computational Particle Fluid Dynamic (CPFD) model of the high pressure fluidized bed described in Chapter 2 to the experimental data also obtained in Chapter 2. The CPFD model was created using the commercially available software Barracuda Virtual Reactor ®. Chapter 3 served as a pre-validation to the work presented in Chapter 4 by determining key model input parameters for the fluidization of ilmenite particles. The model presented in Chapter 3 also expanded upon the results of the experimental work by exploring results (e.g., cross-sectional bubble size distribution along bed height) that the experimental apparatus could not obtain.

Chapter 4 is an in-preparation journal manuscript that describes the novel fluid bed reactor concept that will be implemented in the PCLC pilot scale system. A CPFD model of the cold flow PFIR geometry was created to give insight into key design parameters. The validated model parameters determined in Chapter 3 were used in this CPFD model to increase the confidence in the model results. The effects of various operating conditions (superficial gas velocity, tuyere jet velocity, bed height, and operating pressure) on the particle circulation rate and gas infiltration were investigated.

References

[1] The United Nations, The Paris Agreement, United Nations Paris Agreem. (2021). https://unfccc.int/process-and-meetings/the-paris-agreement/the-paris-agreement (accessed January 24, 2021).

[2] R.K. Pachauri, L.A. Meyer, Climate Change 2014: Synthesis Report. Contribution of Working Groups I, II and III to the Fifth Assessment Report of the Intergovernmental Panel on Climate Change, Geneva, Switzerland, 2014. https://www.ipcc.ch/report/ar5/syr/.

[3] A. Lyngfelt, B. Leckner, A 1000 MWth boiler for chemical-looping combustion of solid fuels – Discussion of design and costs, Appl. Energy. 157 (2015) 475–487. https://doi.org/10.1016/j.apenergy.2015.04.057.

[4] M. Rydén, A. Lyngfelt, T. Mattisson, Synthesis gas generation by chemical-looping reforming in a continuously operating laboratory reactor, Fuel. 85 (2006) 1631–1641. https://doi.org/10.1016/j.fuel.2006.02.004.

[5] T. Pröll, Fundamentals of chemical looping combustion and introduction to CLC reactordesign, in: P. Fennell, B. Anthony (Eds.), Calcium Chem. Looping Technol. Power Gener. Carbon Dioxide Capture, Woodhead Publishing, Cambridge, UK, 2015: pp. 197–219. https://doi.org/10.1016/B978-0-85709-243-4.00010-0.

[6] T. Mendiara, R. Pérez, A. Abad, L.F. De Diego, F. García-Labiano, P. Gayán, J. Adánez, Low-cost Fe-based oxygen carrier materials for the iG-CLC process with coal. 1, Ind. Eng. Chem. Res. 51 (2012) 16216–16229. https://doi.org/10.1021/ie302157y.

[7] M. Arjmand, H. Leion, T. Mattisson, A. Lyngfelt, Investigation of different manganese ores as oxygen carriers in chemical-looping combustion (CLC) for solid fuels, Appl. Energy. 113 (2014) 1883–1894. https://doi.org/10.1016/j.apenergy.2013.06.015.

[8] G.L. Schwebel, D. Filippou, G. Hudon, M. Tworkowski, A. Gipperich, W. Krumm, Experimental comparison of two different ilmenites in fluidized bed and fixed bed chemical-looping combustion, Appl. Energy. 113 (2014) 1902–1908. https://doi.org/10.1016/j.apenergy.2013.07.042.

[9] F.N. Ridha, M.A. Duchesne, X. Lu, D.Y. Lu, D. Filippou, R.W. Hughes, Characterization of an ilmenite ore for pressurized chemical looping combustion, Appl. Energy. 163 (2016) 323–333. https://doi.org/10.1016/j.apenergy.2015.10.070.

[10] F. Mayer, A.R. Bidwe, A. Schopf, K. Taheri, M. Zieba, G. Scheffknecht, Comparison of a new micaceous iron oxide and ilmenite as oxygen carrier for Chemical looping combustion with respect to syngas conversion, Appl. Energy. 113 (2014) 1863–1868. https://doi.org/10.1016/j.apenergy.2013.04.056.

[11] S. Rana, Z. Sun, P. Mehrani, R. Hughes, A. Macchi, Ilmenite oxidation kinetics for pressurized chemical looping combustion of natural gas, Appl. Energy. 238 (2019) 747–759. https://doi.org/10.1016/j.apenergy.2019.01.126.

[12] Y. Tan, F.N. Ridha, M.A. Duchesne, D.Y. Lu, R.W. Hughes, Reduction Kinetics of Ilmenite Ore as an Oxygen Carrier for Pressurized Chemical Looping Combustion of Methane, Energy and Fuels. 31 (2017) 7598–7605. https://doi.org/10.1021/acs.energyfuels.7b01038.

[13] Y. Tan, F.N. Ridha, D.Y. Lu, R.W. Hughes, Reduction Kinetics of Ilmenite Ore for Pressurized Chemical Looping Combustion of Simulated Natural Gas, Energy and Fuels. 31 (2017) 14201–14210. https://doi.org/10.1021/acs.energyfuels.7b02648.

[14] A. Cabello, R.W. Hughes, R.T. Symonds, S. Champagne, D.Y. Lu, E. Mostafavi, N. Manihpey,

Economic Analysis of Pressurized Chemical Looping Combustion for SAGD Application, in: 5th Int. Conf. Chem. Looping, Park City, Utah, USA, 2018.

[15] R.T. Symonds, R.W. Hughes, D.Y. Lu, P. Navarri, O. Ashrafi, Systems analysis of pressurized chemical looping combustion for SAGD applications, Int. J. Greenh. Gas Control. 73 (2018) 111–123. https://doi.org/10.1016/j.ijggc.2018.03.008.

[16] B. Kronberger, E. Johansson, G. Löffer, T. Mattisson, A. Lyngfelt, H. Hofbauer, A two-compartment fluidized bed reactor for CO2 capture by chemical-looping combustion, Chem. Eng. Technol. 27 (2004) 1318–1326. https://doi.org/10.1002/ceat.200402137.

[17] B. Kronberger, A. Lyngfelt, G. Löffler, H. Hofbauer, Design and fluid dynamic analysis of a bench-scale combustion system with CO2 separation-chemical-looping combustion, Ind. Eng. Chem. Res. 44 (2005) 546–556. https://doi.org/10.1021/ie049670u.

[18] E. Johansson, A. Lyngfelt, T. Mattisson, F. Johnsson, Gas leakage measurements in a cold model of an interconnected fluidized bed for chemical-looping combustion, Powder Technol. 134 (2003) 210–217. https://doi.org/10.1016/S0032-5910(03)00125-6.

[19] P. Kolbitsch, T. Pröll, J. Bolhar-Nordenkampf, H. Hofbauer, Design of a chemical looping combustor using a dual circulating fluidized bed reactor system, Chem. Eng. Technol. 32 (2009) 398–403. https://doi.org/10.1002/ceat.200800378.

[20] L.S. Fan, L. Zeng, S. Luo, Chemical-Looping Technology Platform, AIChE J. 59 (2015) 215–228. https://doi.org/10.1002/aic.

[21] L.S. Fan, L. Zeng, W. Wang, S. Luo, Chemical looping processes for CO2 capture and carbonaceous fuel conversion - Prospect and opportunity, Energy Environ. Sci. 5 (2012) 7254–7280. https://doi.org/10.1039/c2ee03198a.

[22] I. Ahmed, H. De Lasa, CO2 Capture Using Chemical Looping Combustion from a Biomass-Derived Syngas Feedstock: Simulation of a Riser-Downer Scaled-Up Unit, Ind. Eng. Chem. Res. 59 (2020) 6900–6913. https://doi.org/10.1021/acs.iecr.9b05753.

[23] K. Adham, C. Harris, A. Kokourine, Plug Flow Reactor with Internal Recirculation Fluidized Bed, CA2951724, 2015.

[24] K. Adham, C. Harris, A. Kokourine, Modeling and Process Features of Plug Flow Reactor with Internal Recirculation for Biomass Pyrolysis, J. Chem. Eng. Process Technol. 08 (2017) 353. https://doi.org/10.4172/2157-7048.1000353.

[25] T. Niass, J. Kislear, M. Buchanan, J. Svalestuen, A. Park, D. DePaolo, J. Powel, Accelerating Breakthrough Innovation in Carbon Capture, Utilization and Storage, Huston, Texas, 2017. http://publications.lib.chalmers.se/records/fulltext/245180/245180.pdf%0Ahttps://hdl.handle.net/20.500.12380/245180%0Ahttp://dx.doi.org/10.1016/j.jsames.2011.03.003%0Ahttps://doi.org/10.1016/j.gr.2017.08.001%0Ahttp://dx.doi.org/10.1016/j.precamres.2014.12.

[26] D.M. Snider, An Incompressible Three-Dimensional Multiphase Particle-in-Cell Model for Dense Particle Flows, J. Comput. Phys. 170 (2001) 523–549. https://doi.org/10.1006/jcph.2001.6747.

[27] D.M. Snider, P.J. O'Rourke, The Multiphase Particle In Cell (MP-PIC) Method for Dense Particle Flow, in: S. Pannala, M. Syamlal, T.J. O'Brien (Eds.), Comput. Gas-Solids Flows React. Syst. Theory, Methods, Pract., 1st ed., IGI Global, Hershey, PA, 2011. https://doi.org/10.1017/CBO9781107415324.004.

[28] M. J. Andrews and P.J. O'Rourke, The Multiphase Particle-in-Cell (MP-PIC) Method for Dense Particulate Flows, Int J Multiph. Flow. 22 (1996) 379–402.

Chapter 2 Experimental Evaluation of Hydrodynamics and Tube-to-Bed Heat Transfer of Fluidized Ilmenite Ore Particles at Elevated Pressures

C. J. McIntyre[a], R.T. Symonds[b], D.Y. Lu[b], S. Champagne[b,] A. Macchi[a*], P. Mehrani[a*]

[a] Department of Chemical and Biological Engineering, University of Ottawa, 161 Louis Pasteur Street, Ottawa, ON, Canada, K1N 6N5

[b] Natural Resources Canada, CanmetENERGY, 1 Haanel Drive, Ottawa, ON, Canada, K1A 1M1

[*]*Corresponding authors email.* Poupak Mehrani: poupak.mehrani@uottawa.ca; Arturo Macchi arturo.macchi@uottawa.ca

The current chapter is a manuscript published in the journal of Powder Technology "Powder Technology, 376, 697 - 707, 2020"

Abstract

The minimum fluidization velocity (U_{mf}), bubble size characteristics, and tube-to-bed heat transfer coefficient (h_c) of ilmenite particles are investigated at pressures up to 2000 kPa. The U_{mf} was found to decrease with pressure for $d_{sv} \geq 236$ µm and remain constant for $d_{sv} \leq 109$ µm. U_{mf} was compared to various Wen and Yu type correlations ($Re_{mf} = \sqrt{C_1^2 + C_2 Ar} - C_1$) with the Saxena & Vogel (1977) constants resulting in the best fit (AARD = 10.5%) for $d_{sv} \leq 109$ µm and the Chitester *et al.* (1984) constants resulting in the best fit (AARD = 6.4%) for $d_{sv} \geq 236$ µm. Pressure marginally effected bubble size relative to gas velocity, with the data fitting the Mori & Wen (1975) correlation best (AARD = 26.4%). The tube-to-bed heat transfer coefficient experienced a maximum with increasing gas velocity and marginally increased with pressure. The Molerus *et al.* (1995) correlation matched the atmospheric heat transfer data.

Keywords: Pressurized fluidized-bed, ilmenite ore, minimum fluidization, bubble size, heat-transfer

Nomenclature

Variables	
A_1, A_2	Shape-bed void functions in eq. 7
Ar	Archimedes number $\left(= \frac{d_v^3 \rho(\rho_p - \rho)g}{\mu^2}\right)$
A_t	Heating tube surface area (m^2)
C_1, C_2	Constants in eq. 8
$c_{p,s}$	Solids heat capacity $(J/kg\ K)$
D	Column diameter (m)
d_0	Initial gas bubble diameter (m)
d_b	Gas bubble diameter (m)
d_{be}	Equilibrium gas bubble diameter (m)
d_{bm}	Maximum gas bubble diameter (m)
d_t	Heating tube diameter (m)
d_{sv}	Volume to surface mean particle diameter (m)
d_v	Volume mean particle diameter (m)
g	Gravity constant $(9.81\ m/s^2)$
H	Height (m)
h_c	Convective tube-to-bed heat transfer coefficient (W/m^2K)
I	Electric current (A)
k_g	Thermal conductivity of gas $(W/m\ K)$
l	Parameter in eq. 11 & 12
n	Number of holes in perforated plate distributor
Pr	Prandtl Number $\left(= \frac{c_{p,g}\mu}{k_g}\right)$
Re_{mf}	Reynolds number at minimum fluidization $\left(= \frac{U_{mf} d_v \rho}{\mu}\right)$
S_H	Horizontal distance between tube in the bundle (m)
S_V	Vertical distance between tube in the bundle (m)
U	Fluid superficial velocity (m/s)
U_e	Excess gas velocity (m/s)
U_{mf}	Minimum fluidization velocity (m/s)
V	Electric Potential (V)
γ, δ, η	Parameters in Horio & Nonaka correlation (Table 1-3)
ϵ	Bed void fraction
ϵ_{mf}	Bed void fraction at minimum fluidization
ρ	Fluid density (kg/m^3)
ρ_p	Particle density (kg/m^3)
$\sigma_{\Delta P}$	Differential pressure standard deviation (Pa)
ϕ	Particle shape factor
μ	Fluid viscosity $(Pa \cdot s)$

Abbreviations	
AARD	Absolute Average Relative Deviation, $= \frac{1}{n}\sum \frac{\lvert x_{experimental} - x_{predicted} \rvert}{x_{experimental}} \times 100\%$
CCUS	Carbon Capture Utilization and Sequestration
CLC	Chemical Looping Combustion
FBC	Fluidized Bed Combustor
GHG	Green House Gas
HB	High Bed
LB	Low Bed
OC	Oxygen Carrier
OCAC	Oxygen Carrier Assisted Combustion
PCLC	Pressurized Chemical Looping Combustion

2.1 Introduction

There has been a substantial research and development effort in developing carbon capture, utilization, and storage (CCUS) technologies in recent years to reduce greenhouse gas (GHG) emissions from fossil fuel-based processes. Chemical looping combustion (CLC), initially proposed by Lewis and Gilliland in the 1950s for the production of pure carbon dioxide [1,2], is recognized as an emerging advanced CCUS technology [3]. Due to its inherent advantages over competing CO_2 separation technologies, including high energy conversion efficiencies, this technology is now widely considered a promising strategy for clean heat, power, and steam generation [4]. CLC processes are typically carried out in dual fluidized bed systems; oxidation in an air reactor and reduction in a fuel reactor. A metal oxide acting as an oxygen carrier (OC) is employed to transfer oxygen from the air to fuel reactor, thereby avoiding direct contact between fuel and air. In general, important performance criteria for OCs include high redox reactivity, high stability under repeated redox cycles at high temperatures, and high resistance to attrition and agglomeration. Additionally, the OCs properties strongly influence cost of the proposed applications, operating conditions, optimal reactor configuration, and many other aspects. Therefore, it is important that the OC be inexpensive and environmentally benign [5]. This is especially important for operations that require high replacement rates for OCs such as solid fuel operations where the carrier can be deactivated by the produced ash or operations that employ high sulphur content fuels which can also cause OC deactivation. Furthermore, ilmenite could possibly become brittle in an oxidizing environment increasing the necessary make-up rate due to fines production [6].

In order to meet these economic and environmental requirements, we believe that natural ores or minerals are the preferred choice for CLC since they are often inexpensive and can be used directly without being combined with supports [3,7]. For this reason, ilmenite ore, largely comprised of Fe and Ti containing species, is considered a promising OC for CLC applications due to its desired thermodynamic properties, high attrition resistance, and high combustion efficiency [8–10]. It has been shown that ilmenite ore exhibits high reactivity with CO and H_2; however, reaction rates with CH_4 are relatively slow [11–13] and these weak redox characteristics might hinder application development [3,10,14,15]. Our approach for improving ilmenite ore reactivity is to shift towards elevated operating pressures [6,16,17]. Symonds *et al.* [18] and Cabello *et al*. [5] found many techno-economic benefits when considering the combustion of natural gas in a pressurized CLC (PCLC) system for industrial heat generation with CO_2 capture when ilmenite ore was used as the OC.

Furthermore, oxygen carrier aided combustion (OCAC) in fluidized bed combustors (FBCs) is a novel process that consists of replacing, totally or partially, the inert bed material by an active oxygen carrying material such as ilmenite ore. The use of these materials may enhance the combustion efficiency and reduce hot spots in the combustor *via* its oxygen buffering ability. During fuel combustion, the OC is reduced providing oxygen in oxygen lean zones and oxidized/regenerated in oxygen rich zones. The previously mentioned high reactivity rates of ilmenite with CO and H_2 makes it a suitable OC for use in FBCs; especially when burning solid fuels with high volatiles content such as lignite and biomass [19–23]. In addition, as a result of the combustion of gaseous fuel components in the dense bed *via* reaction with the oxygen carrier, less excess oxygen is needed to meet emission restrictions, suggesting that OCAC is a promising technology to broadly improve the performance of FBCs, including oxy-fuel combustors [24].

Despite its many potential uses in fluidized beds, studies specifically focused on the fluid bed hydrodynamics and tube-to-bed heat transfer of ilmenite ore remain scarce, with one found article that studied the heat transfer coefficient at elevated temperatures [25]. Proper understanding of the hydrodynamics and tube-to-bed heat transfer is especially important to technologies that implement pressurized reactor designs using in bed heat exchangers. The constrained volume and presence of heat exchanger tubes can decrease heat transfer rates by impeding particle movement. Correlations can be used to estimate the tube-to-bed heat transfer coefficient, but are largely limited in their applicability outside their validated ranges [26–28]. Furthermore, many correlations are validated using large libraries of literature data, which can omit specific operating conditions such as small and high-density particles at increased pressure. Given the importance of ilmenite ore to research and development of promising CCUS technologies (e.g., PCLC, OCAC, oxy-fuel, etc.), further study of the material is needed.

The goal of this work was thus to explore the minimum fluidization, bubble characteristics, and the tube-to-bed heat transfer coefficient of ilmenite ore particles under different operating pressures and gas velocities. These system parameters were compared to multiple literature correlations to evaluate their predictive accuracy and suitability for ilmenite ore.

2.2 Experimental Set up

The experimental apparatus, along with schematics, are explained in detail elsewhere [29]. Experiments were performed in a 0.154 m diameter stainless steel cylindrical pressurized fluidization column with a height of 3 m. The distributor is a perforated plate consisting of two stainless steel plates pressed together with a 45 μm mesh in between. The column was operated up to pressures of 2000 $kPa_{(a)}$, measured by a gauge pressure transducer located at the top of the column. Three ports are located axially starting 0.17 m

above the distributor plate and 0.15 m apart for differential pressure measurements taken across the particle bed. Additional ports are located below the distributor plate and at the top of the column for added differential pressure measurements of the bed and in the freeboard. Air was used as the fluidizing medium and its flow rate was measured by an orifice plate meter. Images of the unit are presented in Appendix A.

The column was operated in two configurations: atmospheric and pressurized. For atmospheric pressure operations, building air was supplied continuously and passed through the system before being released to the atmosphere. For pressurized operations, the column was first pressurized to the desired static pressure and then a centrifugal compressor with a variable speed drive was used to overcome the system pressure drop and recirculate the air through the system in a closed loop. A heat exchanger was included at the outlet of the compressor to maintain a consistent fluidizing gas temperature of 20°C.

For heat transfer tests, a tube bundle was lowered into the column and rested on top of the distributor plate to replicate the geometry of an in-bed heat exchanger (Figure 2-1). The tube bundle consists of five alternating rows of either two or three aluminum tubes housed in a cylindrical stainless-steel casing with a diameter slightly smaller than the column inner diameter. The tubes begin 0.22m from the bottom of the tube bank. The center tube in the second row from the top was replaced by a heating tube. Single tube heat transfer tests were also performed where all the tubes were removed except for the heating tube and the top row to allow for the installation of the tube apparatus. A k-type thermocouple was inserted above the tube bank to measure the bed temperature.

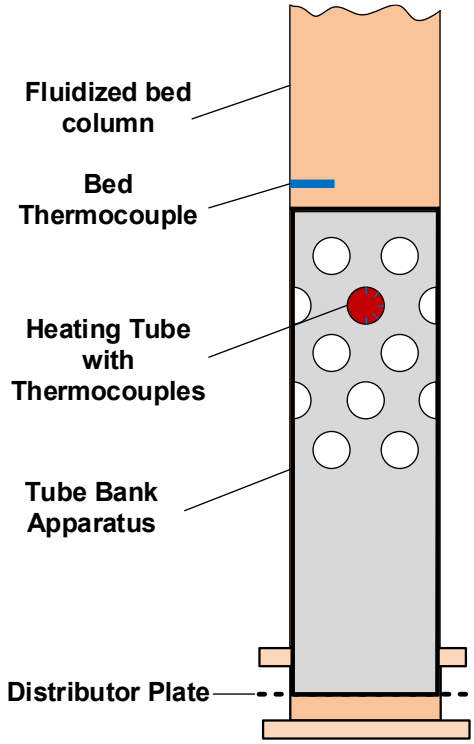

Figure 2-1. Schematic of insertable tube bundle assembly containing a heating tube (shaded circle) inside the fluidized bed column (truncated). The relative horizontal and vertical tube pitches (SH⁄dt and SV⁄dt) were respectively above 2 and 1.5; dimensions are omitted for confidentiality.

The heating tube consists of an internal heating cartridge surrounded by a copper sheathe and capped with Teflon insulators to minimize axial heat transfer. The heating cartridge is attached to a 900 W power source to supply heat to the tube. There are five k-type thermocouples spaced 45° apart to measure the local temperature along the circumference of the heating tube numbered one through five starting at the bottom. More detailed information on the tube bundle and heating cartridge are described elsewhere [29].

Cold flow operating conditions tested in this work were chosen to reflect those found in PCLC systems. All experiments were performed at 20°C. Data collection and process control were enabled through using LabView software.

The particles tested were UKTO ilmenite ore (upgraded roasted ore) ($\rho_p = 4700\ kg/m^3$) of varying average particle sizes (surface-to-volume mean diameters of 95 µm, 107 µm, 109 µm, 236 µm, and 321 µm) supplied by Rio Tinto Iron & Titanium Canada. Each particle size is classified as Geldart B. A sphericity value of 0.84 is used following estimations of roundness of the particle determined by image analysis of the particles. A bed composed of 25 kg (approximately 0.60 m expanded bed height) of material was used for all particle sizes except for the 236 µm and 321 µm particle sizes which required 9.8 kg (approximately 0.22 m expanded bed height) of material due to gas compressor limitations. A 25 kg particle

bed allowed for in-bed measurements of bubble size and bed void fraction at various axial locations, as well as proper coverage of the tube bundle and in-bed thermocouple when heat transfer measurements were taken.

2.3 Methodology

2.3.1 Minimum Fluidization Velocity and Bed Void fraction

The minimum fluidization velocity was determined experimentally by employing the standard method of plotting the measured bed pressure drop as a function of decreasing superficial gas velocity from fluidized conditions to zero [30]. This approach avoids issues related to the compaction of the bed which can result in large overshoots in the pressure drop before achieving fluidization while increasing gas velocity. The bed void fraction at minimum fluidization was determined by using the experimentally determined values for the pressure drop at minimum fluidization and U_{mf} in the resulting force balance at minimum fluidization with the Ergun equation (Eq 2-1) [31].

$$\frac{\Delta P_{mf}}{L} = \left(\rho_p - \rho_g\right)\left(1-\epsilon_{mf}\right)g = \frac{150\left(1-\epsilon_{mf}\right)^2 \mu U_{mf}}{\epsilon_{mf}^3 d_{sv}^2} + \frac{1.75\left(1-\epsilon_{mf}\right)\rho_g U_{mf}^2}{\epsilon_{mf}^3 d_{sv}} \qquad [2\text{-}1]$$

2.3.2 Gas Bubble Size Estimates

Two differential pressure measurements were taken over 0.15 m in vertical height between pressure ports one and two (referred to as the low bed region – LB) and between pressure ports two and three (referred to as the high bed region – HB) allowing for an indication of the evolution of bubble dynamics from the lower to upper regions of the bed. A qualitative comparison of bubble size for each region of the bed (LB and HB) was determined from the standard deviation of the differential pressure measurements using Eq 2-2 [32]. For these experiments, the proportionality constant is taken as one [32], but it should be noted that larger proportionality constants of 1.3 and $\sqrt{3}$ have been used by others for Geldart B particles [28].

$$d_b \propto \frac{\sigma_{\Delta P}}{g\left(1-\epsilon_{mf}\right)\rho_p} \qquad [2\text{-}2]$$

A single bubble bursting at the bed surface can be interpreted as a singular sine wave of the differential pressure measurement over time [33]. The average period of the sine wave corresponds to the frequency of bubbling; a large deviation from the average value is indicative of presence of a large bubble; and a less distorted sine wave indicates a smaller bubble size distribution [34]. When using the standard deviation of the differential pressure measurements in Eq 2-2, it is critical that the signal remains as un-dampened as possible. The tube diameters used in the experiments lie within the recommended range of 2-5 mm [35,36],

and the distance to the pressure transducer is kept below the recommended 2.5 m maximum [36]. All pressure signals are recorded above the distributor plate to avoid any resulting dampening effects.

2.3.3 Heat Transfer Measurements

The tube-to-bed heat transfer coefficient was determined by dividing the power input by the heat transfer area and the temperature difference between the heating rod and the particle bed (Eq 2-3). The heat transfer coefficient is known to vary along the circumference of the heating tube [37,38] and therefore the temperature difference was taken locally at each of the five radial thermocouples. This method also allows for investigation of the heat transfer profile along the tube surface that can be used to infer hydrodynamic activity around the heating tube [37]. The average heat transfer coefficient was determined by assuming vertical symmetry around the tube (Eq 2-4).

$$h_{c,i} = \frac{IV}{A_t(T_i - T_b)} \quad [2\text{-}3]$$

$$h_{c,av} = \frac{\sum_1^5 h_{c,i} + \sum_2^4 h_{c,i}}{5 + 3} \quad [2\text{-}4]$$

It is important to note that the direction of heat transfer in these experiments is from the heating tube to the fluidized bed, while typical operations transfer heat from the fluid bed into the tube. For a given hydrodynamic condition, the heat transfer coefficient is experimentally determined from the temperature difference between the bed and tube surface at a constant power input to the heater. The rate and direction of heat transfer will not affect the resulting heat transfer coefficient so long as the phases' physical and thermal properties between the bed and surface do not change substantially. For these experiments, the power is maintained at 18.1 watts resulting in a tube surface between 10-30°C of the bed temperature, which remains near ambient for all hydrodynamic conditions. Therefore, the change in air properties between the tube surface and bed is minor and has a negligible effect on the heat transfer coefficient.

2.4 Results and Discussion

2.4.1 Minimum Fluidization Velocity

The minimum fluidization velocities for the 95 µm, 107 µm and 236 µm mean particle size samples are plotted in Figure 2-2. The larger mean particle size U_{mf} decreased with increasing pressure from 0.18 m/s at atmospheric pressure to 0.10 m/s at 2000 $kPa_{(a)}$ and appears to approach a constant value. The smaller 95 µm and 107 µm particle U_{mf} remained constant at 0.03 m/s and 0.04 m/s, respectively, at all pressures. The influence of pressure on U_{mf} can be explored through analysis of Eq 2-1. The first term on the right-hand side describes the laminar flow around the particle and therefore depends primarily on the viscous forces experienced by the particle. Due to the negligible effect of pressure on viscosity and the dominance of

laminar flow around the smaller particles, changing the pressure does not significantly impact the U_{mf}. The contribution of the laminar term for the smaller particles to the overall pressure drop is above 90% at all pressures. However, for the larger particles, inertial forces increase as described by the second term on the right-hand side. The dependence of inertial effects on the gas density, and in turn the system pressure, results in decreasing U_{mf} with increasing gas pressure. The contribution of the inertial forces to the overall pressure drop increases from 6% to 40% with increasing pressure.

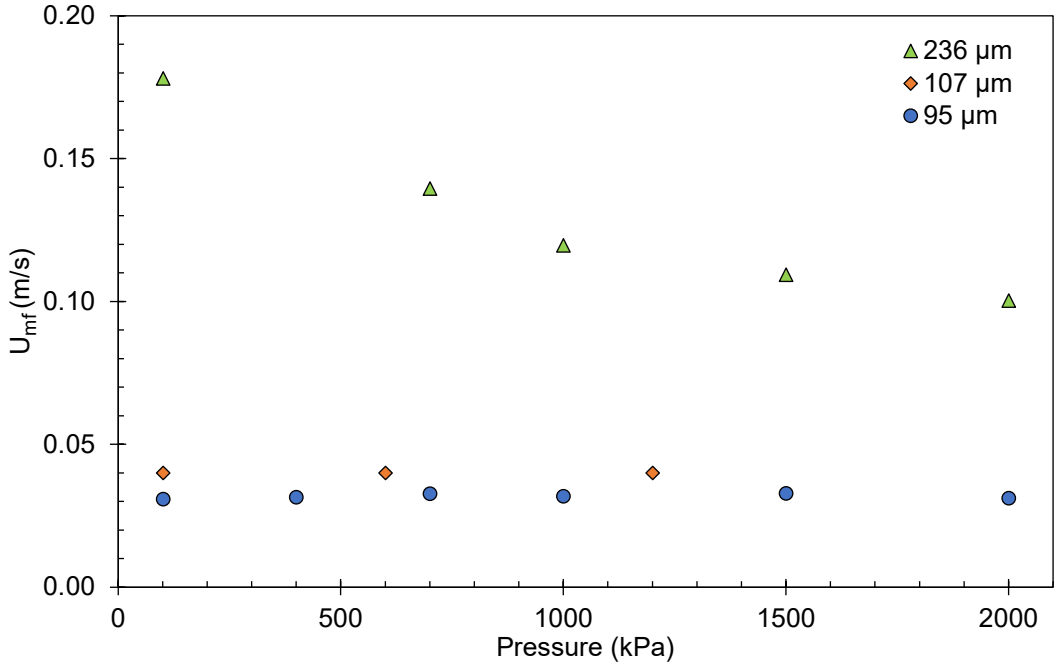

Figure 2-2. Minimum fluidization velocity of 95 µm, 107µm and 236 µm ilmenite particles at varying pressure.

The ability to accurately predict U_{mf} is essential to modelling and design efforts for fluidized beds. Eq 2-1 can be solved directly for U_{mf}, however, this method is sensitive to small errors in bed void fraction and particle shape factor. As such, there are several correlations available in literature [26,30,39,40] to predict U_{mf}. Wen & Yu [39] presented what is arguably one of the most well-known methods of predicting the minimum fluidization velocity in which they solved Eq 2-1 in terms of Re_{mf} (Eq 2-5).

$$150A_1\left(Re_{mf}\right) + 1.75A_2\left(Re_{mf}\right)^2 = Ar \qquad [2\text{-}5]$$

Where

$$A_1 = \frac{1-\epsilon_{mf}}{\phi^2\epsilon_{mf}^3} \text{ and } A_2 = \frac{1}{\phi\epsilon_{mf}^3} \qquad [2\text{-}6]$$

The functions A_1 and A_2 are shape-void functions, which Wen & Yu found to be constant over a large range of Reynolds numbers (0.001-4000) [39]. This allowed for the rearrangement of Eq 2-5 into Eq 2-7, and the definition of two constansts C_1 and C_2. Several authors have used the Wen & Yu [39] relationship to determine their own experimental constants (Table 2-1), each corresponding to their own estimations of the shape-void functions.

$$Re_{mf} = \sqrt{C_1^2 + C_2 Ar} - C_1 \qquad [2\text{-}7]$$

Table 2-1. Various C_1 and C_2 coefficients for the Wen & Yu (1966) correlation.

Author	**C_1**	**C_2**
Wen & Yu [39]	33.7	0.0408
Babu *et al.* [30]	25.25	0.0651
Grace [30]	27.2	0.0408
Chitester *et al.* [41]	28.7	0.0494
Saxena and Vogel [30]	25.3	0.0571

The experimental data obtained in this study were compared to the Wen & Yu [39] correlation for Re_{mf} using different values of C_1 and C_2 (Figure 2-3). There is a deviation in the best fitting correlation based on particle size. The smaller particle sizes ($d_{sv} \leq 109$ µm) best fit the Saxena & Vogel [30] correlation with an AARD of 10.5%, while the larger particles ($d_{sv} \geq 236$ µm) best fit the Chitester *et al.* [41] correlation with an AARD of 6.4%.

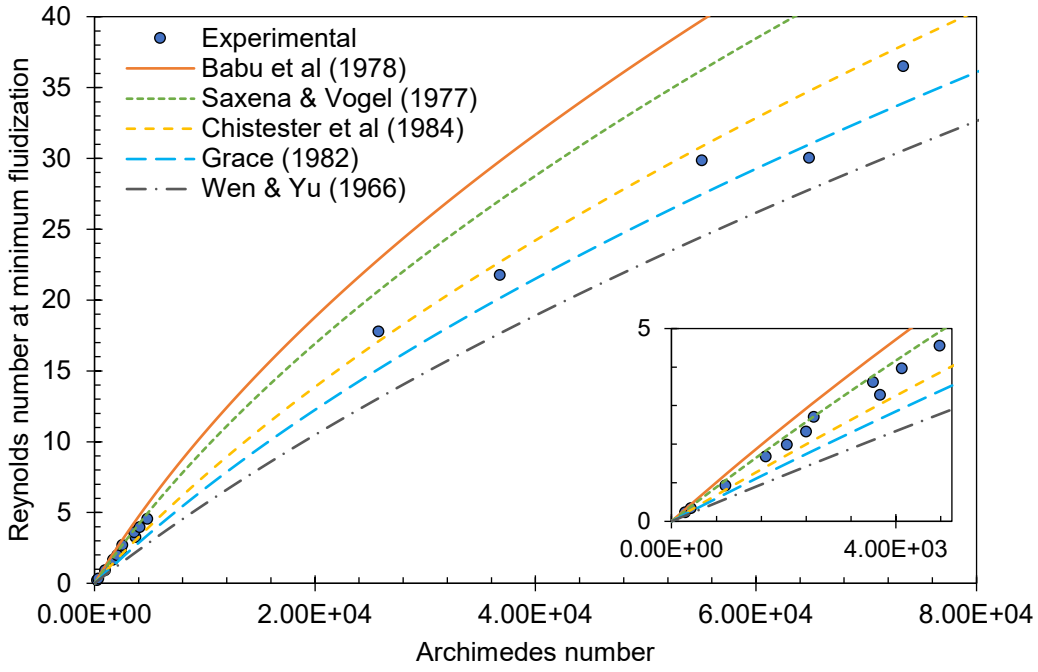

Figure 2-3. Comparison of experimental Re_{mf} to various Re_{mf} correlations.

Anatharaman *et al.* [26] found that Wen & Yu type correlations developed specifically for Geldart B particles varied in their results for U_{mf} by over an order of magnitude for the same particle conditions. The reason for such a wide distribution of predicted values can be likely attributed to the dependence of the C_1 and C_2 constants on the shape-void functions, and by extension the values for ϵ_{mf} and ϕ, as shown in Eq 2-8 and 2-9.

$$C_1 = \frac{150}{1.75}\frac{A_1}{(2A_2)} = \frac{300(1-\epsilon_{mf})}{7\phi} \quad [2\text{-}8]$$

$$C_2 = \frac{1}{1.75A_2} = \frac{\epsilon_{mf}^3\phi}{1.75} \quad [2\text{-}9]$$

For these experiments, the average ϵ_{mf} of the smaller particle sizes is 0.50, while the average ϵ_{mf} for the larger particle sizes is 0.47. Using the sphericity and experimentally derived ϵ_{mf} values, the shape-void functions for the small and large particle ranges are $A_1 \approx 6, A_2 \approx 10$, and $A_1 \approx 7, A_2 \approx 12$, respectively. Comparing these values to those presented in Table 2-2, it can be seen that the AARD for each particle range is the smallest for those correlations with similar values for the shape-void functions. Since these functions can be directly calculated by the sphericity and voidage at minimum fluidization, these values will ultimately determine the predictive accuracy of each correlation meaning that Wen & Yu [39] type correlations remain susceptible to errors in these two values, though to a lesser extent than Eq 2-1.

Table 2-2. Shape-void functions for literature U_{mf} correlations and AARD for the two particle ranges.

Author	A_1	A_2	**AARD** ($d_{sv} \leq 109$ μm)	**AARD** ($d_{sv} \geq 236$ μm)
Babu *et al* [30]	5	9	29.3%	35.6%
Saxena and Vogel [30]	6	10	10.5%	22.8%
Chitester *et al* [41]	8	12	14.6%	6.4%
Grace [30]	9	14	25.4%	9.9%
Wen & Yu [39]	11	14	39.2%	20.1%

2.4.2 Gas bubble size estimates

Figure 2-4 and Figure 2-5 present the estimated mean gas bubble sizes for the 107 μm particle size at varying pressures and excess gas velocities in the high and low bed regions, respectively. It is clear from these results that pressure has a marginal effect on gas bubble size compared to excess gas velocity. Bubble growth throughout the column increases with increasing pressure with the estimated gas bubble size increasing relative to the lower region on average by 20.5%, 32.7% and 47.0% for the 101 $kPa_{(a)}$, 600 $kPa_{(a)}$, and 1200 $kPa_{(a)}$ respectively.

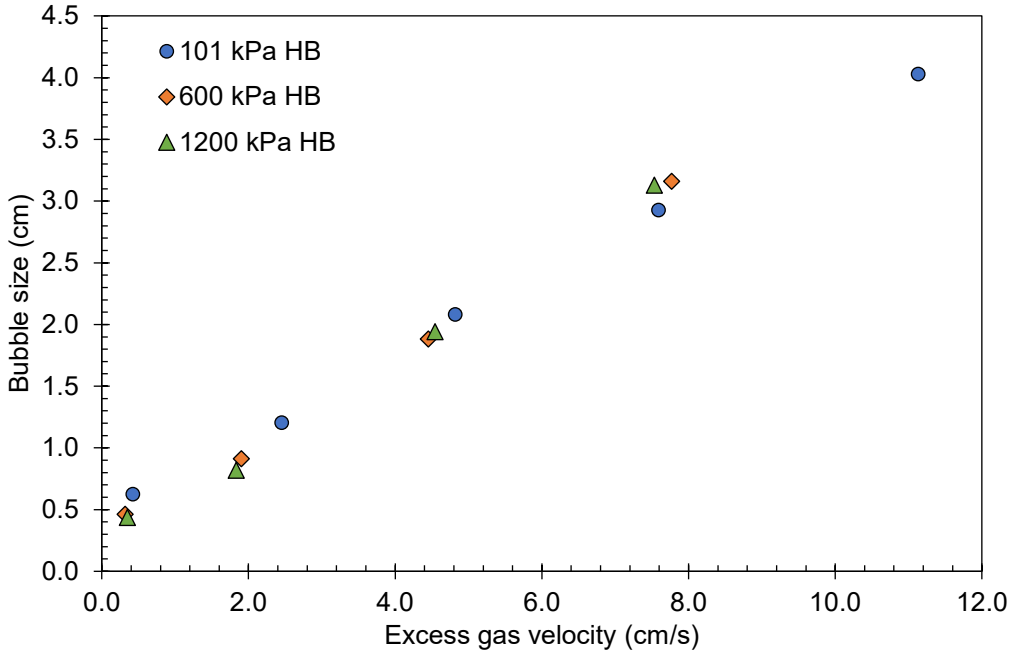

Figure 2-4. Estimated bubble size for 107 µm particle size at varying pressure and excess gas velocity in the high bed region.

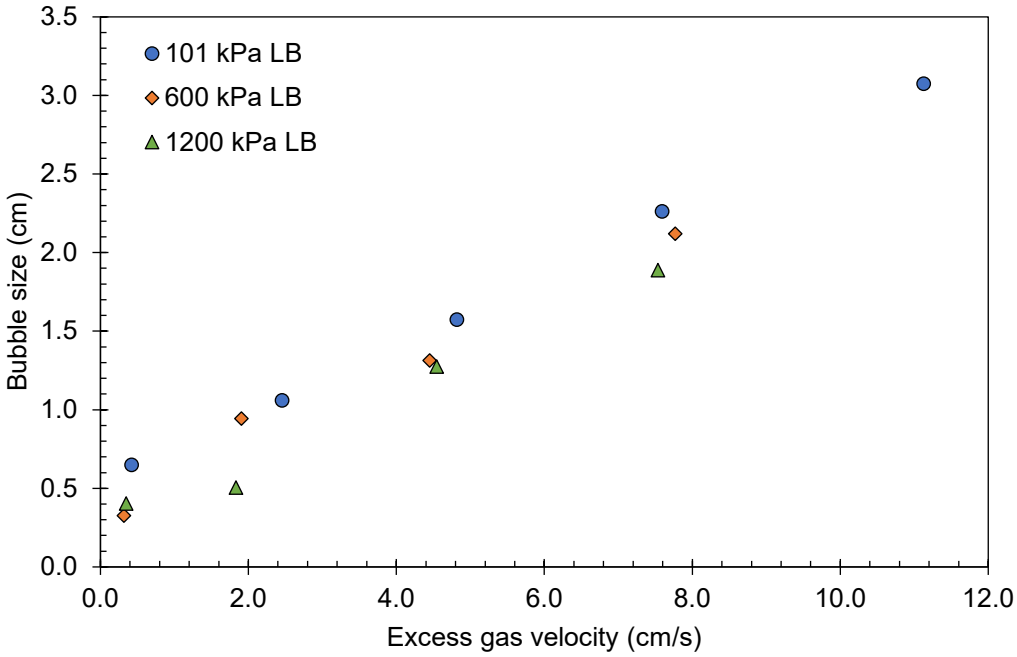

Figure 2-5. Estimated bubble size for 107 µm particle size at varying pressure and excess gas velocity in the low bed region.

A comparison of the differential pressure time series at varying pressures and excess gas velocities is shown in Figure 2-6 for the 107 µm particle size in the high bed region. At a U_e of 2.0 cm/s there is a noticeable

change in the behaviour of the signal amplitude around the average value indicating that the bubbles are decreasing in size with increasing pressure which is consistent with conclusions from the literature [42]. However, this change in amplitude is less than 1 kPa indicating that increasing the system pressure only has a minor effect on bubbling behaviour. At a higher U_e of 8.0 cm/s the change in amplitude behaviour is no longer present, and pressure has less of an effect on the bubbling behaviour. It can also be seen that the there is a wider size distribution of bubbles at all conditions, and no obvious change of bubbling frequency.

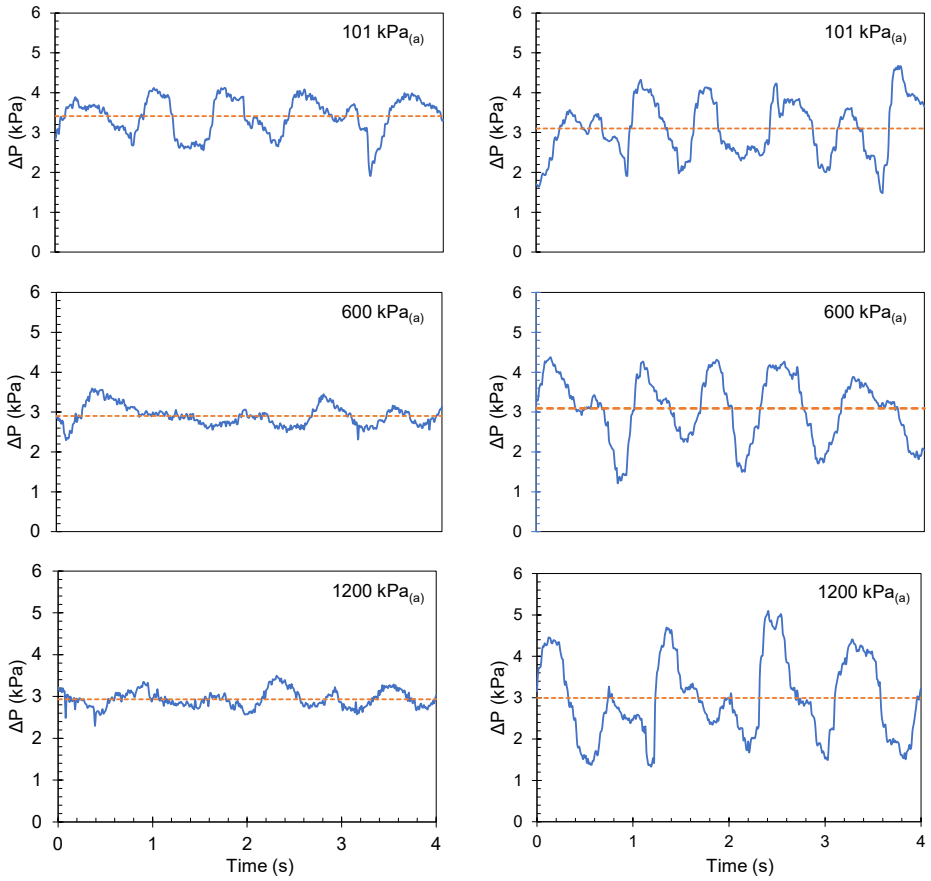

Figure 2-6. Differential pressure time series of 107 µm particles in the high bed region. Left: U_e = 2.0 cm/s. Right U_e = 8.0cm/s.

Gas bubble size correlations are well documented in the literature for a variety of operating conditions [27]. Table 2-3 outlines the various correlations explored in this study and their operating restrictions. Each correlation depends on the size of the initial bubble diameter at the distributor (d_0) which cannot be measured using the current experimental setup and therefore the commonly used Miwa *et al.* correlation (Eq 2-10) is used to estimate this value [27]. The correlation applies for perforated plate distributors.

$$d_0 = 0.347\left(\frac{A_c(U - U_{mf})}{n}\right)^{0.4} \qquad [2\text{-}10]$$

Table 2-3. Bubble size correlations for perforated plate distributors used in this work.

Author(s)	**Correlation**	**Supporting equations**	**Operating conditions**
Mori & Wen [43]	$\frac{d_{bm}-d_b}{d_{bm}-d_0}=\exp\left(-\frac{0.3H}{D}\right)$	$d_{bm}=1.87d_0$	$0.5 \le U_{mf} \le 20\ cm/s$ $60\ \mu m \le d_p \le 450 \mu m$ $U-U_{mf} \le 48\ cm/s$ $D \le 130\ cm$
Cai *et al.* [44]	$d_b=0.138H^{0.8}\left(U-U_{mf}\right)^{0.42}\exp\left(-2.5\times10^{-5}\left(U-U_{mf}\right)^2-10^{-3}\left(U-U_{mf}\right)\right)$		Geldart B particles Bubbling & Turbulent Beds $100 \le P \le 7000\ kPa$ $25 \le T \le 1000°C$
Choi *et al.* [45]	$\left(U-U_{mf}\right)(d_b-d_0)+0.474g^{0.5}\left(d_b^{1.5}-d_0^{1.5}\right)=1.132\left(U-U_{mf}\right)H$		$0.91 \le U_{mf} \le 214\ cm/s$ $41 \le d_p \le 1760\ \mu m$ $10 \le D \le 122\ cm$ $100 \le P \le 7100\ kPa$ $20 \le T \le 1000°C$
Horio & Nonaka [46]	$\left(\frac{\sqrt{d_b}-\sqrt{d_{be}}}{\sqrt{d_0}-\sqrt{d_{be}}}\right)^{\frac{1-\gamma}{\eta}}\left(\frac{\sqrt{d_b}+\sqrt{\delta}}{\sqrt{d_0}+\sqrt{\delta}}\right)^{\frac{1+\gamma}{\eta}}=\exp\left(-\frac{0.3H}{D}\right)$	$\gamma=\frac{2.56(D/g)^{0.5}}{U_{mf}}$ $\eta=\left(\gamma^2+\frac{4d_{bm}}{D}\right)^{0.5}$ $\delta=D(\gamma+\eta)^2$ $d_{be}=\frac{D}{4}(-\gamma+\eta)^2$ $d_{bm}=1.87n^{0.4}d_0$	$5.0 \le U \le 50\ cm/s$ $7.9 \le D \le 100\ cm$

Note: all units are dimensioned to centimeters and seconds

Table 2-4 presents the AARD of the four correlations tested under several operating parameters including three different particle sizes (95, 107, and 109 µm), a range of pressures from 101 to 2000 $kPa_{(a)}$, and gas velocities ranging from $1.1U_{mf}$ to $4U_{mf}$. Three of the four correlations deviate from the experimental value by more than 150%, but the Mori & Wen [43] correlation provides a more reasonable deviation of 26.4%. Figure 2-7 presents a comparison of the Mori & Wen [43] correlation results to the experimental values at varying U/U_{mf} ratios. The correlation gives the best predictions for lower ratios between $1.1U_{mf}$ and $1.6U_{mf}$, but begins to under predict the bubble size as the ratio increases.

Table 2-4. AARD of tested bubble size correlations compared to experimental data.

`Correlation	AARD
Mori & Wen [43]	26.4%
Choi *et al.* [44]	184.3%
Cai *et al.* [45]	155.5%
Horio & Nonaka [46]	160.0%

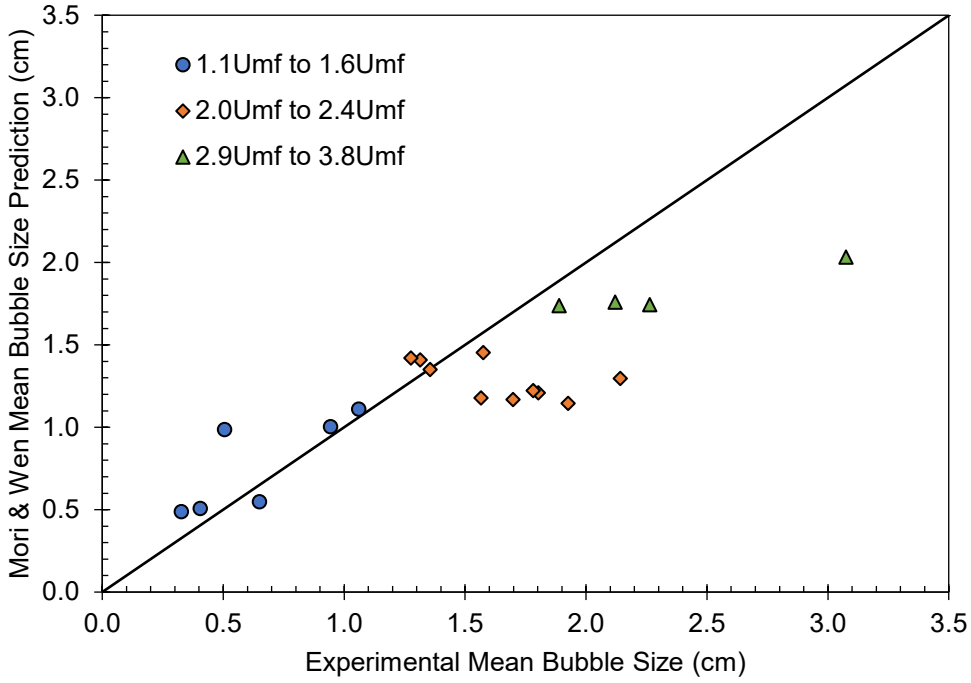

Figure 2-7. Comparison of Mori & Wen bubble size correlation to experimental data using a proportionality of one.

The comparison of the correlations to the experimental values depends largely on the proportionality constant used in Eq 2-2. The results discussed above assume a proportionality of one, however, other values

reported in literature are 1.3, and $\sqrt{3}$. Figure 2-8 compares the AARD of each tested correlation at the three different proportionality constants. It can be seen that the Mori & Wen [43] correlation consistently gives the best results, however, at the largest proportionality three of the correlations have deviations around 50%.

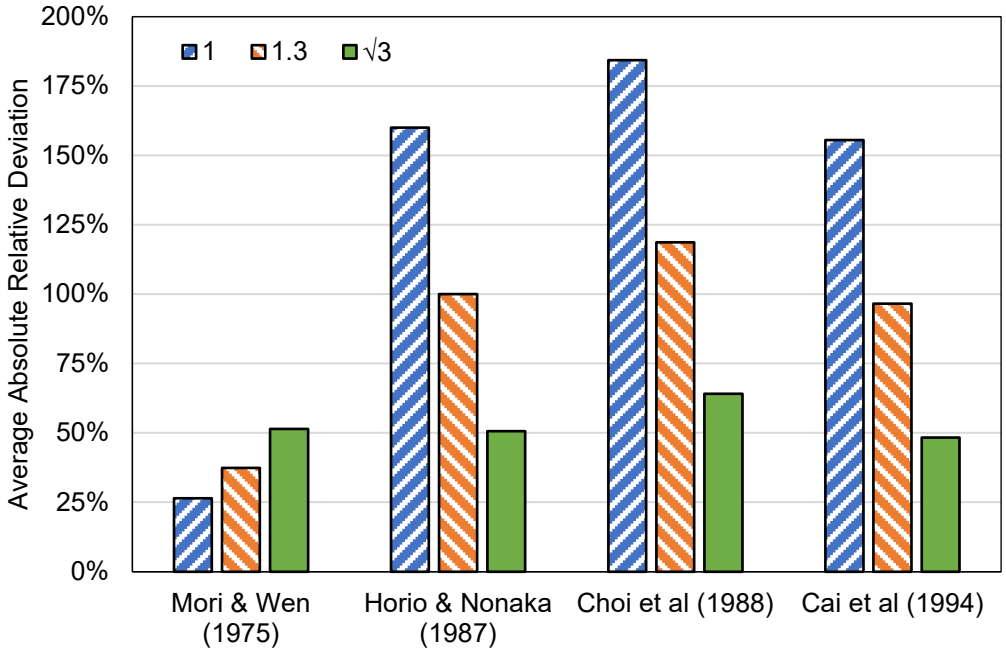

Figure 2-8. Comparison of bubble size correlation AARD with varying proportionality constants in Eq 2-2.

Results from the bubble size correlation discussion should be used with caution. Comparison of the absolute value of bubble size to different bubble size correlations is difficult due to the limitations of different bubble size measurement techniques and the resulting sensitivity that semi-empirical or empirical correlations have to their respective methodologies [27]. Further study of the effect of the experimental technique on bubble size results is recommended to properly understand the implications they have when deriving correlations from their results.

The method of measurement used in this study also has its own limitations. Should the distance between the two pressure ports be less than one half the largest bubble size, then the largest bubbles in the region will be filtered out, thereby skewing the results towards the smaller sizes [32]. However, if the spacing is too large then the pressure waves resulting from bed oscillations will not be naturally filtered out [47]. Lastly, the proportionality in Eq 2-2 is assumed constant over all operating conditions, but could be different at lower gas velocities [28]. A varying proportionality constant is more likely in Geldart A particles but

could still be a factor in these experiments. Efforts have been made in the experimental set-up to limit the uncertainty of this measurement technique as stated above.

2.4.3 Tube-to-bed Heat Transfer Coefficient

The results for the average tube-to-bed heat transfer coefficient for the 107 μm particle size at various pressures and gas velocity are shown in Figure 2-9. The heat transfer coefficient increases with gas velocity and pressure and exhibits an optimum with increasing gas velocity at atmospheric pressure and begins to plateau at higher pressures suggesting possible maxima at higher fluidization numbers $\left(U/U_{mf}\right)$. For Geldart B particles, particle convection is the dominant mode of heat transfer [48] meaning the heat transfer of these particles is determined primarily by the concentration of particles around the heat transfer tube (i.e., the local solids hold up) and the rate at which the particles are replaced, (i.e., particle mixing) [37,38]. Increased particle mixing increases heat transfer, but increased voids decreases heat transfer. These two phenomena work in opposing manners to form a maximum heat transfer coefficient as the gas flow rate is increased.

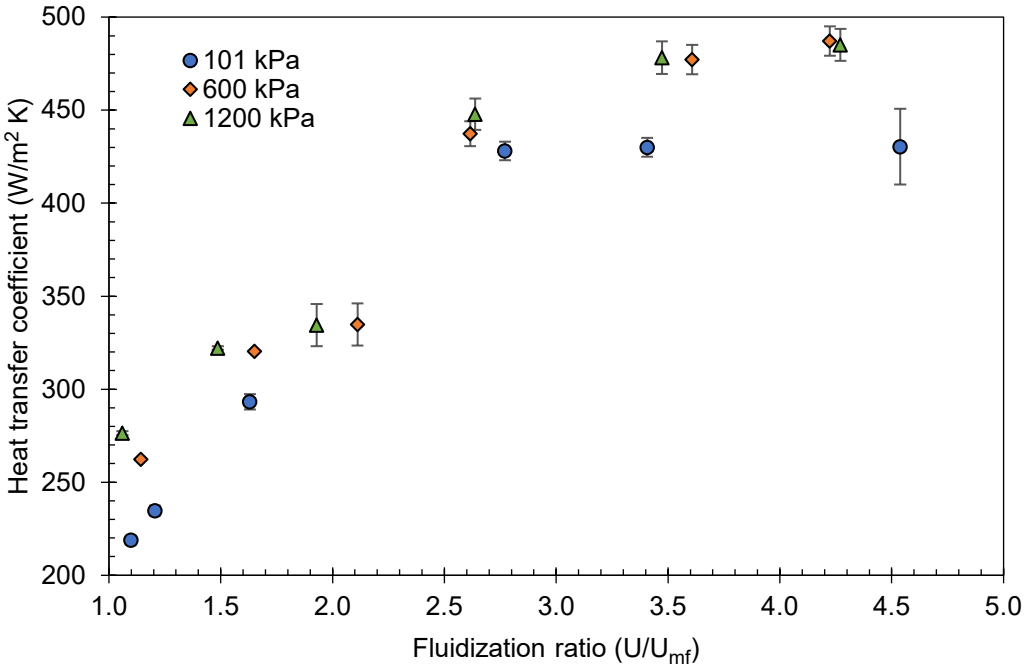

Figure 2-9. Average surface-to-bed heat transfer coefficient for tube bundle.

Pressure is known to increase the heat transfer coefficient [38,49]. For small particles the impact of pressure is mainly found through better particle convection as opposed to increased gas density. Increasing pressure increases the quality of fluidization through smaller, more evenly spatially distributed, and more frequent bubbling [38], all of which contribute to a higher solid hold up around the heat transfer surface and increased

particle mixing. This phenomenon is also evident in Figure 2-9. As pressure increases, the heat transfer coefficient also increases, and the maximum value at higher pressures occurs after that of the atmospheric experiments. Pressure, however, only has a minor effect on the heat transfer increasing the value by 10.6% from atmospheric to 600 $kPa_{(a)}$ and by 13.0% from atmospheric to 1200 $kPa_{(a)}$ at similar fluidization numbers.

The small influence of pressure likely results from the fact that the hydrodynamics for the particle bed are not heavily changed by increasing the pressure for this system. The tube bank sleeve prevents the use of differential pressure measurements to capture the hydrodynamic behaviour inside the particle bed. Furthermore, drawing conclusions from the previously discussed bubbling behaviour would be inappropriate since these results do not capture the additional effect of the internal geometry [33,50]. However, investigating the heat transfer coefficient radial profile can give some information on the hydrodynamic behaviour around the tube [37].

Figure 2-10 presents the radial heat transfer profile at $1.5U_{mf}$ and $2.3U_{mf}$ at varying pressures. The almost flat profile at the two higher pressures at $1.5U_{mf}$ indicates more homogenous fluidization relative to the atmospheric results. The $2.3U_{mf}$ profiles are more dynamic at all three pressures which alludes to greater heterogeneity of the dense and bubble phases when the gas velocity is increased [37]. The hydrodynamics of the bed change at a lower gas velocity with increasing pressure but do not change significantly when the gas velocity is increased. This is also evident in the average heat transfer coefficient where there is a greater impact of pressure at the lower gas velocities than compared to the higher gas velocities, so long as the maximum heat transfer coefficient has not yet been reached. The low impact of pressure can therefore be explained by the lack of influence that pressure has on the hydrodynamics around the heating tube.

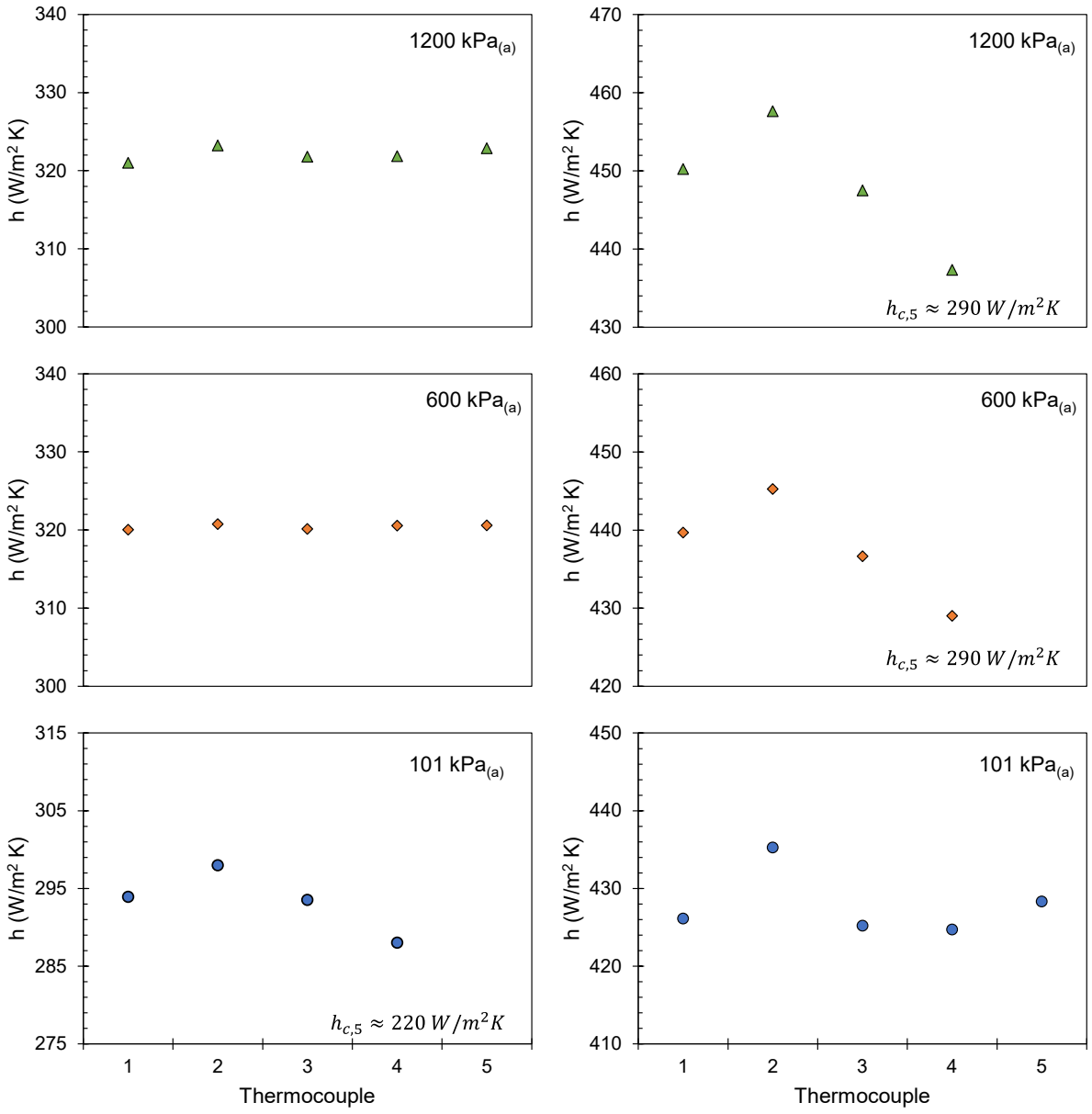

Figure 2-10. Radial profiles of heat transfer coefficient around heat transfer tube at $1.5U_{mf}$ (left) and $2.3U_{mf}$ (right).

The heat transfer coefficient at varying gas velocities and pressures for the single tube configuration is shown in Figure 2-11 to demonstrate the applicability of this tube bundle design. The heat transfer coefficient at similar fluidization numbers is higher in the single tube relative to the tube bundle by an average of 9.2% alluding to marginally better particle circulation due to the lack of surrounding tubes. Without the surrounding tubes to break-up passing gas bubbles, particle circulation will increase and therefore will increase the heat transfer coefficient. Pressure also has little impact similarly to the results

presented with the tube bundle. Again, the lack of influence pressure has the on bubbling behaviour likely causes the low influence of pressure on the heat transfer.

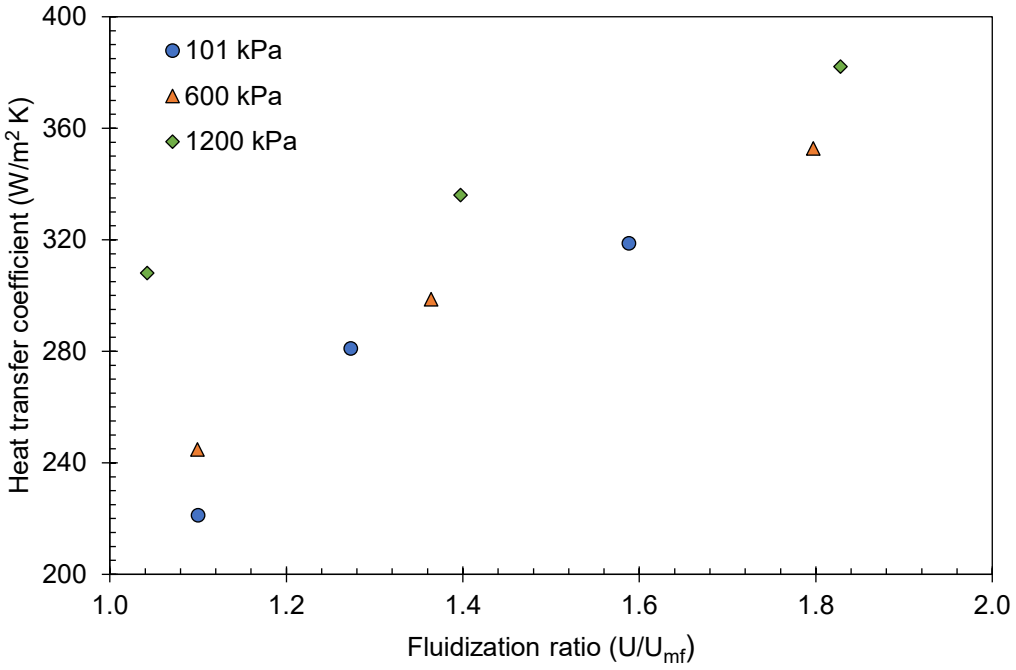

Figure 2-11. Average surface-to-bed heat transfer coefficient for single tube.

It is useful to study the predictive behaviour of available literature correlations for the tube-to-bed heat transfer coefficient. The Molerus *et al.* [51] correlation (Eq 2-11 to 2-13) for heat transfer is a semi-empirical correlation which considers both particle and gas convection (first and second terms respectively on the right hand side of Eq 2-11) on the overall heat transfer coefficient, making it a promising correlation for predicting pressurized heat transfer. The correlation was validated for particle sizes between 74 and 4000 µm, particle densities up to 11,800 kg/m^3, pressures up to 2000 kPa$_{(a)}$, and temperatures up to 1050K.

$$\frac{h_c l}{k_g} = \left[\frac{0.125\left(1-\epsilon_{mf}\right)}{1+\frac{k_g}{2c_{p,s}\mu}+d\left(U-U_{mf}\right)} \times \frac{1}{1+33.3\left[\left(\frac{U_e}{U_{mf}}\right)^{\frac{1}{3}}\left(\frac{\rho_p c_{p,s}}{k_g g}\right)^{\frac{1}{3}}U_e\right]^{-1}} \right] + 0.165\frac{Pr^{\frac{1}{3}}\left(\frac{\rho_g}{\rho_p-\rho_g}\right)^{\frac{1}{3}}}{\left[1+0.05\left(\frac{U_{mf}}{U_e}\right)\right]} \quad [2\text{-}11]$$

$$l = \left(\frac{\mu}{\rho_p-\rho_g}\right)^{\frac{2}{3}}\left(\frac{1}{g}\right)^{\frac{1}{3}} \quad [2\text{-}12]$$

$$d(U - U_{mf}) = 0.28\frac{k_g}{2c_{p,s}\mu}(1-\epsilon_{mf})^2\left(\frac{\rho_g}{\rho_p-\rho_g}\right)^{0.5}\left[\left(\frac{\rho_p c_{p,s}}{k_g g}\right)^{\frac{1}{3}}\right]^2 U_e U_{mf} \quad [2\text{-}13]$$

Furthermore, the Grewal & Saxena [48] correlation (Eq 2-14) is tested due to its recently determined applicability to ilmenite ore between 400°C and 900°C [25]. The correlation requires the knowledge of the solids hold up, and therefore correlation developed by Grewal [52] is used (Eq 2-15). The authors developed the correlation for particles diameters less than 504 µm at ambient temperature and atmospheric pressure making the dominant heat transfer mechanism particle convection. Grewal & Saxena validated the correlation for particle sizes between 136 and 1450 µm, particle densities up to approximately 5000 kg/m^3, heat transfer tube diameters of 0.0508 to 0.127 m, and temperatures up to 1373 K [48].

$$\frac{h_c d_t}{k_g} = 47(1-\epsilon)\left(\frac{\rho_p U d_t}{\mu}\frac{\mu^2}{d_{sv}^3\rho_p^2 g}\right)^{0.325}\left(\frac{\rho_p c_{p,s} d_t^{1.5} g^{0.5}}{k_g}\right)^{0.23} Pr^{0.3} \quad [2\text{-}14]$$

$$\epsilon = \frac{1}{2.1}\left[0.4 + \left(4\left(\frac{\mu U}{d_{sv}^2(\rho_p-\rho_g)\phi^2 g}\right)^{0.43}\right)^{\frac{1}{3}}\right] \quad [2\text{-}15]$$

Figure 2-12 compares the experimental heat transfer coefficient found with the tube bundle to the predicted value from the two correlations at three pressures. The Grewal & Saxena [48] correlation over predicts the heat transfer coefficient and does not have a large influence of pressure due to the small influence of gas density in correlation. The AARD for the 101 kPa$_{(a)}$, 600 kPa$_{(a)}$, and 1200 kPa$_{(a)}$ are 35.9%, 19.9%, and 17.8% respectively.

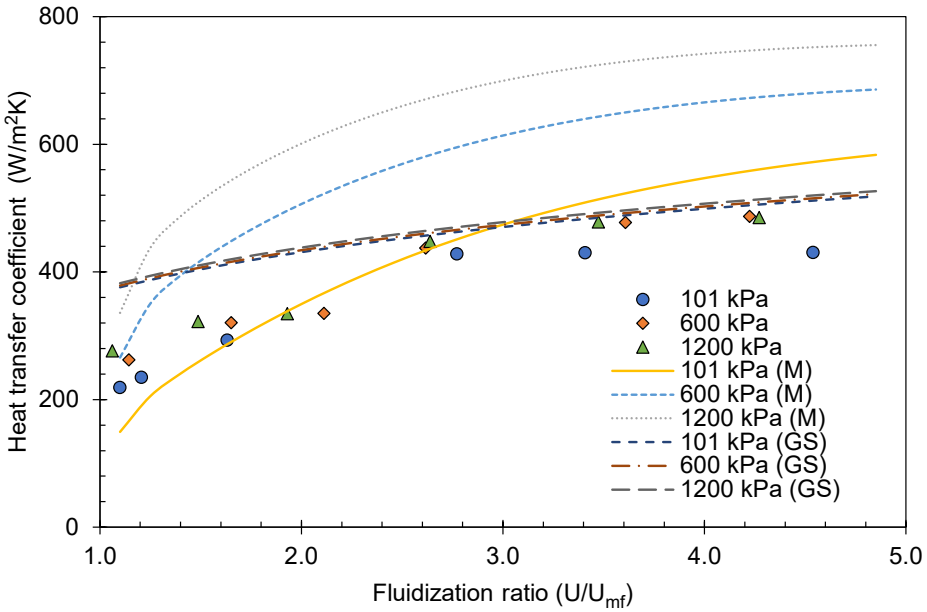

Figure 2-12. Comparison of Molerus et al (M) and Grewal & Saxena (GS) correlations to experimental heat transfer coefficient values for the tube bundle.

The Molerus *et al.* [51] correlation predicts well at 101 $kPa_{(a)}$ with an AARD of 18.9%, but over predicts with increasing pressure. The AARD increases to 37.2% at 600 $kPa_{(a)}$, and finally 49.3% at 1200 $kPa_{(a)}$. The relative contributions of gas and particle convection predicted by the correlation are not indicative of the experimental data, with the correlation attributing more impact to gas convection. Pressure will influence the gas convective contribution significantly more than the particle convection term [29] and therefore will result in increasing over predictions for this system in which the tube-to-bed heat transfer coefficient is primarily reliant on the particle convection mechanism.

2.5 Conclusions

Pressure effects were investigated on the hydrodynamics of ilmenite ore particles of varying sizes. Specifically, the minimum fluidization velocity, bed void fraction at minimum fluidization, and gas bubble size were investigated. Minimum fluidization velocity was found to remain constant for the smaller particles (95 μm and 107 μm) and decrease for the larger particles (236 μm) over fluidizing pressures of 101 $kPa_{(a)}$ to 2000 $kPa_{(a)}$. For smaller particles ($d_{sv} \leq 109$ μm) the Saxena & Vogel [30] correlation fit best, while for larger particles ($d_{sv} \geq 236$ μm) the Chistester *et al.* [41] correlation fit best. The bed void fraction at the minimum fluidization velocity was found to be 0.50 and 0.47 for the smaller and larger particles, respectively. The shape-void functions, and by extension the sphericity and bed void fraction at minimum fluidization, are also found to be the largest determinant of whether a literature correlation will accurate predict the minimum fluidization velocity.

Mean bubble size was found to be marginally impacted by pressure, but significantly affected by excess gas velocity. Differential pressure time series provided a qualitative indication that the bubble size estimates could be used with some confidence to determine experimental trends. Four correlations for bubble diameter assuming perforated plate distributors were compared to the experimental results. Most correlations deviate from the experimental results by more than 150% however, the Mori & Wen [43] correlation was found to more closely predict experimental results. The Mori & Wen [43] correlation better predicted the bubble size at lower U/U_{mf} values between 1.1 and 1.6, with higher ratios being under predicted. Further analysis of the impact of measurement techniques on correlation derivation is required.

The convective tube-to-bed heat transfer coefficient was determined at three pressures for the 107 μm particle size for both a tube bundle and single tube. A maximum value is observed as fluidization velocity is increased resulting from counteracting phenomena of decreasing local solids hold-up and increased solid mixing. Pressure was found to increase the heat transfer coefficient only marginally relative to gas flow rate. The fluidization behaviours around the tube were inferred from the local heat transfer coefficient profile along the circumference of the tube.

The Molerus *et al.* [51] and Grewal & Saxena [48] correlations were compared to the experimental heat transfer values. The Saxena & Grewal correlation over predicted the heat transfer coefficient, while the Molerus *et al.* [51] correlation matched the atmospheric values, but over predicted the pressurized results due to an overestimated contribution of heat transfer via gas convection.

Fluidized reactor design implementing ilmenite ore as an oxygen carrier can now be conducted with increased confidence at both atmospheric and pressurized conditions. Given the wide variation of literature correlation predictions presented here for fundamental design parameters, it is recommended that experimental work be conducted for those systems implementing small and dense particles at elevated pressures.

Acknowledgements

This research was partially sponsored and funded by the Natural Sciences and Engineering Research Council (NSERC) of Canada. Additional financial support was provided by the Government of Canada, Natural Resources Canada's Program for Energy Research and Development (PERD).

References

[1] W.K. Lewis, E.R. Gilliland, Production of Pure CO2, 2665972, 1954. https://patents.google.com/patent/US2665972A/en.

[2] W.K. Lewis, E.. Gilliland, M.. Sweeney, Gasification of carbon: metal oxides in a fluidized powder bed, Chem. Eng. Prog. (1951) 251–256.

[3] T. Mendiara, R. Pérez, A. Abad, L.F. De Diego, F. García-Labiano, P. Gayán, J. Adánez, Low-cost Fe-based oxygen carrier materials for the iG-CLC process with coal. 1, Ind. Eng. Chem. Res. 51 (2012) 16216–16229. https://doi.org/10.1021/ie302157y.

[4] P.C. Chiu, Y. Ku, Chemical looping process - a novel technology for inherent CO2 capture, Aerosol Air Qual. Res. 12 (2012) 1421–1432. https://doi.org/10.4209/aaqr.2012.08.0215.

[5] A. Cabello, R.W. Hughes, R.T. Symonds, S. Champagne, D.Y. Lu, E. Mostafavi, N. Manihpey, Economic Analysis of Pressurized Chemical Looping Combustion for SAGD Application, in: 5th Int. Conf. Chem. Looping, Park City, Utah, USA, 2018.

[6] S. Rana, Z. Sun, P. Mehrani, R. Hughes, A. Macchi, Ilmenite oxidation kinetics for pressurized chemical looping combustion of natural gas, Appl. Energy. 238 (2019) 747–759. https://doi.org/10.1016/j.apenergy.2019.01.126.

[7] M. Arjmand, H. Leion, T. Mattisson, A. Lyngfelt, Investigation of different manganese ores as oxygen carriers in chemical-looping combustion (CLC) for solid fuels, Appl. Energy. 113 (2014) 1883–1894. https://doi.org/10.1016/j.apenergy.2013.06.015.

[8] G.L. Schwebel, D. Filippou, G. Hudon, M. Tworkowski, A. Gipperich, W. Krumm, Experimental comparison of two different ilmenites in fluidized bed and fixed bed chemical-looping combustion, Appl. Energy. 113 (2014) 1902–1908. https://doi.org/10.1016/j.apenergy.2013.07.042.

[9] F.N. Ridha, M.A. Duchesne, X. Lu, D.Y. Lu, D. Filippou, R.W. Hughes, Characterization of an ilmenite ore for pressurized chemical looping combustion, Appl. Energy. 163 (2016) 323–333. https://doi.org/10.1016/j.apenergy.2015.10.070.

[10] F. Mayer, A.R. Bidwe, A. Schopf, K. Taheri, M. Zieba, G. Scheffknecht, Comparison of a new micaceous iron oxide and ilmenite as oxygen carrier for Chemical looping combustion with respect to syngas conversion, Appl. Energy. 113 (2014) 1863–1868. https://doi.org/10.1016/j.apenergy.2013.04.056.

[11] H. Leion, A. Lyngfelt, M. Johansson, E. Jerndal, T. Mattisson, The use of ilmenite as an oxygen carrier in chemical-looping combustion, Chem. Eng. Res. Des. 86 (2008) 1017–1026. https://doi.org/10.1016/j.cherd.2008.03.019.

[12] A. Cuadrat, A. Abad, J. Adánez, L.F. De Diego, F. García-Labiano, P. Gayán, Behavior of ilmenite as oxygen carrier in chemical-looping combustion, Fuel Process. Technol. 94 (2012) 101–112. https://doi.org/10.1016/j.fuproc.2011.10.020.

[13] N. Berguerand, A. Lyngfelt, Design and operation of a 10 kWth chemical-looping combustor for solid fuels - Testing with South African coal, Fuel. 87 (2008) 2713–2726. https://doi.org/10.1016/j.fuel.2008.03.008.

[14] L. Huang, M. Tang, M. Fan, H. Cheng, Density functional theory study on the reaction between hematite and methane during chemical looping process, Appl. Energy. 159 (2015) 132–144. https://doi.org/10.1016/j.apenergy.2015.08.118.

[15] J. Adánez, A. Cuadrat, A. Abad, P. Gayán, L.F.D. Diego, F. García-Labiano, Ilmenite activation during consecutive redox cycles in chemical-looping combustion, Energy and Fuels. 24 (2010) 1402–1413. https://doi.org/10.1021/ef900856d.

[16] Y. Tan, F.N. Ridha, M.A. Duchesne, D.Y. Lu, R.W. Hughes, Reduction Kinetics of Ilmenite Ore as an Oxygen Carrier for Pressurized Chemical Looping Combustion of Methane, Energy and Fuels. 31 (2017) 7598–7605. https://doi.org/10.1021/acs.energyfuels.7b01038.

[17] Y. Tan, F.N. Ridha, D.Y. Lu, R.W. Hughes, Reduction Kinetics of Ilmenite Ore for Pressurized Chemical Looping Combustion of Simulated Natural Gas, Energy and Fuels. 31 (2017) 14201–14210. https://doi.org/10.1021/acs.energyfuels.7b02648.

[18] R.T. Symonds, R.W. Hughes, D.Y. Lu, P. Navarri, O. Ashrafi, Systems analysis of pressurized chemical looping combustion for SAGD applications, Int. J. Greenh. Gas Control. 73 (2018) 111–123. https://doi.org/10.1016/j.ijggc.2018.03.008.

[19] H. Thunman, F. Lind, C. Breitholtz, N. Berguerand, M. Seemann, Using an oxygen-carrier as bed material for combustion of biomass in a 12-MWth circulating fluidized-bed boiler, Fuel. 113 (2013) 300–309. https://doi.org/10.1016/j.fuel.2013.05.073.

[20] A. Corcoran, J. Marinkovic, F. Lind, H. Thunman, P. Knutsson, M. Seemann, Ash properties of ilmenite used as bed material for combustion of biomass in a circulating fluidized bed boiler, Energy and Fuels. 28 (2014) 7672–7679. https://doi.org/10.1021/ef501810u.

[21] F. Lind, A. Corcoran, H. Thunman, Validation of the oxygen buffering ability of bed materials used for OCAC in a large scale CFB boiler, Powder Technol. 316 (2017) 462–468. https://doi.org/10.1016/j.powtec.2016.12.048.

[22] M. Hanning, A. Corcoran, F. Lind, M. Rydén, Biomass ash interactions with a manganese ore used as oxygen-carrying bed material in a 12 MWth CFB boiler, Biomass and Bioenergy. 119 (2018) 179–190. https://doi.org/10.1016/j.biombioe.2018.09.024.

[23] C. Kajnäs, M. Hedberg, H. Leion, The Effect of Iron- and Manganese-Based Oxygen Carriers as Bed Materials in Oxygen Carrier Aided Combustion, Energy Technol. 7 (2019) 1–13. https://doi.org/10.1002/ente.201900321.

[24] M. Rydén, M. Hanning, F. Lind, Oxygen Carrier Aided Combustion (OCAC) of wood chips in a 12 MWth circulating fluidized bed boiler using steel converter slag as bed material, Appl. Sci. 8 (2018). https://doi.org/10.3390/app8122657.

[25] V. Stenberg, V. Sköldberg, L. Öhrby, M. Rydén, Evaluation of bed-to-tube surface heat transfer coefficient for a horizontal tube in bubbling fluidized bed at high temperature, Powder Technol. 352 (2019) 488–500. https://doi.org/10.1016/j.powtec.2019.04.073.

[26] A. Anantharaman, R.A. Cocco, J.W. Chew, Evaluation of correlations for minimum fluidization velocity (Umf) in gas-solid fluidization, Powder Technol. (2018). https://doi.org/10.1016/j.powtec.2017.10.016.

[27] S. Karimipour, T. Pugsley, A critical evaluation of literature correlations for predicting bubble size and velocity in gas-solid fluidized beds, Powder Technol. (2011). https://doi.org/10.1016/j.powtec.2010.09.016.

[28] M. Rüdisüli, T.J. Schildhauer, S.M.A. Biollaz, A. Wokaun, J. Ruud van Ommen, Comparison of bubble growth obtained from pressure fluctuation measurements to optical probing and literature correlations, Chem. Eng. Sci. 74 (2012) 266–275. https://doi.org/10.1016/j.ces.2012.01.045.

[29] F. Li, E. Mielke, R.W. Hughes, M. Fitzsimmons, A. Macchi, P. Mehrani, Heat transfer in a pressurized fluidized bed with continuous addition of fines, Powder Technol. (2019) 12. https://doi.org/10.1016/j.powtec.2019.08.078.

[30] J. Grace, Fluidized Bed Hydrodynamics, in: Handb. Multiph. Flow, McGraw-Hill, Washington,DC, 1982: p. 970.

[31] S. Ergun, Fluid flow through Packed Columns, Chem. Eng. Prog. 48 (1952) 89–94.

[32] M. Liu, Y. Zhang, H. Bi, J.R. Grace, Y. Zhu, Non-intrusive determination of bubble size in a gas-solid fluidized bed: An evaluation, Chem. Eng. Sci. 65 (2010) 3485–3493. https://doi.org/10.1016/j.ces.2010.02.049.

[33] M. Séguin, Fuel Residence Times for Clean Combustion of Coal in a Pressurized Fluidized Bed - Cold Flow Study, (2017) 140.

[34] J.R. van Ommen, S. Sasic, J. Van Der Schaaf, S. Gheorghiu, F. Johnsson, M.-O. Coppens, Time-series analysis of pressure fluctuations in gas–solid fluidized beds – A review, Int. J. Multiph. Flow. 37 (2011) 403–428. https://doi.org/10.1016/j.ijmultiphaseflow.2010.12.007.

[35] J.R. van Ommen, R.F. Mudde, Measuring the Gas-Solids Distribution in Fluidized Beds - A Review, Int. J. Chem. React. Eng. 6 (2008). https://doi.org/10.2202/1542-6580.1796.

[36] J.R. Van Ommen, J.C. Schouten, M.L.M. Stappen, C.M. Van Den Bleek, Response Characteristics of probe-transducer systems for pressure measurements in gas-solid fluidized beds: how to prevent pitfalls in dynamic pressure measurements, Powder Technol. 106 (1999) 199–218.

[37] S.W. Kim, J.Y. Ahn, S.D. Kim, D. Hyun Lee, Heat transfer and bubble characteristics in a fluidized bed with immersed horizontal tube bundle, Int. J. Heat Mass Transf. 46 (2003) 399–409. https://doi.org/10.1016/S0017-9310(02)00296-X.

[38] S.W. Kim, S.D. Kim, Heat transfer characteristics in a pressurized fluidized bed of fine particles with immersed horizontal tube bundle, Int. J. Heat Mass Transf. 64 (2013) 269–277. https://doi.org/10.1016/j.ijheatmasstransfer.2013.04.045.

[39] C.Y. Wen, Y.H. Yu, A Generalized Method for Predicting the Minimum Fluidization Velocity, AIChE J. (1966) 610–612.

[40] W. Yang, D.C. Chitester, R.M. Kornosky, D.L. Keairns, A generalized methodology for estimating minimum fluidization velocity at elevated pressure and temperature, AIChE J. 31 (1985) 1086–1092. https://doi.org/10.1002/aic.690310706.

[41] D.C. Chitester, R.M. Kornosky, L.S. Fan, J.P. Danko, Characteristics of fluidization at high pressure, Chem. Eng. Sci. (1984). https://doi.org/10.1016/0009-2509(84)80025-1.

[42] J.G. Yates, Effects of Temperature and Pressure on Gas-Solid Fluidization, Chem. Eng. Sci. 51 (1996).

[43] S. Mori, C.Y. Wen, Estimation of bubble diameter in gaseous fluidized beds, AIChE J. 21 (1975) 109–115. https://doi.org/10.1002/aic.690210114.

[44] P. Cai, M. Schiavetti, G. De Michele, G.C. Grazzini, M. Miccio, Quantitative estimation of bubble size in PFBC, Powder Technol. 80 (1994) 99–109. https://doi.org/10.1016/0032-5910(94)02834-6.

[45] J.H. Choi, J.E. Son, S.D. Kim, Bubble size and frequency in gas fluidized beds, J. Chem. Eng. Japan. 21 (1988) 171–178. https://doi.org/10.1252/jcej.21.171.

[46] M. Horio, N. Akira, A generalized bubble diameter correlation for gas-solid fluidized beds, AIChE J. 33 (1987) 1865–1872. https://doi.org/10.1002/aic.690331113.

[47] Y. Zhang, H. Bi, J.R. Grace, C. Lu, Comparison of decoupling methods for analyzing pressure fluctuations in gas-fluidized beds, Am. Insitute Chem. Eng. 56 (2010) 869–877.

[48] N.S. Grewal, S.C. Saxena, Heat transfer between a horizontal tube and a gas-solid fluidized bed, Int. J. Heat Mass Transf. 23 (1980) 1505–1519. https://doi.org/10.1016/0017-9310(80)90154-4.

[49] J.S.M. Botterill, M. Desai, Limiting factors in gas-fluidized bed heat transfer, Powder Technol. 6 (1972) 231–238. https://doi.org/10.1016/0032-5910(72)83017-1.

[50] S. Olsson, J. Wiman, A.E. Almstedt, Hydrodynamics of Pressurizred Fluidized Bed with Horizontal Tubes: Influence of Pressure, Fluidization Velocity, and Tube-Bank Geometry, Chem. Eng. Sc. 50

(1995) 581–592.

[51] O. Molerus, A. Burschka, S. Dietz, Particle migration at solid surfaces and heat transfer in bubbling fluidized beds-I. Particle migration measurement systems, Chem. Eng. Sci. 50 (1995) 871–877. https://doi.org/10.1016/0009-2509(94)00445-W.

[52] N.S. Grewal, Experimental and Theoretical Investigations of Heat Transfer between a Gas-Solid Fluidized Bed and Immersed Tubes, University of Illinois at Chicago Circle, 1979.

Chapter 3 CPFD modeling of high pressure bubbling fluidized bed hydrodynamics using ilmenite particles

C. J. McIntyre[a], R.W. Hughes[b], A. Macchi[a*], P. Mehrani[a*]

[a] Department of Chemical and Biological Engineering, University of Ottawa, 161 Louis Pasteur Street, Ottawa, ON, Canada, K1N 6N5

[b] Natural Resources Canada, CanmetENERGY, 1 Haanel Drive, Ottawa, ON, Canada, K1A 1M1

[*]*Corresponding authors email.* Arturo Macchi arturo.macchi@uottawa.ca*;* Poupak Mehrani: poupak.mehrani@uottawa.ca

Chapter 3 is a manuscript to be submitted for journal publication

Abstract

The multiphase particle-in-cell (MP-PIC) approach was used to model the hydrodynamics of five different ilmenite particle size distributions in a high pressure cylindrical fluidized bed. The model was created using the commercial software Barracuda Virtual Reactor® and validated against previously obtained experimental data. The model was able to replicate the experimental results for minimum fluidization velocity and was found to be dependent on the model input close pack factor. A close pack factor of 0.58 resulted in the best alignment between model and experiments with an average absolute deviation (AARD) of 3.9%. Trends in bed expansion with fluidization ratio and pressure were well represented by the model, but the simulation consistently underpredicted experimental values by an average of 4.8%. The model was able to demonstrate the expected trends for the bubble size distribution with change in relation to fluidization ratio, pressure, and elevation. The mean bubble diameter calculated by the model deviated on average by 18.7% from the experimental results. The Mori & Wen correlation for bubble growth was adapted to the mean bubble diameter growth determined from the model resulting in an AARD of 22%.

Keywords: Multiphase Particle-in-Cell, bubbling fluidization, pressurized fluidized-bed, Computational Particle Fluid Dynamics (CPFD)

Nomenclature

Variables	
$\boldsymbol{A}$	Discrete particle acceleration (m/s^2)
C_d	Drag Coefficient (-)
D	Drag Function (s^{-1})
D_1	Wen-Yu Drag Function (s^{-1})
D_2	Ergun Drag Function (s^{-1})
D_b	Bubble diameter (cm)
$\overline{D_b}$	Mean bubble diameter (cm)
$D_{b,max}$	Maximum bubble diameter in distribution (cm)
ΔP	Pressure differential (kPa)
Δz	Height differential (m)
$\boldsymbol{F}$	Interphase rate of momentum transfer (N)
f	Particle distribution function (-)
$f(D_b)$	Probability density function at given bubble size (-)
$\boldsymbol{g}$	Acceleration due to gravity (m/s^2)
H	Bed height (m)
K	Proportionality constant (Eq 3-16)
m	Mass (kg)
N	Number of orifices in distributor plate (-)
p	Pressure (Pa)
P_s	Solids Pressure term (Eq 3-7) (Pa)
Re	Reynolds Number $= \frac{2\rho_f r_s \lvert \boldsymbol{u_f} - \boldsymbol{u_s} \rvert}{\mu_f}$ (-)
r_s	Particle radius (m)
t	Time (s)
U	Superficial gas velocity (m/s)
$\boldsymbol{u}$	Velocity (m/s)
$\boldsymbol{x}$	Position (m)
Greek Letters	
β	Solids stress function term (Eq 3-7) (-)
ε	Solids stress function term (Eq 3-7) (-)
μ	1st statistical moment (mean) (cm), viscosity (Pa s)
ρ	Density (kg/m^3)
σ	2nd statistical moment (standard deviation) (cm)
$\boldsymbol{\tau}$	Stress tensor (Pa)
θ	Volume fraction (-)

Subscripts	
ΔP	Pressure differential
f	Fluid phase
$fixed$	Fixed bed conditions
$fluidized$	Fluidized bed conditions
mf	Minimum fluidization
s	Solid phase
Acronyms	
AARD	Average Absolute Relative Deviation $= \frac{1}{n}\sum \frac{\lvert x_{experimental} - x_{predicted} \rvert}{x_{experimental}} \times 100\%$
AR	Air Reactor
CCUS	Carbon Capture, Utilization, and Sequestration
CFD	Computational Fluid Dynamics
CLC/R	Chemical Looping Combustion / Reforming
CPFD	Computation Particle Fluid Dynamics
FR	Fuel Reactor
KTGF	Kinetic Theory of Granular Flow
MP-PIC	Multiphase Particle-in-Cell
OC	Oxygen Carrier
TFM	Two Fluid Model
XRF	X-Ray Fluorescence

Note: vector quantities are bolded

3.1 Introduction

Chemical looping combustion and reforming (CLC/R) have emerged in recent years to be promising next generation carbon capture, utilization, and sequestration (CCUS) technologies to produce clean heat, steam, and hydrogen [1–3]. CLC/R operates on the fundamentals of oxyfuel combustion but incorporate oxygen carriers (OC) to provide inherent oxygen production in place of using an air separation unit [3]. The OC is looped between two separate reaction chambers, denoted as the air and fuel reactors (AR and FR respectively), in which the OC undergoes cyclic oxidation and reduction reactions. Oxidation occurs within the AR and reduction occurs within the FR, thereby providing the necessary oxygen for fuel combustion without direct contact of fuel with air. Ilmenite ore is a promising candidate for an OC given its favourable thermodynamic properties and high reactivity with syngas [4–6]. Ilmenite exhibits relatively low reactivity with methane at atmospheric pressure [7–9], but the reactivity can be improved by increasing the partial pressure of methane through increased operating pressure [10–12]. In addition, increased operating pressures have been shown to have many technical and economic benefits to the full CLC/R processes [13,14].

Computational fluid dynamic (CFD) modeling has become an increasingly useful tool for investigating the hydrodynamics of gas-solid fluidized beds [15]. The technique allows for extensive exploration of conditions that could otherwise be too difficult or expensive to conduct experimentally such as in the cases of high pressure or high temperature operation. Furthermore, CFD can give insights into fluidized bed properties that would be difficult to determine in an experimental setting. There are two traditional frameworks for CFD modeling of fluidized beds [16,17]: 1) Eulerian-Eulerian Framework and 2) Eulerian-Lagrangian Framework.

The Eulerian-Eulerian framework, also referred to as the Two Fluid Model (TFM), represents both the fluid and particle phases as interpenetrating continua [18]. The behaviour of the two phases are modeled using their respective volume averaged mass and momentum balances. Closure terms are determined based on the Kinetic Theory of Granular Flow (KTGF) [18,19] and sub-models for particle drag, phase interactions, and geometry interactions [16,18]. The TFM approach allows for efficient modeling of large volumes but sacrifices the resolution of the particle phase since it treats the entire phase as a single entity. Separate equations would be required for each particle diameter to model polydisperse systems which would in turn increase the computational demand. There are concerns with how well the TFM can represent meso-scale structures such as gas bubbles and clusters within a fluid bed, particularly for Geldart type A particles [17].

The Eulerian-Lagrangian framework differs from the Eulerian-Eulerian approach by modeling the particle phase using discrete entities. The movement of particles is calculated by solving the Newtonian equations

of motion for each entity allowing for simpler modeling of polydisperse systems, but at a cost to computational efficiency since each individual entity must tracked throughout the simulation [16,20].

The multiphase particle-in-cell (MP-PIC) approach [21–23], also referred to as the computational particle fluid dynamic (CPFD) method, aims to mitigate the high computational demand of Eulerian-Lagrangian methods by grouping particles with similar properties (mass, velocity, position, etc.) into computational parcels and treating the solid phase as both discrete entities and a continuum. Particle phase properties are either solved in a Eulerian or Lagrangian framework, depending on the property. For example, particle stresses are difficult to calculate for individual particles in dense particle loadings (>5wt%) [22], so the MP-PIC method uses an Eulerian framework to calculate particle stress gradients, and then maps the stress to the discrete particles using linear interpolation operators [21,22]. As such, the MP-PIC method can efficiently model systems with large numbers of particles without sacrificing particle phase resolution excessively.

Barracuda Virtual Reactor ® is a commercial software that employs the MP-PIC method to model fluid-particle systems. It has been used to explore a wide variety of systems including bubbling fluidized beds [17,24–32], fluidized bed risers [33–37] and downcomers [38], full circulating fluidized beds [39–43], and dual interconnected circulating fluidized beds [44–47]. Most of these works compared MP-PIC results with experimental findings through qualitative comparison of flow structures or quantitative results with reasonable amounts of success.

In particular, the MP-PIC method has been validated considering a wide range of atmospheric pressure bubbling fluidized bed data for minimum fluidization, bed expansion, and bubble size distributions. Amarasinghe et al. [26] and Jayarathna [27] successfully modeled the minimum fluidization of Geldart type A, B, and D particles using the MP-PIC method under ambient temperature and pressure. Shao et al [24] extended their work by validating the method using minimum fluidization data obtained at high operating temperatures and pressures, and demonstrated the expected trends in minimum fluidization with particle size, particle density, operating pressure, and operating temperature. Solnordal et al [28] applied the modeling approach to simulate a two chamber internally circulating bubbling fluidized bed. They compared both quantitative results for particle circulation rate and qualitative bubbling behaviour around the heat exchanger bundles with reasonable success. Karimipour & Pugsley [25], and Vashisth et al [17] found the MP-PIC method could accurately predict the bed expansion of Geldart type A particles without modification to the drag law they had implemented. Park et al [32] were able to model the segregation of char particles in a bubbling fluidized bed using various distributor nozzle arrangements. Lastly, Fotovat et al [29] found that the MP-PIC approach could reasonably predict the bubble size distributions, as well as the first, second and third statistical moments (mean, standard deviation, and skewness respectively) of the

distribution for a biomass-sand bubbling fluidized bed operating under ambient conditions and various biomass loadings.

This work evaluates the applicability of the MP-PIC method in modeling the hydrodynamics of a pressurized bubbling fluidized bed operating with ilmenite particles that are relatively small, high density Geldart type B particles. Specifically, this work aims to explore the ability of the MP-PIC method to predict appropriate trends and values for minimum fluidization velocity, bed expansion, and mean bubble size in a pressurized bubbling fluidized bed without significant alteration to the default input values. The results are validated using previously obtained experimental values [48]. Analyses of the simulated bubble size distributions and bubble size growth rates were also performed to demonstrate how the MP-PIC method can explore other fluidized bed properties not recorded by the experimental set-up. Barracuda Virtual Reactor ® v17.4.1 is used to perform the simulations.

3.2 Experimental program

Details of experimental set-up and experimental results are explained elsewhere [48,49]. Briefly, the system contains a 2.8 m tall cylindrical, high-pressure fluidized bed column with an internal diameter of 0.15 m. The distributor is a perforated plate containing 61 holes of 6 mm diameter. Differential pressure taps are located at various heights along the column. The bed is split into two vertical regions for bubble size measurements denoted as the mid and high bed regions. The mid bed region begins at a height of 0.17 m and ends at 0.32 m, while the high bed region begins at a height of 0.32 m and ends at 0.47 m. Experimental results of tests in which ilmenite was fluidized at high pressure [48] are compared with the modeling results obtained in this work. The specific conditions considered, and the data collected are presented in Table 3-1.

Table 3-1. Experimental operating ranges and measurements compared with modeling results.

Sauter Mean Particle Diameter (µm)	**Operating Pressure(s) (kPa)**	**Fluidization Ratio(s)* (U/U_{mf})**	**Measurements**		
			Minimum Fluidization Velocity	Bed Expansion	Mean Bubble Diameter
95	101 - 2000	2.0 – 2.4	X	X	X
107	101 - 1200	1.1-3.8	X	X	X
109	700	2.0	X	X	X
236	101 - 2000	N/A	X		
321	700	N/A	X		

*Fluidization ratios for bed expansion and mean bubble size measurements

3.3 Model description

3.3.1 Multiphase particle-in-cell method governing equations

The MP-PIC approach models the fluid phase as a continuum using the volume averaged Navier-Stokes equations on a Eulerian grid [21–23]. The fluid phase continuity equation and momentum balance are shown in Eq 3-1 & 3-2, respectively. The rate of interphase momentum transfer, $\boldsymbol{F}$, is described by Eq 3-3.

$$\frac{\partial(\theta_f \rho_f)}{\partial t} + \boldsymbol{\nabla} \cdot \left(\theta_f \rho_f \boldsymbol{u_f}\right) = 0 \quad [3\text{-}1]$$

$$\frac{\partial(\theta_f \rho_f \boldsymbol{u_f})}{\partial t} + \boldsymbol{\nabla} \cdot \left(\theta_f \rho_f \boldsymbol{u_f} \boldsymbol{u_f}\right) = -\boldsymbol{\nabla} p - \boldsymbol{F} + \theta_f \rho_f \boldsymbol{g} + \boldsymbol{\nabla} \cdot (\theta_f \boldsymbol{\tau_f}) \quad [3\text{-}2]$$

$$\boldsymbol{F} = \iint f m_s \left[D_s\left(\boldsymbol{u_f} - \boldsymbol{u_s}\right) - \frac{1}{\rho_s} \boldsymbol{\nabla} p \right] dm_s d\boldsymbol{u_s} \quad [3\text{-}3]$$

The solid phase is described using a particle distribution function (Eq 3-4). The particle distribution function is the local number density of particles multiplied by the local probability distribution function of particle properties that are important to the application, for example the mass and velocity of particles, m_s and $\boldsymbol{u_s}$. Therefore, Eq 3-4 describes the average number density of particles at a given location and time with mass in the interval $(m_s + dm_s)$ and velocity in the interval $(\boldsymbol{u_s} + d\boldsymbol{u_s})$.

$$f(\boldsymbol{x}, m_s, \boldsymbol{u_s}, t) dm_s d\boldsymbol{u_s} \quad [3\text{-}4]$$

Taking the time rate of change of Eq 3-4 gives a Liouville equation, a mathematical expression for the conservation of particle numbers (Eq 3-5), which conserves the number of particles within each parcel volume as they move along the trajectories in particle phase space.

$$\frac{\partial f}{\partial t} + \boldsymbol{\nabla_x} \cdot (f \boldsymbol{u_s}) + \boldsymbol{\nabla_{u_s}} \cdot (f \boldsymbol{A}) = 0 \quad [3\text{-}5]$$

The particle acceleration, $\boldsymbol{A}$, is calculated using Eq 3-6. The terms in Eq 3-6 explain the particle acceleration due to aerodynamic drag, pressure gradient, gravity, and interparticle stresses. The MP-PIC method inherently models particle size distributions since it solves the full particle distribution function, and the drag term in Eq 3-6, D_s, implicitly couples the fluid and solid phases [22].

$$\boldsymbol{A} = D_s\left(\boldsymbol{u_f} - \boldsymbol{u_s}\right) - \frac{1}{\rho_s} \boldsymbol{\nabla} p + \boldsymbol{g} - \frac{1}{\theta_s \rho_s} \boldsymbol{\nabla} \tau_s \quad [3\text{-}6]$$

In conserving particle numbers (Eq 3-5) the assumption is made that there is no particle break-up or particle-particle collisions. Instead, the collective influence of neighbouring particles on the particle acceleration is

approximated by the normal particle stress function (Eq 3-7). The function is calculated on the Eulerian grid using the particle close pack factor, θ_{CP}, before being mapped to the discrete particle entities by employing linear interpolation operators between the gird and particle positions. The close pack value is defined as the maximum volume fraction of the particles within a given cell. The particle stress function is based on the stress function of Harris & Crighton [50], but the denominator has been modified to avoid a singularity when the particle volume fraction equals the close pack value. As the solids volume fraction approaches a close packed state, the influence of neighbouring particles on particle acceleration approaches its maximum, making the close pack factor a highly influential parameter for dense phase flows. The close pack value is influenced by the particle size distribution and particle shape making the value somewhat arbitrary according to Snider [21].

$$\tau_s = \frac{P_s \theta_s^{\beta}}{\max[\theta_{CP} - \theta_s, \varepsilon(1-\theta_s)]} \quad [3\text{-}7]$$

3.3.2 Drag model

The drag model used in this work is the blended Wen-Yu/Ergun drag model (Eq 3-8) based on previous works modeling bubbling fluidized beds using the MP-PIC method [17,24–28]. The model uses the local solids volume fraction to calculate a weighted average of the Wen-Yu (Eq 3-9 & 3-10) and Ergun (Eq 3-11) drag models between solids volume fractions of $0.75\theta_{CP}$ and $0.85\theta_{CP}$. When solids concentrations are below this range, the Wen-Yu model is used to calculate the drag, while the Ergun model is used when the solids concentration is above the interval. This model can therefore predict the change in drag forces due to local solids volume fraction making it well suited to model the lean and dense phases of a bubbling fluidized bed. It should be noted the drag law is also influenced by the close pack value.

$$D = \begin{cases} D_1 & \theta_s < 0.75\theta_{CP} \\ (D_2 - D_1)\dfrac{(\theta_s - 0.75\theta_{CP})}{0.85\theta_{CP} - 0.75\theta_{CP}} + D_1 & 0.75\theta_{CP} \le \theta_s \le 0.85\theta_{CP} \\ D_2 & \theta_s > 0.85\theta_{CP} \end{cases} \quad [3\text{-}8]$$

$$D_1 = \frac{3}{8}\frac{C_d \rho_f |\boldsymbol{u_f} - \boldsymbol{u_s}|}{\rho_s r_s} \quad [3\text{-}9]$$

$$C_d = \begin{cases} \dfrac{24}{Re}\theta_f^{-2.65} & Re < 0.5 \\ \dfrac{24}{Re}\theta_f^{-2.65}(1.0 + 0.15Re^{0.687}) & 0.5 \le Re \le 1000 \\ 0.44\theta_f^{-2.65} & Re > 1000 \end{cases} \quad [3\text{-}10]$$

$$D_2 = 0.5\frac{\left(\dfrac{180\theta_s}{\theta_f Re} + 2\right)\left(\rho_f |\boldsymbol{u_f} - \boldsymbol{u_s}|\right)}{\rho_s r_s} \quad [3\text{-}11]$$

3.3.3 Model geometry and boundary conditions

The computational mesh is shown in Figure 3-1. Only the lower half of the 2.8 m long column is constructed in the mesh since the maximum static bed height used in the experiments was approximately 0.5 m and particle elutriation was not observed during experiments. The truncation of the column allowed for a higher concentration of cells within the fluidized bed given computational restraints. A pressure boundary condition is defined at the top of the mesh and is set equal to the desired operating pressure. The initial conditions of the system are stagnant air, and either 25 kg of solids for the three smallest particle sizes or 9.8 kg of solids for the two largest to emulate the experimental conditions. The particle size distributions used in the model were determined through sieve analysis of the particles used in the experiments. The ilmenite particles were modeled on its constituent compounds in its oxidized form determined from XRF analysis [14]: 30.7wt% Fe_2O_3, 45.4wt% Fe_2TiO_5, 21.4wt% TiO, 2.5wt% inert material (assumed SiO_2). The other important model parameters (Table 3-2) are taken from the default and recommended values by the software developers [51]. All simulations are completed under isothermal conditions at 300 K.

Table 3-2. Model parameters used in this work.

Parameter Name	Value
Gravity, m/s^2	9.81
Close pack value	0.58
Maximum momentum redirection from collision	40%
Normal-to-wall momentum retention	0.85
Tangent-to-wall momentum retention	0.85
Diffuse Bounce	0
P_s (Eq 3-7), Pa	10
β (Eq 3-7)	3
ε (Eq 3-7)	1e-08
Turbulence model	Large Eddy Simulation

The fluidizing air is injected uniformly through 61 injection points located at the base of the mesh to replicate the perforated plate distributor. A given air mass flow rate is held constant for 5 seconds to achieve steady-state conditions, and then data is collected for an additional 5 seconds. For a more in depth explanation of the high pressure CPFD model refer to Appendix B.

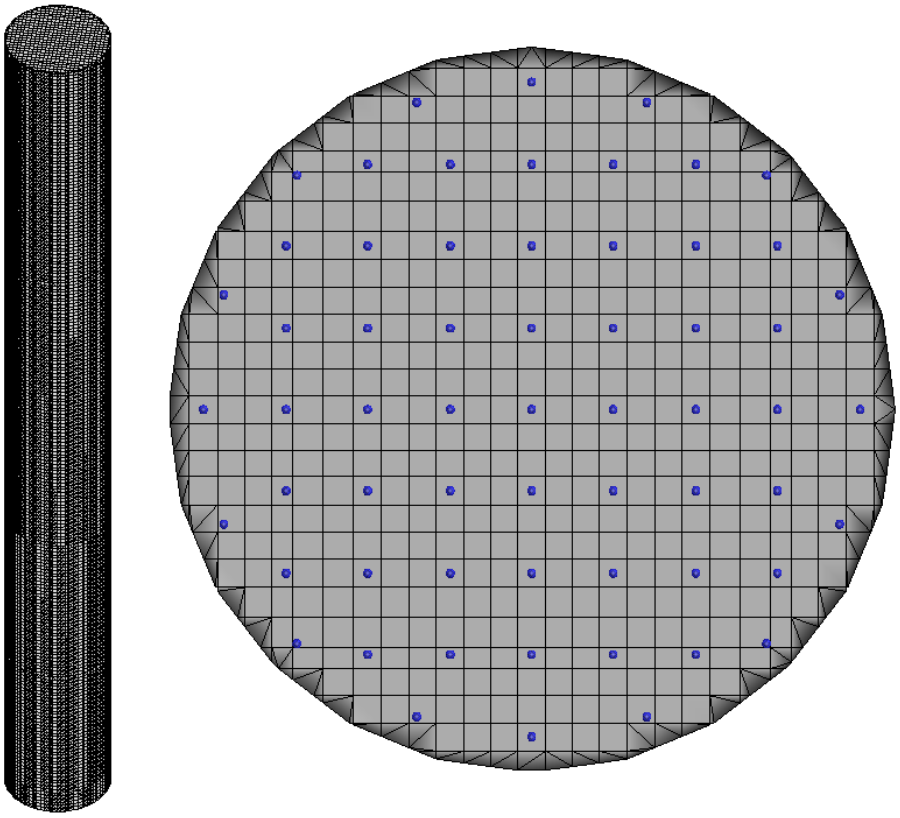

Figure 3-1. Computational mesh of the high-pressure cylindrical bubbling fluidized bed with fluid injection points shown.

The influence of the mesh on the model results was tested by comparing the axial pressure drop profile and axial average solids volume fraction profile at three different mesh resolutions: 106,329 cells (coarse), 139,948 cells (medium), and 180,900 cells (fine). The absolute average relative deviation (AARD) in average solids volume fraction between the coarse and medium resolution mesh is approximately 10%, whereas from the medium to fine mesh the AARD is less than 1% at any axial location. Similarly, the pressure drop axial profile presented an AARD of less than 0.5% between the medium and fine mesh. For computational efficiency, the medium mesh resolution was thus selected for future work.

3.4 Results and discussion

3.4.1 Minimum fluidization

The minimum fluidization velocity was determined using the pressure drop method for both the experiments and model [52]. The pressure drop over the entire fluidized bed (ΔP) is measured at various superficial gas velocities. The gas velocity is first increased to overcome the hysteresis often found using this method, and then decreased. The data for the decreasing superficial gas velocity is then used to

determine the minimum fluidization velocity through the intersection of the lines plotted to approximate the pressure drop under fixed bed and fluidized bed conditions (Figure 3-2). Note, calculation of model results is performed with a decreasing gas flow rate in order to reduce calculation time.

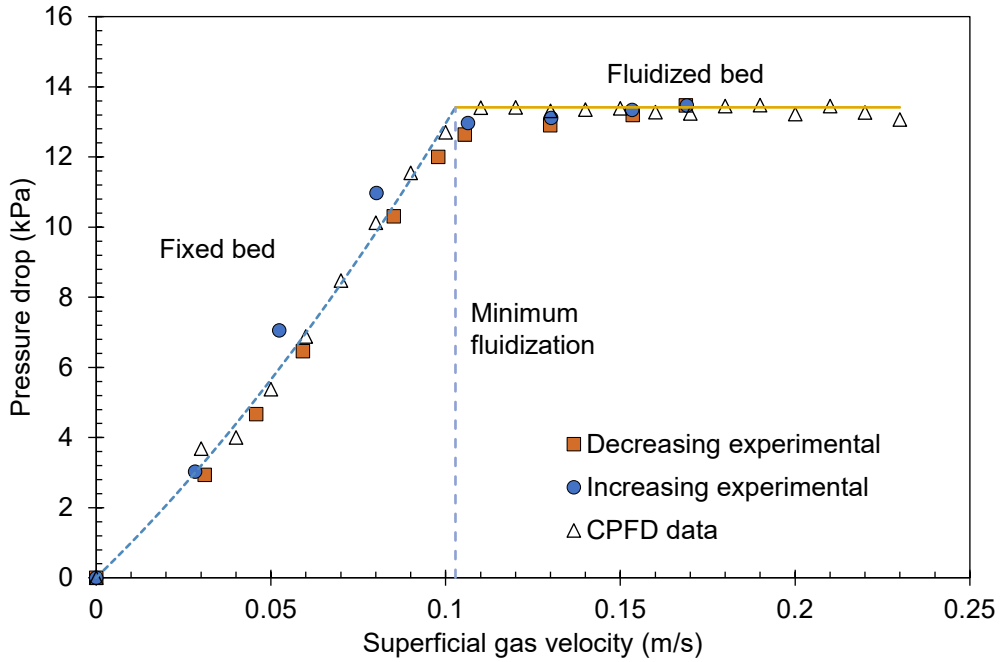

Figure 3-2. Method of determining minimum fluidization velocity. Results for 236 µm particles at 2000 kPa shown.

The importance of the close pack factor in determining an accurate minimum fluidization velocity through the model should be noted. The value of the close pack factor influences the pressure loss in the fixed bed region since the pressure loss in the fluidized bed region is only dependent on the weight of the suspended particle bed. As the close pack factor increases, the pressure drop in the fixed bed will increase causing a steeper slope in the fixed bed line, therefore the intersection of the fixed and fluidized bed lines will shift to lower superficial gas velocities. The predicted minimum fluidization velocity will therefore decrease as the close packing factor increases.

Two experimental conditions were selected to determine the appropriate close pack value for the model (Table 3-3). The close packing factor was varied between the recommended values of 0.55 to 0.60 [51], with results presented in Figure 3-3. For both experimental conditions evaluated, a close packing factor of 0.58 resulted in the lowest relative error between the model and experimental results. An AARD of 2.6% and 1.8% were calculated for experiments A and B, respectively.

Table 3-3. Experimental conditions for subset to determine close pack value.

Operating Condition	Experiment A	Experiment B
Sauter Mean Particle Diameter (µm)	95	236
Operating Pressure (kPa)	2000	1000
Bed Mass (kg)	25	9.8

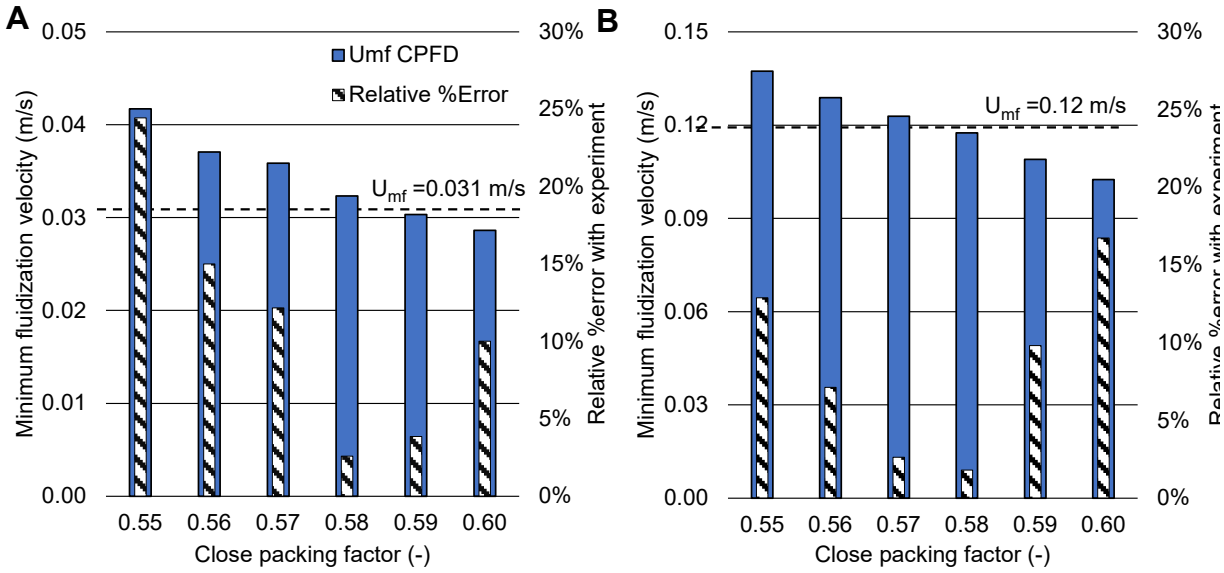

Figure 3-3. Predicted minimum fluidization values for A) 95µm at 2000 kPa and B) 236 µm at 1000 kPa for various close packing factors.

Applying a close pack value of 0.58 to the full set of conditions results in accurate predictions of the minimum fluidization velocity (Figure 3-4). The model predicted the decrease of minimum fluidization velocity with pressure for larger particle size, and a lack of influence of pressure for smaller particles in accordance to literature [24,48,52–54]. The model predicted the full set of experimental values within an average absolute relative deviation of 3.9%. The AARDs in order of increasing particle sizes are 4.2%, 4.4%, 2.0%, 2.8%, and 9.1%, showing little change in the accuracy of the model with particle size except for the largest particles. The model accuracy also is independent of the operating pressure, varying from and AARD of 1.5% to 6.6% over the range modeled.

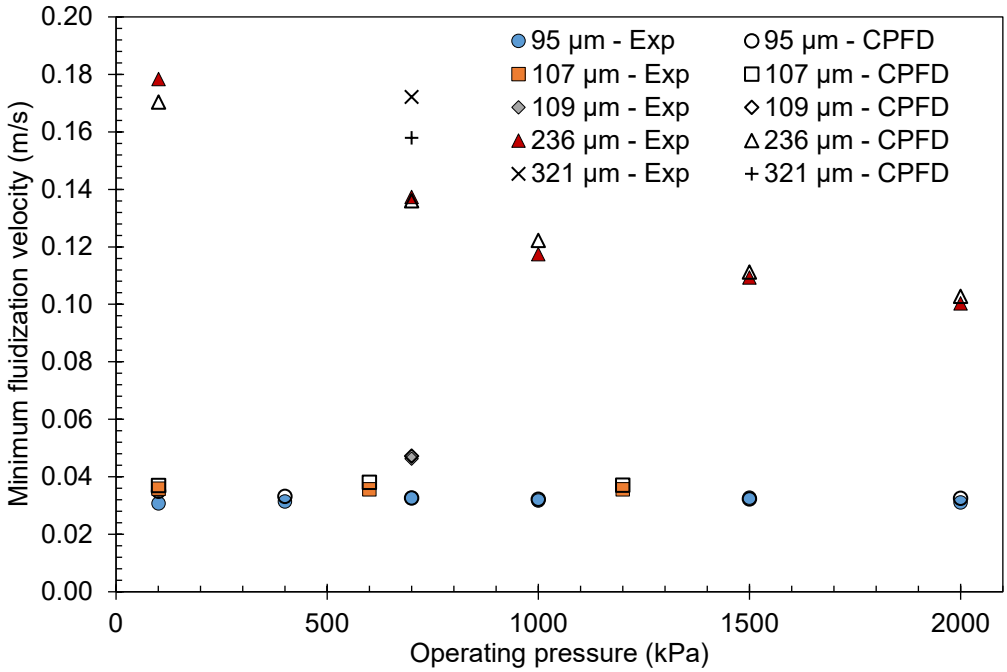

Figure 3-4. Comparison of experimental (Exp) and model (CPFD) predicted minimum fluidization values.

3.4.2 Bed expansion

Bed expansion was measured experimentally using the relationship between in-bed differential pressure measurements and bed height as shown in Eq 3-12 & 3-13. A distance of 0.3 m was used between the pressure ports, Δz, and the fixed bed solids volume fraction, $\varepsilon_{s,fixed}$ was taken as the close pack factor of 0.58.

$$\frac{H_{fluidized}}{H_{fixed}} = \frac{\varepsilon_{s,fixed}}{\varepsilon_{s,fluidized}} \quad [3\text{-}12]$$

$$\varepsilon_{s,fluidized} = 1 - \frac{\Delta P}{g(\rho_s - \rho_g)\Delta z} \quad [3\text{-}13]$$

The bed expansion predicted by the model was determined by spatially averaging the solids volume fraction over a plane at various axial locations. A plot of the solids volume fraction *versus* height was created, and the fluidized bed height was determined to be the height at which the solids volume fraction is zero. The fixed bed height was determined in an identical way when the fluidizing gas mass flow was set to zero.

Figure 3-5 compares the experimental and simulated bed expansion results as they vary with fluidizing ratio and operating pressure for the 107 µm mean particle size. The model results generally under predicted the experimentally determined expansion but reflected the observed trends. As the fluidization ratio increases,

more gas flows into the bubble phase which in turn increases the expansion through an increase in gas bubble holdup. Furthermore, McIntyre *et al* [48] found little impact of pressure (for the same range operated here) on the bed expansion of these particles, which is reflected in the model results.

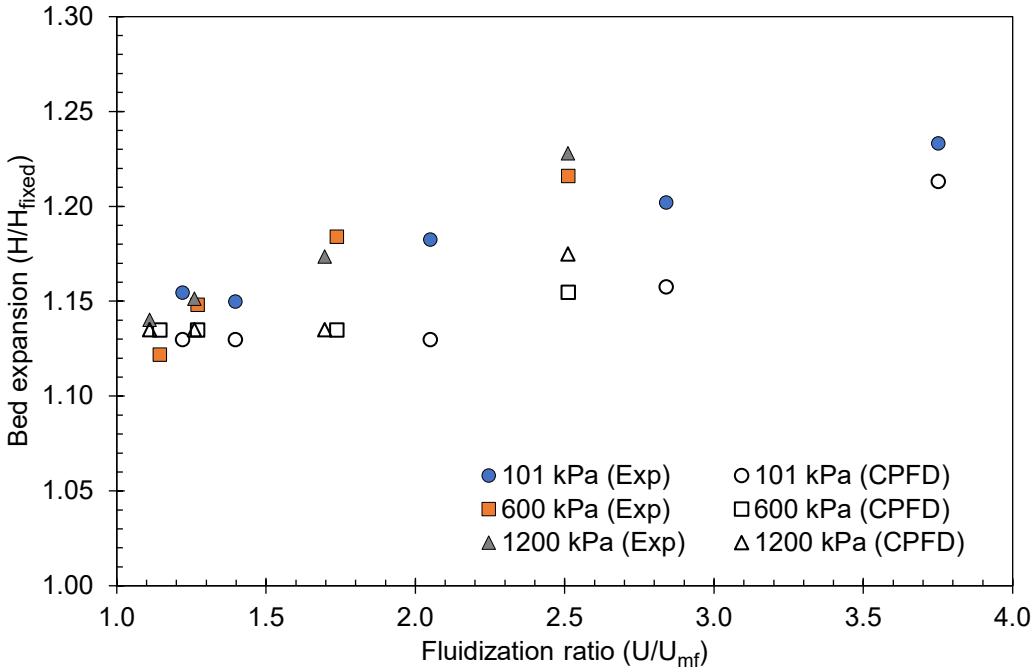

Figure 3-5. Comparison of experimental (Exp) and model (CPFD) results considering bed expansion with varying pressure and fluidizing ratio for a mean particle diameter of 107 µm.

Comparing the full set of experimental and model results for the three measured particle sizes (Figure 3-6) shows a general under prediction by the model. However, the AARD between the model and all the experimental values was 4.8%, meaning the model reflected the system well. It should be noted that the 95 µm average particle size resulted in greater errors, but still gave reasonable results (AARD of 9.5%). Better predictions for the bed expansion could be achieved by fine tuning the other input parameters but would limit the extension of the model to other operating conditions and is therefore not investigated here.

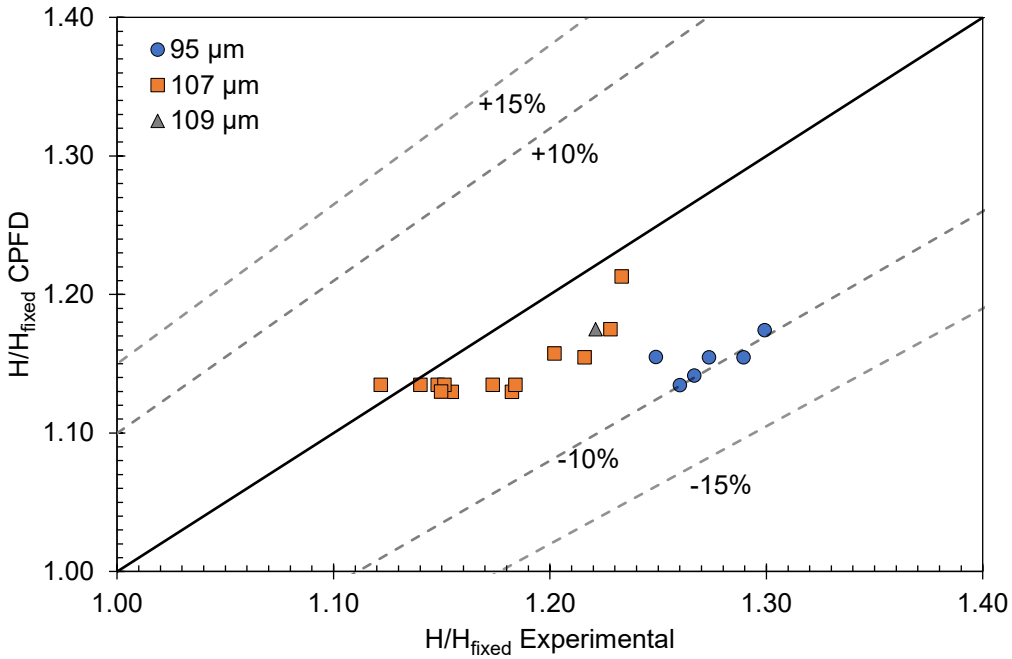

Figure 3-6. Comparison of bed expansion experimental data set to CPFD results. Percentages show relative deviation with 45° line.

3.4.3 Gas bubbles

3.4.3.1 Size distribution

Images of axial planes were used to determine the bubble size distributions from the model (Figure 3-7). Images were taken at multiple radial locations and time steps to determine a representative size distribution. A contour of the solids volume fraction was first produced and then masked to produce a high contrast image by using a threshold solid volume fraction of 0.4 to denote the edges of gas bubbles. The image processing software ImageJ was then used to calculate the projected area of the bubbles from the masked image, and a final bubble size was determined by calculating the diameter of an area-equivalent circle. It should be noted that the area used to calculate the diameter was the maximum area projection of a given bubble. This was accomplished by comparing the projected areas of a given bubble at various radial locations and using the maximum value for area. The bubbles were tracked along the radius by their height. The vertical location of the gas bubble was determined by the location of the bubble center [48]. The first and second statistical moments of the number distribution (Eq 3-14 & 3-15) were used to calculate an average bubble diameter and the broadness of the distribution, respectively. Note, since the recorded data is not continuous, the discrete forms of Eq 3-14 & 3-15 with bin sizes (ΔD_{b_i}) of 1.0 cm, and the midpoint value of a given bin is used as the bubble size (D_{b_i}).

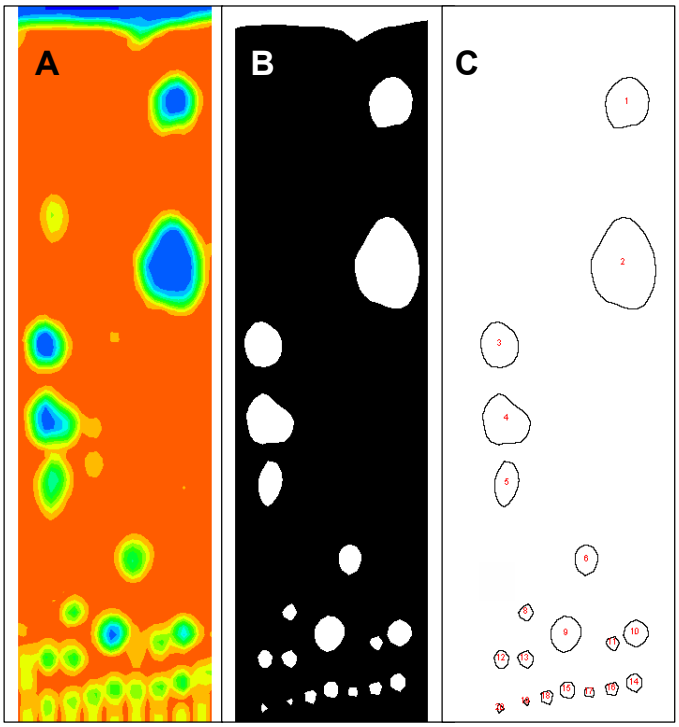

Figure 3-7. CPFD gas bubble analysis procedure for 107 µm particles operating at 600 kPa and a superficial velocity of 2.2 Umf. A) Particle volume fraction contour image showing gas bubbles B) High contrast masked image of projected bubble areas C) ImageJ analysis of gas bubble edges.

$$\mu = \overline{D_b} = \frac{\int_0^{D_{b,max}} f(D_b)\, D_b dD_b}{\int_0^{D_{b,max}} f(D_b)\, dD_b} = \frac{\sum_0^{D_{b,max}} f(D_{b_i}) D_{b_i} \Delta D_{b_i}}{\sum_0^{D_{b,max}} f(D_{b_i}) \Delta D_{b_i}} \quad [3\text{-}14]$$

$$\sigma = \left[\frac{\int_0^{D_{b,max}} f(D_b)\,(D_b - \overline{D_b})^2\, dD_b}{\int_0^{D_{b,max}} f(D_b)\, dD_b}\right]^{0.5} = \left[\frac{\sum_0^{D_{b,max}} f(D_{b_i})\,(D_{b_i} - \overline{D_b})^2\, \Delta D_{b_i}}{\sum_0^{D_{b,max}} f(D_{b_i}) \Delta D_{b_i}}\right]^{0.5} \quad [3\text{-}15]$$

Figure 3-8 displays the model bubble size distribution in different height intervals of the fluidized bed. Note the last two intervals correspond to the experimental mid and high bed regions. The distributions shift to larger bubble sizes along the height of the column due to bubble coalescence, which adheres to literature trends [52,53]. The coalescence is demonstrated by the broadening of the distribution and the appearance of larger bubble sizes in the higher bed regions. Furthermore, the model shows that bubble growth occurs primarily in the lowest region of the bed. Mean bubble diameter increases from the first to second interval by 167% on average but only increase by 22% from the fifth to sixth interval. Lastly, the high number of bubble diameters in the range of 0.0 to 1.0 cm in the lowest region of the bed indicate the presence of a relatively uniform initial bubble size just above the distributor, which can also be seen visually in Figure 3-7.

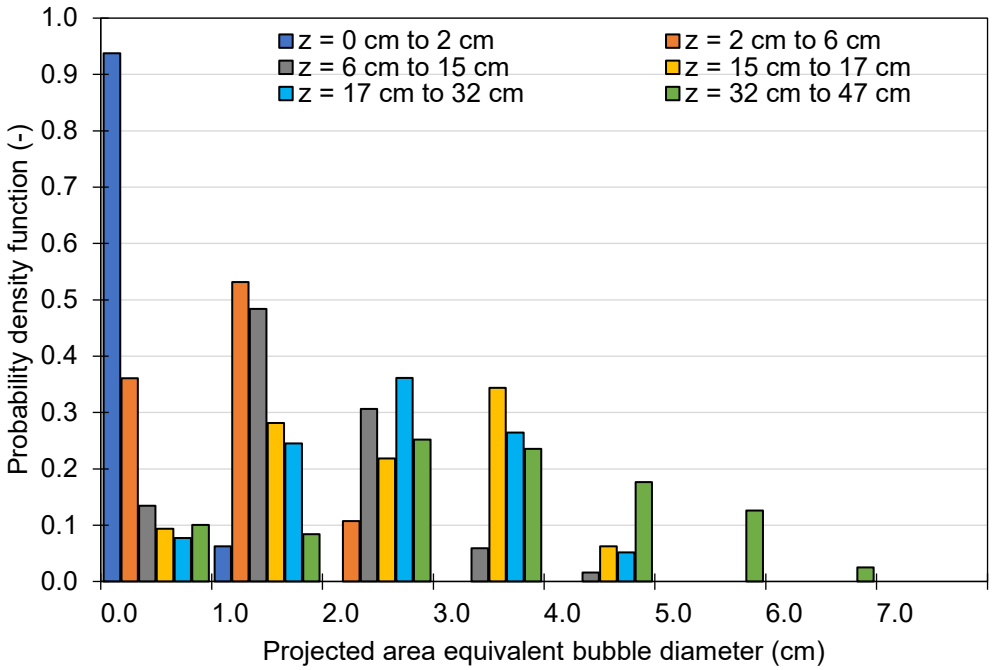

Figure 3-8. Bubble size distribution along the fluidized bed height for the 107 µm particles, operating at 2.2U_{mf} and 101 kPa.

Similarly, Figure 3-9 demonstrates the effect of fluidization velocity on bubble size distribution, showing an increase in the breadth of the bubble size distribution with velocity, as well as the mean bubble diameter. This effect is evident by the appearance of larger bubbles (D_b >5 cm) at 2.2 and 3.8 U_{mf}, and the overall broadening of the distribution at the increased gas velocities. When the fluidization velocity is increased from 1.6 U_{mf} to 2.2 U_{mf}, the mean bubble diameter increases by 28.2% and the standard deviation of the distribution increases by 51.1%. Increasing the superficial gas velocity to 3.8 U_{mf} further increases the mean and standard deviation of the distribution by 30.3% and 44.6% respectively.

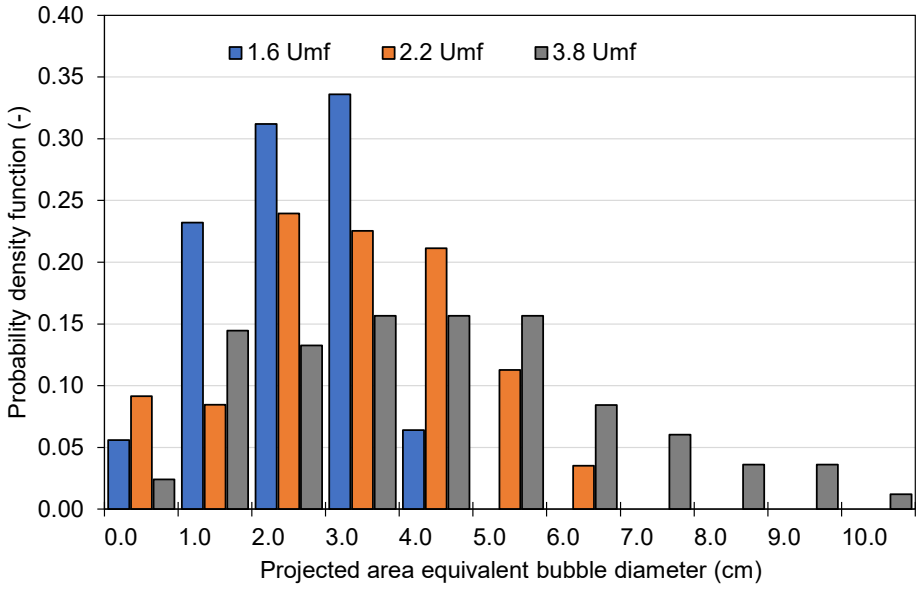

Figure 3-9. Bubble size distribution at three fluidization velocities in the high bed region for the 107 µm particles at 600 kPa.

Figure 3-10 shows a marginal effect of operating pressure on the distribution relative to the effects of axial location and fluidization velocity. There was found to be no statistical difference in the means between any pressure. This lack of impact of pressure on the mean bubble size is also reported in the experimental results [48].

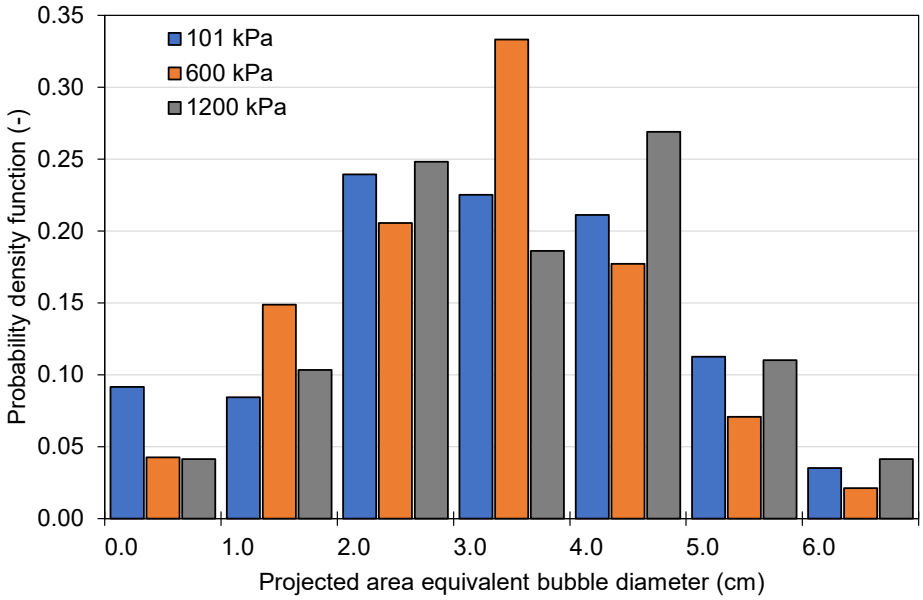

Figure 3-10. Bubble size distribution at three operating pressures in the high bed region for the 107 µm particles at 2.1 U_{mf}.

3.4.3.2 Gas bubble size validation

The experimentally derived mean gas bubble diameters were determined using the proportionality relationship in Eq 3-16 [55], where the proportionality constant, K, has been reported to be 1 [55], 1.3, or √3 [56] for Geldart type B particles. Figure 3-11 compares the model results against the experimental data when a value of √3 was used as the proportionality constant. The model predicts the mean bubble size with an AARD of 18.7% which is consistent with deviations found in literature for MP-PIC models [29].

$$\overline{D_b} = K \frac{\sigma_{\Delta P}}{g(1-\varepsilon_{mf})\rho_p} \qquad [3\text{-}16]$$

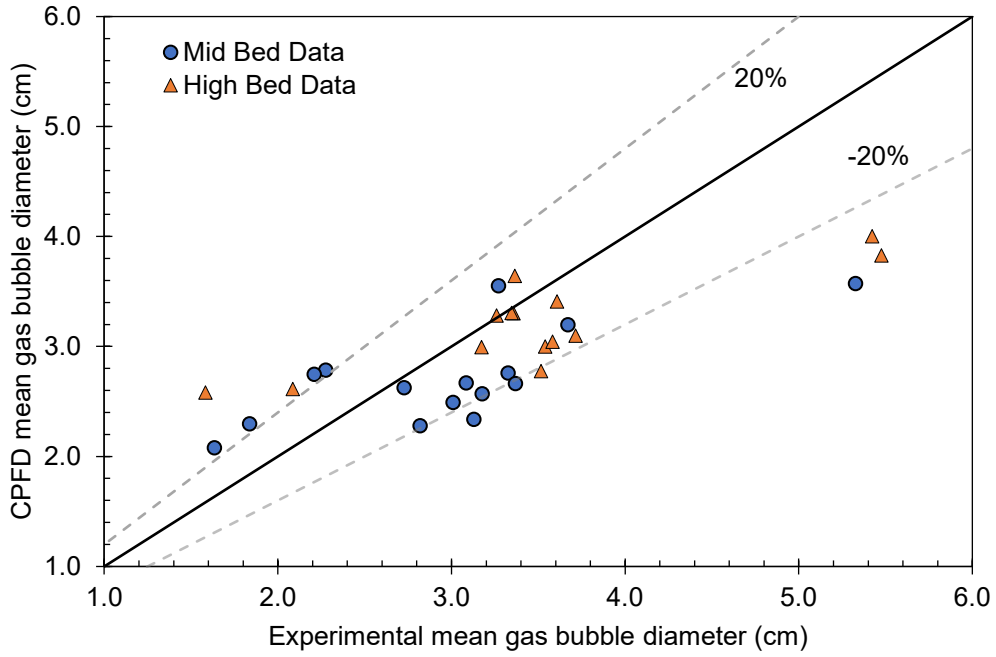

Figure 3-11. Comparison of experimentally and model derived mean bubble size. Percentages show relative deviation with 45° line.

3.4.3.3 Gas bubble growth

The bubble size growth throughout the fluidized bed was evaluated at low heights using the validated model results thereby overcoming a limitation of the experimental set up [48]. This bubble growth was then compared to the Mori & Wen [57] correlation for bubble size growth (Eq 3-17) to determine the applicability of the correlation to the simulated operating conditions. Note, the correlation requires an estimate of the initial bubble diameter (D_{b0}) and the bubble diameter approached if unrestrained coalescence were to occur in a sufficiently tall column, noted here as the maximum bubble diameter (D_{bM}) which are given by Eq 3-18 and Eq 3-19 respectively [57,58]. Figure 3-12 compares the model derived

mean bubble diameter and the Mori & Wen [57] correlation predictions along the height of the column at three pressures.

$$\frac{D_{bM} - \overline{D_b}}{D_{bM} - D_{b0}} = \exp\left(-\frac{0.3H}{D_c}\right) \quad [3\text{-}17]$$

$$D_{b0} = 1.38\left(\frac{A_c(U - U_{mf})}{Ng^{0.5}}\right)^{0.4} \quad [3\text{-}18]$$

$$D_{bM} = 2.59\left(\frac{A_c(U - U_{mf})}{g^{0.5}}\right)^{0.4} \quad [3\text{-}19]$$

The Mori & Wen [57] correlation correctly predicts the low impact of pressure, but overestimates the bubble size throughout the height of the fluidized bed. The overestimate can be attributed to the initial and maximum bubble diameter estimates. A modified Mori & Wen (Modified M&W) correlation was derived by altering the empirical proportionality coefficients present in Eq 3-18 and 3-19. By minimizing the sum of squares of the error between Eq. 18 and the initial bubble diameters predicted by the CPFD model (from z = 0 to 2 cm), a new coefficient of 0.71 was determined. Similarly, the coefficient in Eq 3-19 is changed by minimizing the sum of the square of the errors between the bubble diameter correlation and the CPFD data, resulting in a new coefficient of 1.62. The modified M&W correlation is presented in Figure 3-12 along side the model bubble diameter data at three pressures.

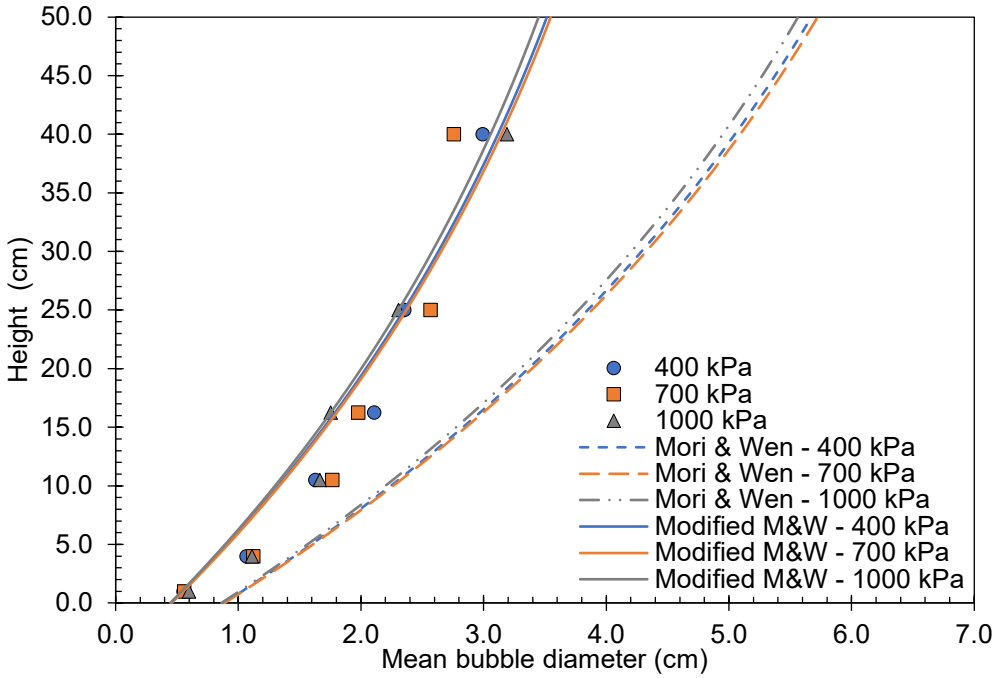

Figure 3-12. Comparison of the CPFD mean bubble size and Mori & Wen predicted bubble diameter along the fluidized bed height for the 95 µm particles at $2U_{mf}$.

When compared to the full gas bubble data set, the Mori & Wen correlation resulted in an AARD of 73%, while the Modified M&W aligned better with an AARD of 22%. It is important to note that the growth factor of 0.3 was not changed, implying the accuracy of the Mori & Wen correlation lies with the supporting correlations for initial and maximum bubble diameters.

3.5 Conclusions

Experimental data from a high-pressure cylindrical bubbling fluidized bed was compared to a computational model using the multiphase particle-in-cell approach in Barracuda Virtual Reactor® v17.4.1. The accuracy of the model in predicting the minimum fluidization velocity of various ilmenite particle sizes (95, 107, 109, 236, and 321 µm) at various pressures (101 to 2000 kPa) was found to be dependent on the input value of the close packing factor. A parametric study found that a close pack value of 0.58 was well suited to determine the minimum fluidization velocities of all the particle size distributions at each pressure, within an AARD of 3.9%.

A study of the bed expansion found that the model was able to represent the experimental trends with increasing fluidization velocity and operating pressure. The model was also able to predict the bed expansion values within an AARD of 4.8%, but with consistent under prediction. This under prediction appeared to be dependent on particle size, with the 95 µm particle size resulting in a larger deviation but remaining below 10%.

The effects of axial location, fluidization velocity and operating pressure on the bubble size distributions reported by the model were also explored. The results showed an increase in both mean bubble diameter, and distribution broadness with increased axial elevation and fluidization velocity which followed expected trends. The effect of pressure was also found to be statistically insignificant, which aligns with the experimental findings. The mean bubble diameters deviated on average by 18.7% when the experimental values were calculated using a proportionality constant of $\sqrt{3}$.

A comparison of the Mori & Wen bubble size growth correlation was compared to the bubble size growth derived from the CPFD data. The correlation over predicted the simulated bubble diameters by an average of 73%. Reductions to the empirical constants of the supporting correlations for initial and maximum bubble diameters resulted in an improved AARD of 22% with the simulated data without modifying the growth constant. The Mori & Wen equation can therefore be used to predict the axial growth of gas bubbles, but caution must used when estimating the initial and theoretical maximum bubble diameters.

In summary, the MP-PIC method was able to describe the hydrodynamic trends of the pressurized bubbling fluidized bed well. The quantitative results of the model were found to be dependent on model input parameters, so it is recommended that MP-PIC model results be validated using experimental data to ensure accurate predictions.

Acknowledgments

This research was partially sponsored and funded by the Natural Sciences and Engineering Research Council (NSERC) of Canada. This research work was sponsored and partially funded by the Program for Energy Research and Development (PERD) of Natural Resources Canada, Government of Canada. Additional funding was provided by Hatch ltd and MITACs through the MITACs Accelerate program. The authors would like to thank Patrick Boisvert from NRCan CanmetENERGY Ottawa, and Alex Kokourine from Hatch, ltd for sharing their advice and expertise in CFD and CPFD modeling towards this work. The authors would also like to thank the staff at CPFD Software for their continued help in using Barracuda Virtual Reactor.

References

[1] T. Mendiara, R. Pérez, A. Abad, L.F. De Diego, F. García-Labiano, P. Gayán, J. Adánez, Low-cost Fe-based oxygen carrier materials for the iG-CLC process with coal. 1, Ind. Eng. Chem. Res. 51 (2012) 16216–16229. https://doi.org/10.1021/ie302157y.

[2] T. Mattisson, M. Keller, C. Linderholm, P. Moldenhauer, M. Rydén, H. Leion, A. Lyngfelt, Chemical-looping technologies using circulating fluidized bed systems: Status of development, Fuel Process. Technol. 172 (2018) 1–12. https://doi.org/10.1016/j.fuproc.2017.11.016.

[3] A. Lyngfelt, Chemical Looping Combustion: Status and Development Challenges, Energy & Fuels. 34 (2020) 9077–9093. https://doi.org/10.1021/acs.energyfuels.0c01454.

[4] G.L. Schwebel, D. Filippou, G. Hudon, M. Tworkowski, A. Gipperich, W. Krumm, Experimental

comparison of two different ilmenites in fluidized bed and fixed bed chemical-looping combustion, Appl. Energy. 113 (2014) 1902–1908. https://doi.org/10.1016/j.apenergy.2013.07.042.

[5] F.N. Ridha, M.A. Duchesne, X. Lu, D.Y. Lu, D. Filippou, R.W. Hughes, Characterization of an ilmenite ore for pressurized chemical looping combustion, Appl. Energy. 163 (2016) 323–333. https://doi.org/10.1016/j.apenergy.2015.10.070.

[6] F. Mayer, A.R. Bidwe, A. Schopf, K. Taheri, M. Zieba, G. Scheffknecht, Comparison of a new micaceous iron oxide and ilmenite as oxygen carrier for Chemical looping combustion with respect to syngas conversion, Appl. Energy. 113 (2014) 1863–1868. https://doi.org/10.1016/j.apenergy.2013.04.056.

[7] H. Leion, A. Lyngfelt, M. Johansson, E. Jerndal, T. Mattisson, The use of ilmenite as an oxygen carrier in chemical-looping combustion, Chem. Eng. Res. Des. 86 (2008) 1017–1026. https://doi.org/10.1016/j.cherd.2008.03.019.

[8] A. Cuadrat, A. Abad, J. Adánez, L.F. De Diego, F. García-Labiano, P. Gayán, Behavior of ilmenite as oxygen carrier in chemical-looping combustion, Fuel Process. Technol. 94 (2012) 101–112. https://doi.org/10.1016/j.fuproc.2011.10.020.

[9] N. Berguerand, A. Lyngfelt, Design and operation of a 10 kWth chemical-looping combustor for solid fuels - Testing with South African coal, Fuel. 87 (2008) 2713–2726. https://doi.org/10.1016/j.fuel.2008.03.008.

[10] S. Rana, Z. Sun, P. Mehrani, R. Hughes, A. Macchi, Ilmenite oxidation kinetics for pressurized chemical looping combustion of natural gas, Appl. Energy. 238 (2019) 747–759. https://doi.org/10.1016/j.apenergy.2019.01.126.

[11] Y. Tan, F.N. Ridha, M.A. Duchesne, D.Y. Lu, R.W. Hughes, Reduction Kinetics of Ilmenite Ore as an Oxygen Carrier for Pressurized Chemical Looping Combustion of Methane, Energy and Fuels. 31 (2017) 7598–7605. https://doi.org/10.1021/acs.energyfuels.7b01038.

[12] Y. Tan, F.N. Ridha, D.Y. Lu, R.W. Hughes, Reduction Kinetics of Ilmenite Ore for Pressurized Chemical Looping Combustion of Simulated Natural Gas, Energy and Fuels. 31 (2017) 14201–14210. https://doi.org/10.1021/acs.energyfuels.7b02648.

[13] A. Cabello, R.W. Hughes, R.T. Symonds, S. Champagne, D.Y. Lu, E. Mostafavi, N. Manihpey, Economic Analysis of Pressurized Chemical Looping Combustion for SAGD Application, in: 5th Int. Conf. Chem. Looping, Park City, Utah, USA, 2018.

[14] R.T. Symonds, R.W. Hughes, D.Y. Lu, P. Navarri, O. Ashrafi, Systems analysis of pressurized chemical looping combustion for SAGD applications, Int. J. Greenh. Gas Control. 73 (2018) 111–123. https://doi.org/10.1016/j.ijggc.2018.03.008.

[15] A. Anantharaman, R.A. Cocco, J.W. Chew, Evaluation of correlations for minimum fluidization velocity (Umf) in gas-solid fluidization, Powder Technol. (2018). https://doi.org/10.1016/j.powtec.2017.10.016.

[16] P. Ostermeier, A. Vandersickel, S. Gleis, H. Spliethoff, Numerical Approaches for Modeling Gas-Solid Fluidized Bed Reactors: Comparison of Models and Application to Different Technical Problems, J. Energy Resour. Technol. Trans. ASME. 141 (2019) 1–10. https://doi.org/10.1115/1.4043327.

[17] S. Vashisth, A.H. Ahmadi Motlagh, S. Tebianian, M. Salcudean, J.R. Grace, Comparison of numerical approaches to model FCC particles in gas-solid bubbling fluidized bed, Chem. Eng. Sci. 134 (2015) 269–286. https://doi.org/10.1016/j.ces.2015.05.001.

[18] P. Ostermeier, A. Vandersickel, S. Gleis, H. Spliethoff, Three dimensional multi fluid modeling of

Geldart B bubbling fluidized bed with complex inlet geometries, Powder Technol. 312 (2017) 89–102. https://doi.org/10.1016/j.powtec.2017.02.015.

[19] J. Ding, D. Gidaspow, A bubbling fluidization model using kinetic theory of granular flow, AIChE J. 36 (1990) 523–538. https://doi.org/10.1002/aic.690360404.

[20] M.J. V Goldschmidt, B.P.B. Hoomans, J. a M. Kuipers, Detailed Comparison of Euler-Lagrange and Euler-Euler models for Simulation of Dense Gas-Fluidised Beds, in: Proc. 10th Work. Two Phase Flow Predict., 2002: pp. 285–299.

[21] D.M. Snider, An Incompressible Three-Dimensional Multiphase Particle-in-Cell Model for Dense Particle Flows, J. Comput. Phys. 170 (2001) 523–549. https://doi.org/10.1006/jcph.2001.6747.

[22] D.M. Snider, P.J. O'Rourke, The Multiphase Particle In Cell (MP-PIC) Method for Dense Particle Flow, in: S. Pannala, M. Syamlal, T.J. O'Brien (Eds.), Comput. Gas-Solids Flows React. Syst. Theory, Methods, Pract., 1st ed., IGI Global, Hershey, PA, 2011. https://doi.org/10.1017/CBO9781107415324.004.

[23] M. J. Andrews and P.J. O'Rourke, The Multiphase Particle-in-Cell (MP-PIC) Method for Dense Particulate Flows, Int J Multiph. Flow. 22 (1996) 379–402.

[24] Y. Shao, J. Gu, W. Zhong, A. Yu, Determination of minimum fluidization velocity in fluidized bed at elevated pressures and temperatures using CFD simulations, Powder Technol. 350 (2019) 81–90. https://doi.org/10.1016/j.powtec.2019.03.039.

[25] S. Karimipour, T. Pugsley, Application of the particle in cell approach for the simulation of bubbling fluidized beds of Geldart A particles, Powder Technol. 220 (2012) 63–69. https://doi.org/10.1016/j.powtec.2011.09.026.

[26] W. S. Amarasinghe, C. K. Jayarathna, B. S. Ahangama, B. M. E. Moldestad, L.-A. Tokheim, Experimental Study and CFD Modelling of Minimum Fluidization Velocity for Geldart A, B and D Particles, Int. J. Model. Optim. 7 (2017) 152–156. https://doi.org/10.7763/ijmo.2017.v7.575.

[27] C. Jayarathna, B. Moldestad, L.-A. Tokheima, Validation of results from Barracuda CFD modelling to predict the minimum fluidization velocity and the pressure drop of Geldart A particles, Proc. 58th Conf. Simul. Model. (SIMS 58) Reykjavik, Iceland, Sept. 25th – 27th, 2017. 138 (2017) 76–82. https://doi.org/10.3384/ecp1713876.

[28] C.B. Solnordal, V. Kenche, T.D. Hadley, Y. Feng, P.J. Witt, K.S. Lim, Simulation of an internally circulating fluidized bed using a multiphase particle-in-cell method, Powder Technol. 274 (2015) 123–134. https://doi.org/10.1016/j.powtec.2014.12.045.

[29] F. Fotovat, A. Abbasi, R.J. Spiteri, H. de Lasa, J. Chaouki, A CPFD model for a bubbly biomass-sand fluidized bed, Powder Technol. 275 (2015) 39–50. https://doi.org/10.1016/j.powtec.2015.01.005.

[30] Y. Zhang, Q. Wei, CPFD simulation of bed-to-wall heat transfer in a gas-solids bubbling fluidized bed with an immersed vertical tube, Chem. Eng. Process. - Process Intensif. 116 (2017) 17–28. https://doi.org/10.1016/j.cep.2017.03.007.

[31] J.M. Weber, K.J. Layfield, D.T. Van Essendelft, J.S. Mei, Fluid bed characterization using electrical capacitance volume tomography (ECVT), compared to CPFD software's barracuda, Powder Technol. 250 (2013) 138–146. https://doi.org/10.1016/j.powtec.2013.10.005.

[32] H.C. Park, H.S. Choi, Numerical study of the segregation of pyrolized char in a bubbling fluidized bed according to distributor configuration, Powder Technol. 355 (2019) 637–648. https://doi.org/10.1016/j.powtec.2019.07.084.

[33] X. Shi, X. Lan, F. Liu, Y. Zhang, J. Gao, Effect of particle size distribution on hydrodynamics and

solids back-mixing in CFB risers using CPFD simulation, Powder Technol. 266 (2014) 135–143. https://doi.org/10.1016/j.powtec.2014.06.025.

[34] X. Shi, R. Sun, X. Lan, F. Liu, Y. Zhang, J. Gao, CPFD simulation of solids residence time and back-mixing in CFB risers, Powder Technol. 271 (2015) 16–25. https://doi.org/10.1016/j.powtec.2014.11.011.

[35] Q. Wang, T. Niemi, J. Peltola, S. Kallio, H. Yang, J. Lu, L. Wei, Particle size distribution in CPFD modeling of gas-solid flows in a CFB riser, Particuology. 21 (2015) 107–117. https://doi.org/10.1016/j.partic.2014.06.009.

[36] Y. Zhang, F. Lei, S. Wang, X. Xu, Y. Xiao, A numerical study of gas-solid flow hydrodynamics in a riser under dense suspension upflow regime, Powder Technol. 280 (2015) 227–238. https://doi.org/10.1016/j.powtec.2015.04.061.

[37] M. Nakhaei, C.E. Hessel, H. Wu, D. Grévain, S. Zakrzewski, L.S. Jensen, P. Glarborg, K. Dam-Johansen, Experimental and CPFD study of gas–solid flow in a cold pilot calciner, Powder Technol. 340 (2018) 99–115. https://doi.org/10.1016/j.powtec.2018.09.008.

[38] A. Lanza, M.A. Islam, H. de Lasa, Particle clusters and drag coefficients in gas-solid downer units, Chem. Eng. J. 200–202 (2012) 439–451. https://doi.org/10.1016/j.cej.2012.06.027.

[39] Q. Wang, H. Yang, P. Wang, J. Lu, Q. Liu, H. Zhang, L. Wei, M. Zhang, Application of CPFD method in the simulation of a circulating fluidized bed with a loop seal, part I-Determination of modeling parameters, Powder Technol. 253 (2014) 814–821. https://doi.org/10.1016/j.powtec.2013.11.041.

[40] Q. Wang, H. Yang, P. Wang, J. Lu, Q. Liu, H. Zhang, L. Wei, M. Zhang, Application of CPFD method in the simulation of a circulating fluidized bed with a loop seal Part II-Investigation of solids circulation, Powder Technol. 253 (2014) 822–828. https://doi.org/10.1016/j.powtec.2013.11.040.

[41] Q. Ma, F. Lei, Y. Xiao, Numerical analysis of operating conditions for establishing high-density circulating fluidized bed by CPFD method, Powder Technol. 338 (2018) 446–457. https://doi.org/10.1016/j.powtec.2018.07.012.

[42] Q. Tu, H. Wang, CPFD study of a full-loop three-dimensional pilot-scale circulating fluidized bed based on EMMS drag model, Powder Technol. 323 (2018) 534–547. https://doi.org/10.1016/j.powtec.2017.09.045.

[43] Y. Wu, L. Peng, L. Qin, M. Wang, J. Gao, X. Lan, Validation and application of CPFD models in simulating hydrodynamics and reactions in riser reactor with Geldart A particles, Powder Technol. 323 (2018) 269–283. https://doi.org/10.1016/j.powtec.2017.10.003.

[44] J.M. Parker, CFD model for the simulation of chemical looping combustion, Powder Technol. 265 (2014) 47–53. https://doi.org/10.1016/j.powtec.2014.01.027.

[45] J. Gu, Y. Shao, X. Liu, W. Zhong, A. Yu, Modelling of particle flow in a dual circulation fluidized bed by a Eulerian-Lagrangian approach, Powder Technol. 323 (2018) 433–447. https://doi.org/10.1016/j.ces.2018.08.008.

[46] M.A. Hamilton, K.J. Whitty, J.A.S. Lighty, Numerical simulation comparison of two reactor configurations for chemical looping combustion and chemical looping with oxygen uncoupling, J. Energy Resour. Technol. Trans. ASME. 138 (2016) 1–9. https://doi.org/10.1115/1.4033108.

[47] S. Kraft, F. Kirnbauer, H. Hofbauer, CPFD simulations of an industrial-sized dual fluidized bed steam gasification system of biomass with 8 MW fuel input, Appl. Energy. 190 (2017) 408–420. https://doi.org/10.1016/j.apenergy.2016.12.113.

[48] C.J. McIntyre, R.T. Symonds, D.Y. Lu, S. Champagne, A. Macchi, P. Mehrani, Experimental

evaluation of hydrodynamics and tube-to-bed heat transfer of fluidized Ilmenite ore particles at elevated pressures, Powder Technol. 376 (2020) 697–707. https://doi.org/10.1016/j.powtec.2020.08.062.

[49] F. Li, Heat Transfer in a High-pressure Gas-solid Fluidized Bed with Horizontal Tube Bundle and Continuous Addition of Fines, (2018).

[50] S.E. Harris, D.G. Crighton, Solitons, solitary waves, and voidage disturbances in gas-fluidized beds, J. Fluid Mech. 266 (1994) 243–276. https://doi.org/10.1017/S0022112094000996.

[51] CPFD Software, Barracuda Virtual Reactor User Manual, (n.d.).

[52] J. Grace, Fluidized Bed Hydrodynamics, in: Handb. Multiph. Flow, McGraw-Hill, Washington,DC, 1982: p. 970.

[53] A.C. Hoffmann, J.G. Yates, Experimental Observations of Fluidized Beds at Elevated Pressures, Chem. Eng. Commun. 41 (1986) 133–149. https://doi.org/10.1080/00986448608911716.

[54] D.C. Chitester, R.M. Kornosky, L.S. Fan, J.P. Danko, Characteristics of fluidization at high pressure, Chem. Eng. Sci. (1984). https://doi.org/10.1016/0009-2509(84)80025-1.

[55] M. Liu, Y. Zhang, H. Bi, J.R. Grace, Y. Zhu, Non-intrusive determination of bubble size in a gas-solid fluidized bed: An evaluation, Chem. Eng. Sci. 65 (2010) 3485–3493. https://doi.org/10.1016/j.ces.2010.02.049.

[56] M. Rüdisüli, T.J. Schildhauer, S.M.A. Biollaz, A. Wokaun, J. Ruud van Ommen, Comparison of bubble growth obtained from pressure fluctuation measurements to optical probing and literature correlations, Chem. Eng. Sci. 74 (2012) 266–275. https://doi.org/10.1016/j.ces.2012.01.045.

[57] S. Mori, C.Y. Wen, Estimation of bubble diameter in gaseous fluidized beds, AIChE J. 21 (1975) 109–115. https://doi.org/10.1002/aic.690210114.

[58] J.R. Grace, R. Di Felice, A. Di Renzo, X. Bi, N. Ellis, T. Li, Y. Xu, F. Fotovat, T.M. Knowlton, S. Reddy Karri, C. Wang, J. Zhu, P. Mehrani, A. Sowinski, D.E. Jia, A. Machecha-Botero, J. Shabanian, J. Chaouki, Y. Zhang, C. Briend, J. McMillan, C. Wu, Y. Cheng, N. Epstien, D. Pjontek, A. Donaldson, A. Macchi, Essentials of Fluidization Technology, 1st ed., Wiley-VCH, Weinheim, Germanu, 2020. https://doi.org/10.1002/9783527699483.

Chapter 4 CPFD modeling of a novel internally circulating fluidized bed for chemical looping combustion

C. J. McIntyre[a], A. Kokourine[b], R.W. Hughes[c], A. Macchi[a*], P. Mehrani[a*]

[a] Department of Chemical and Biological Engineering, University of Ottawa, 161 Louis Pasteur Street, Ottawa, ON, Canada, K1N 6N5

[b]Hatch, Ltd., 2800 Speakman Drive, Mississauga, ON, Canada, L5K 2R7

[c] Natural Resources Canada, CanmetENERGY, 1 Haanel Drive, Ottawa, ON, Canada, K1A 1M1

[*]*Corresponding authors email.* Arturo Macchi arturo.macchi@uottawa.ca*;* Poupak Mehrani: poupak.mehrani@uottawa.ca

Chapter 4 is a manuscript to be submitted for journal publication

Abstract

A novel reactor design is proposed for chemical looping combustion. The Plug Flow Internally-circulating Reactor (PFIR) consists of an annular fluidized bed region operating in the bubbling regime. The reactor is separated into two different sections by baffles with underflow slots to allow for solids passage. The solids are circulated around the reactor with angled fluid jets. A CPFD (Computational Particle Fluid Dynamics) model of the PFIR was created using the multiphase particle-in-cell method to investigate the effects of superficial gas velocity, jet velocity, and bed mass on solids circulation rate and gas infiltration rate between sections. The circulation rate of solids was found to be dependent on the rate of horizontal fluid momentum entering, requiring a minimum rate of fluid momentum before circulation begins. A regression allowed for a method of predicting the required rate of momentum input for a desired circulation rate. The gas infiltration was found to be correlated to the solids circulation rate, with more gas passing through to adjacent zones with higher solids circulation due to the gas trapped in the emulsion phase. A regression of the data allowed for a method to predict the gas infiltration rate for a desired solids circulation rate.

Keywords: Plug Flow Internally-circulating Reactor, Solids Circulation, Gas Infiltration Chemical Looping Combustion, Computational Particle Fluid Dynamics

Nomenclature

Variables	
$\boldsymbol{A}$	Discrete particle acceleration (m/s^2)
A_c	Cross sectional area (m^2)
C_d	Drag Coefficient (-)
D	Drag Function (s^{-1})
D_1	Wen-Yu Drag Function (s^{-1})
D_2	Ergun Drag Function (s^{-1})
ΔP	Pressure differential (kPa)
$\boldsymbol{F}$	Interphase rate of momentum transfer (N)
f	Particle distribution function (-)
$\boldsymbol{g}$	Acceleration due to gravity (m/s^2)
H	Bed height (m)
m	Mass (kg)
$\dot{m}$	Mass flow rate (kg/s)
M_b	Bed mass (kg)
MW	Molar weight (g/gmol)
P	Pressure (Pa)
$\dot{p}_{in}$	Fluid momentum rate entering (kg m/s^2)
P_s	Solids Pressure term (Eq 4-7) (Pa)
R	Universal gas constant (8.314 J/mol K)
Re	Reynolds Number $= \frac{2\rho_f r_s \lvert \boldsymbol{u_f} - \boldsymbol{u_s} \rvert}{\mu_f}$ (-)
r_s	Particle radius (m)
T	Temperature (K)
t	Time (s)
U	Superficial gas velocity (m/s)
$\boldsymbol{u}$	Velocity (m/s)
V_j	Tuyere jet velocity (m/s)
$\boldsymbol{x}$	Position (m)
Greek Letters	
β	Solids stress function term (Eq 4-7) (-)
ε	Solids stress function term (Eq 4-7) (-)
μ	Viscosity (Pa s)
ρ	Density (kg/m^3)
$\boldsymbol{\tau}$	Stress tensor (Pa)
θ	Volume fraction (-)
Subscripts	
f	Fluid phase
mf	Minimum fluidization
s	Solid phase

Acronyms	
AARD	Average Absolute Relative Deviation $= \frac{1}{n}\sum \frac{\lvert x_{experimental} - x_{predicted} \rvert}{x_{experimental}} \times 100\%$
AR	Air Reactor
CCUS	Carbon Capture, Utilization, and Sequestration
CFD	Computational Fluid Dynamics
CLC/R	Chemical Looping Combustion / Reforming
CPFD	Computation Particle Fluid Dynamics
FR	Fuel Reactor
ICFB	Interconnected Circulating Fluidized Bed
KTGF	Kinetic Theory of Granular Flow
MP-PIC	Multiphase Particle-in-Cell
OC	Oxygen Carrier
PFIR	Plug Flow Internally-circulating Reactor
TFM	Two Fluid Model

Note: vector quantities are bolded

4.1 Introduction

Chemical looping combustion (CLC) and chemical looping reforming (CLR) are two promising next generation carbon capture, utilization, and sequestration (CCUS) technologies to produce heat, steam, and hydrogen [1–3]. Similar to oxy-fuel combustion, CLC operates by reacting hydrocarbon fuels with high purity oxygen to prevent the dilution of flue gases with nitrogen. Instead of using an air separation unit however, CLC implements a metal oxide, known as an oxygen carrier (OC), to provide inherent oxygen separation [3]. The OC is looped between an air reactor (AR) and fuel reactor (FR) where it undergoes cyclic oxidation and reduction reactions. In the AR, the OC is oxidized by incoming air before it is transferred to the FR where it undergoes a reduction reaction with the fuel. Ilmenite has favourable thermodynamic properties and high reactivity with syngas [4–6] making it a promising candidate for an OC, but it exhibits relatively low reactivity with methane at atmospheric conditions [7–9]. High pressure operation can compensate for the low reactivity by increasing the partial pressure of methane. Increased operating pressures have additional technical and economic benefits to the overall process [10,11].

There are several considerations when selecting a CLC reactor design [12]. The reactors must (1) provide sufficiently high solids circulation rate to achieve the required thermal energy transfer and stoichiometric ratios between the air and fuel reactors; (2) maintain sufficient gas separation; (3) provide sufficient residence time to reach the desired conversions; and (4) withstand temperatures and pressures required for application. Several design concepts have been explored for CLC [13,14], including interconnected circulating fluidized beds (ICFBs) [11,15–22] (Figure 4-1A), fixed bed gas switching (Figure 4-1B) [4,23–26] and rotating fixed beds (Figure 4-1C) [27,28].

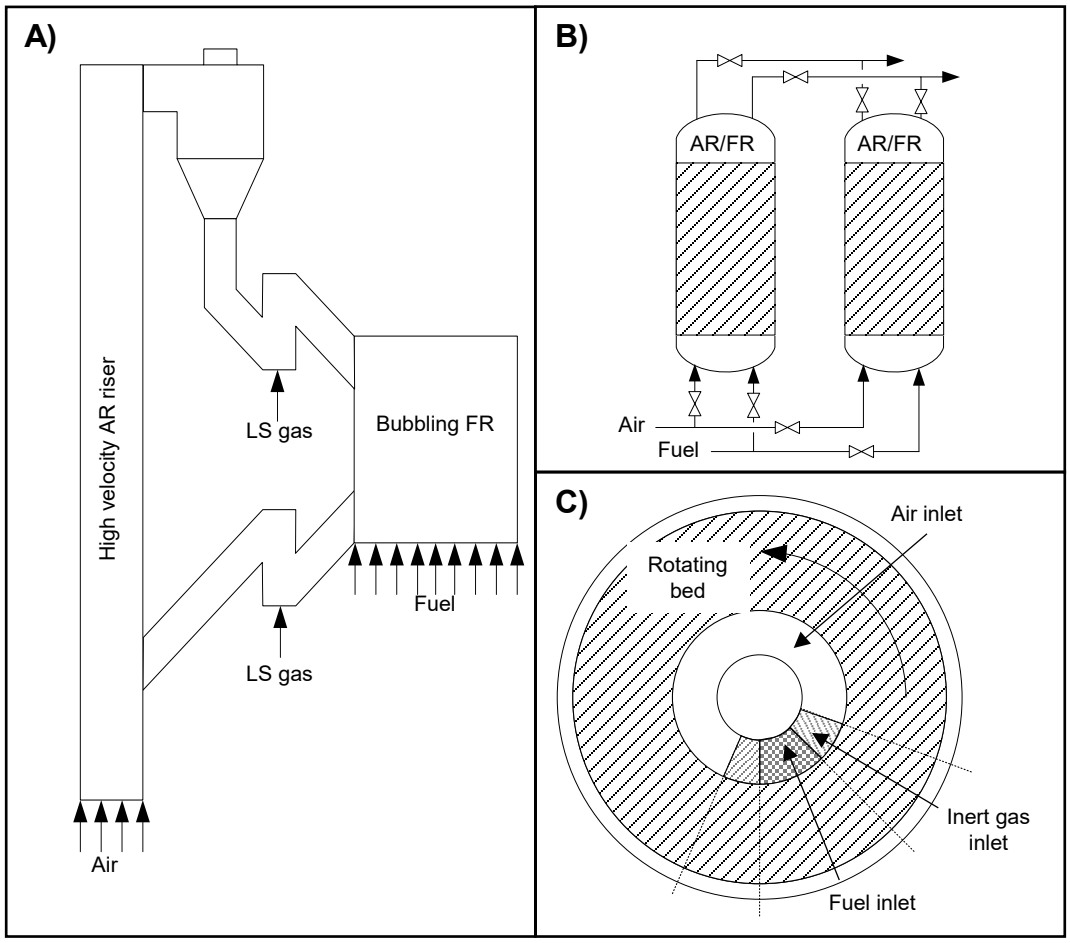

Figure 4-1. Schematics for different reactor concepts implemented for CLC. A) interconnected circulating fluidized bed B) fixed bed with gas switching and C) rotating bed.

ICFBs are the most commonly studied and implemented reactor designs in the CLC community [3,13]. They typically consist of a high velocity riser as the AR and a moving or bubbling fluidized bed for the FR [15–18,22,29,30]. Loop seals are employed to prevent gas infiltration between reactors and facilitate solids transfer, while cyclones are used to separate the gas and solids. ICFBs take advantage of high rates of gas-solid mixing, and can achieve high circulation rates [31]. However, they have several disadvantages when operating at increased pressures such as high capital costs to outfit the different sections (cyclones, loop-seals) with their respective pressure vessels, and increased fluidization gas in the loop seals which decreases the overall efficiency of the CLC process [32].

Fixed bed reactors consist of two or more separate reactors containing fixed beds of OC operating in parallel to maintain near-continuous operation [23,24]. Instead of solids transfer between distinct air and fuel reactor vessels, the nature of a vessel is changed based on the inlet gas. Air and fuel are switched between the

different vessels to complete the oxidation and reduction steps of the OC. This reactor scheme inherently avoids steps for gas-solids separation and allows for easier high-pressure operation [12,33]. However, the fixed bed risks particle sintering due to the required high temperatures for operation and lower heat transfer rates relative to fluidized beds [4]. Furthermore, gas switching at large scale would involve a complicated system of valves, and the pulsed operation could be problematic for downstream operations [12].

Rotating reactors use a fixed bed of particles that is rotated around an annular vessel [27,28]. The gases are vertically distributed along the inner wall and radially propagate outwards through the rotating bed with inert gases introduced between the air and fuel injections to mitigate gas mixing. This reactor scheme has only been demonstrated at lab scale, and exhibited low carbon dioxide purities on the order of 20-65% due to significant nitrogen slippage [28].

This work explores a new type of reactor geometry called the Plug Flow Internally-circulating Reactor (PFIR) [34,35]. The PFIR (Figure 4-2) consists of an annular region in which particles are fluidized and circulated between two distinct sections separated by baffles. The baffles have an opening at the bottom of the reactor vessel to allow for solids to pass between the reactor sections, while aiding in separation of the gases. Fluidization gas is introduced through angled tuyeres located at the bottom of the vessel, which also induces the rotation of the particle bed. The PFIR operates in the bubbling fluidized bed regime, thereby taking advantage of the excellent gas-solids mixing of fluidized beds. Furthermore, issues resulting from external solids circulation are eliminated since all circulation occurs internally and with no mechanical parts, which can reduce operational downtime. Lastly, the PFIR offers the advantage of reduced capital and construction costs, and a smaller footprint since it consists of only one vessel. Specifically, this study investigates the effects of superficial gas velocity, tuyere jet velocity, bed mass, and operating pressure on the solids circulation rate and gas infiltration rate between sections under cold flow conditions to gain an initial understanding of how the PFIR operates.

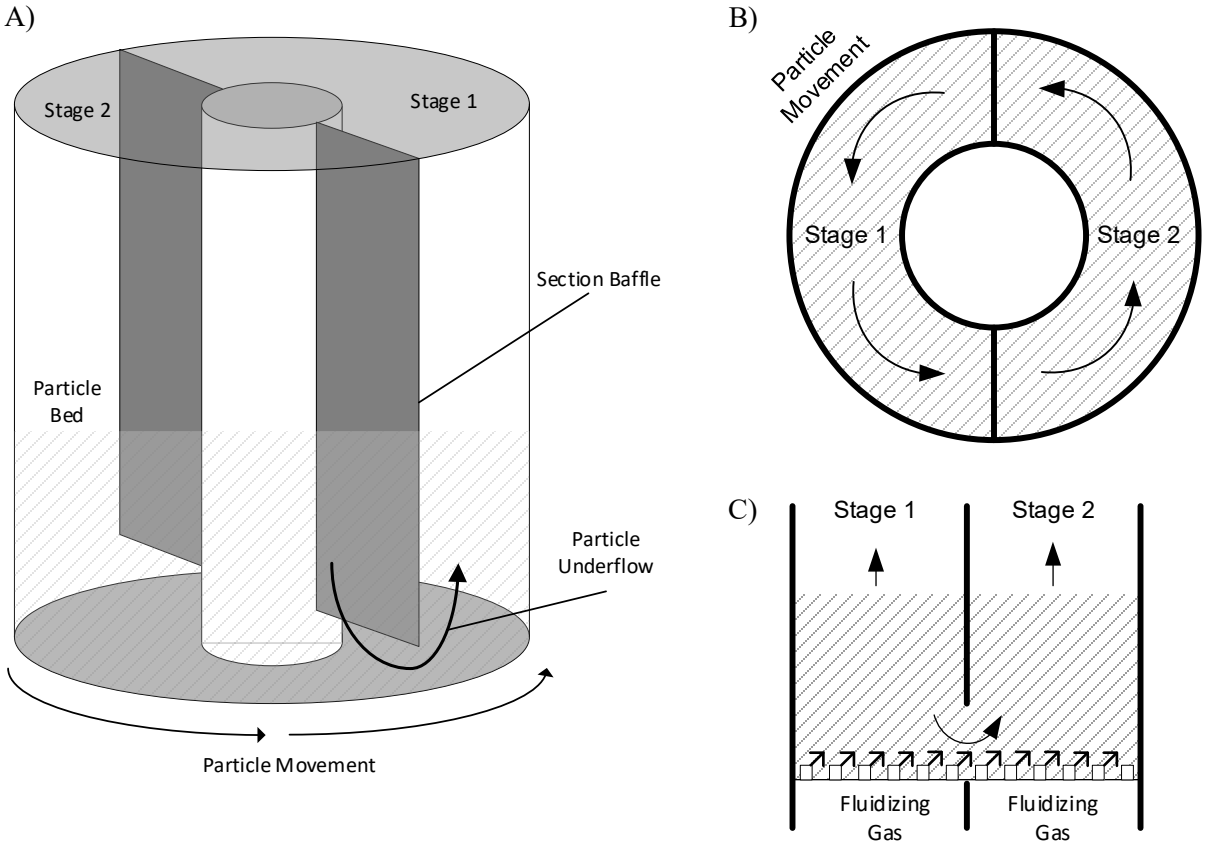

Figure 4-2. Schematic of PFIR geometry. A) 3-dimensional view B) Top-down view C) Side view of stage transition

The investigation is completed using the Multi-Phase Particle-in-Cell (MP-PIC) approach implemented in the commercial software Barracuda Virtual Reactor® v20.01. The MP-PIC approach, also known as the Computational Particle Fluid Dynamic (CPFD) approach, has been shown to be a computationally efficient and accurate method of exploring fluidized bed geometries, including bubbling fluidized beds [36–44], internally circulation fluidized beds [45], fluidized bed risers [46–50] and downcomers [51], full circulating fluidized beds [22,52–56], and interconnected circulating fluidized beds [57–60]. The MP-PIC approach follows an Eulerian-Lagrangian framework in that it models the fluid phase as a continuous entity and models the particulate phase using discrete entities called computational particles or parcels. Computational parcels are groupings of particles with similar position, mass, velocity, etc. This mathematical treatment of fluidized bed systems significantly lowers the computational demand of Eulerian-Lagrangian methods [61–63]. To reduce computational demand, the method calculates select particle properties in an Eulerian framework that are computationally difficult to calculate for the individual parcels and uses interpolation operators to map these properties to the discrete entities. Thus, the MP-PIC approach can model large

fluidized bed systems, such as commercial reactors, efficiently without excessively sacrificing the particle phase resolution.

4.2 Model description

4.2.1 Multiphase particle-in-cell method governing equations

The volume-averaged Navier-Stokes equations are used to model the fluid phase as a continuum on an Eulerian grid (Eq 4-1 & 4-2) [61–63]. The interphase rate of momentum transfer, $\boldsymbol{F}$, is calculated using Eq 4-3.

$$\frac{\partial(\theta_f \rho_f)}{\partial t} + \boldsymbol{\nabla} \cdot \left(\theta_f \rho_f \boldsymbol{u_f}\right) = 0 \quad [4\text{-}1]$$

$$\frac{\partial(\theta_f \rho_f \boldsymbol{u_f})}{\partial t} + \boldsymbol{\nabla} \cdot \left(\theta_f \rho_f \boldsymbol{u_f} \boldsymbol{u_f}\right) = -\boldsymbol{\nabla} p - \boldsymbol{F} + \theta_f \rho_f \boldsymbol{g} + \boldsymbol{\nabla} \cdot (\theta_f \boldsymbol{\tau_f}) \quad [4\text{-}2]$$

$$\boldsymbol{F} = \iint f m_s \left[D_s\left(\boldsymbol{u_f} - \boldsymbol{u_s}\right) - \frac{1}{\rho_s} \boldsymbol{\nabla} p \right] dm_s d\boldsymbol{u_s} \quad [4\text{-}3]$$

A particle distribution function is used to model the solid phase (Eq 4-4). A Liouville equation (Eq 4-5) is obtained when the time rate of change of Eq 4-4 is taken, which can be interpreted as the conservation of particle numbers as they move along their trajectories in the particle phase space. Eq 4-5 assumes there is no direct particle-particle collisions or particle breakup.

$$f(\boldsymbol{x}, m_s, \boldsymbol{u_s}, t) dm_s d\boldsymbol{u_s} \quad [4\text{-}4]$$

$$\frac{\partial f}{\partial t} + \boldsymbol{\nabla_x} \cdot (f \boldsymbol{u_s}) + \boldsymbol{\nabla_{u_s}} \cdot (f \boldsymbol{A}) = 0 \quad [4\text{-}5]$$

Eq 4-6 describes the particle acceleration, $\boldsymbol{A}$, due to aerodynamic drag, buoyancy, gravity, and interparticle normal stresses. The full particle size distribution is inherently modeled by the coupling of the phases through the drag term, and since the full particle distribution (Eq 4-4) is solved at each time step.

$$\boldsymbol{A} = D_s\left(\boldsymbol{u_f} - \boldsymbol{u_s}\right) - \frac{1}{\rho_s} \boldsymbol{\nabla} P + \boldsymbol{g} - \frac{1}{\theta_s \rho_s} \boldsymbol{\nabla} \tau_s \quad [4\text{-}6]$$

Interparticle collisions are not directly modeled, but instead the collective stresses of neighbouring particles are calculated and applied to individual particles. This collective effect is determined by the normal particle

stress tensor (Eq 4-7), which is a modified version of the Harris & Crighton [64] particle stress function to avoid the singularity when the particle volume fraction equals the close pack value, θ_{CP}. The close pack value is the maximum volume fraction of particles that can occupy a computational cell.

$$\tau_s = \frac{P_s \theta_s^{\beta}}{\max[\theta_{CP} - \theta_s, \varepsilon(1 - \theta_s)]} \quad [4\text{-}7]$$

4.2.2 Drag model

The drag model used in this work is the blended Wen-Yu/Ergun drag model (Eq 4-8) which has been extensively validated for bubbling fluidized beds over a wide range of operating conditions [36–39,41,45]. The particle drag is determined by using the local solids volume fraction to calculate a weighted average of the Wen-Yu (Eq 4-9 & 4-10) and Ergun drag equations (Eq 4-11). The Wen-Yu model is better suited to dilute particle regions and the Ergun drag is better suited to dense particle regions, as such, the blended Wen-Yu/Ergun drag law is well suited to modeling the different levels of particle drag in the dilute and dense regions of a bubbling fluidized bed.

$$D = \begin{cases} D_1 & \theta_s < 0.75\theta_{CP} \\ (D_2 - D_1)\dfrac{(\theta_s - 0.75\theta_{CP})}{0.85\theta_{CP} - 0.75\theta_{CP}} + D_1 & 0.75\theta_{CP} \le \theta_s \le 0.85\theta_{CP} \\ D_2 & \theta_s > 0.85\theta_{CP} \end{cases} \quad [4\text{-}8]$$

$$D_1 = \frac{3}{8}\frac{C_d \rho_f |\boldsymbol{u_f} - \boldsymbol{u_s}|}{\rho_s r_s} \quad [4\text{-}9]$$

$$C_d = \begin{cases} \dfrac{24}{Re}\theta_f^{-2.65} & Re < 0.5 \\ \dfrac{24}{Re}\theta_f^{-2.65}(1.0 + 0.15Re^{0.687}) & 0.5 \le Re \le 1000 \\ 0.44\theta_f^{-2.65} & Re > 1000 \end{cases} \quad [4\text{-}10]$$

$$D_2 = 0.5\frac{\left(\dfrac{180\theta_s}{\theta_f Re} + 2\right)\left(\rho_f |\boldsymbol{u_f} - \boldsymbol{u_s}|\right)}{\rho_s r_s} \quad [4\text{-}11]$$

4.2.3 Model geometry and boundary conditions

The modeled PFIR geometry (Figure 4-3) has an inner diameter of 0.115 m, and an outer diameter of 0.571 m, creating an annular region of 0.228 m in width where fluidization occurs. Fluidizing gas is introduced through uniformly distributed injection points (triangular pattern) at the bottom of the 3.6 m tall column to

emulate a tuyere plate. The tuyere jets are angled at 25° above the horizontal to induce circulation. Baffles are located 60° apart from each other to separate the two zones of the reactor. There is a 0.1 m high opening at the bottom of the baffle which spans the width of the annulus to allow for solids circulation between zones.

The model had three pressure boundary conditions located at the top of the column – two in the larger section and one in the smaller section. All three were set to the desired operating pressure. The particles used in the model are alumina zirconia with a Sauter mean diameter of 236 µm, modeled as a particle size distribution with a d_{10}, d_{50}, and d_{90} of 212 µm, 250 µm, and 300 µm respectively. The particle bed mass, fluidizing gas mass flow rate, and fluid injection jet velocity were all input for a given case. Five superficial gas velocities between 2.1 and 4.9 U_{mf}, three jet velocities of 60, 80, and 100 m/s, seven bed masses from 58 to 1460 kg, and seven operating pressures from 101 kPa to 1200 kPa were modeled. It should be noted that the jet velocity and fluidizing gas mass flow rate were controlled independently in the model which can be physically interpreted as changing the orifice diameter of the tuyere to change the jet velocity. The model operated isothermally at 300 K for all cases.

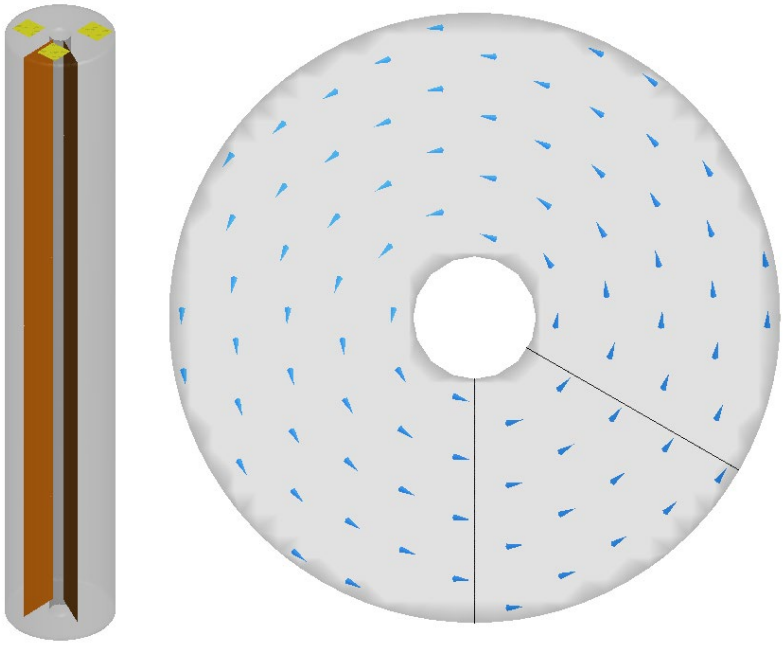

Figure 4-3. Simulated PFIR geometry.

Other relevant simulation parameters are presented in Table 4-1. The model parameters were taken from previous work in which the MP-PIC method was validated for bubbling fluidized beds implementing high density and relatively small particles (ilmenite) [65]. The alumina zirconia particles used in this work have

a similar density ($\rho_p = 4300\ kg/m^3$) to ilmenite ($\rho_p = 4700\ kg/m^3$) and the PFIR model implemented an identical particle size distribution as the validated model, thus giving confidence in these model parameters to provide reasonably accurate results.

Table 4-1. Model parameters used in this work.

Parameter Name	**Value**
Gravity, m/s^2	9.81
Close pack value	0.58
Maximum momentum redirection from collision	40%
Normal-to-wall momentum retention	0.85
Tangent-to-wall momentum retention	0.85
Diffuse Bounce	0
P_s (Eq. 7), Pa	10
β (Eq. 7)	3
ε (Eq. 7)	1e-08
Turbulence model	Large Eddy Simulation

Data for solids circulation rate was collected using measurement planes along at four locations (negative X, negative Y, positive X, and positive Y axes) while data for gas infiltration was collected at the entrance of the fuel reactor (corresponding to the negative Y axis). More information about the data collection is presented in Appendix C. Figure 4-4 depicts the raw data for net particle mass crossing the measurement plane with time. The particle circulation rate was determined by averaging the absolute values of the slopes of each line. It should be noted that the sign of the slope corresponds to the direction of travel – positive slopes indicate the particles are travelling in the positive coordinate direction, and negative slopes indicate the opposite. Steady state is achieved after approximately 5 seconds of simulation time, however a 20 second window was used to be conservative. The slopes were therefore calculated using the last 80 seconds of data. The method of data analysis is identical for determining the gas infiltration rate.

It should be noted that the noise in the raw data is due to gas bubbles travelling back and forth through the measurement planes. The impact of gas bubbles is evident by the lower levels of noise in the negative Y axis line, which corresponds to the fuel reactor entrance and therefore a smaller area of measurement.

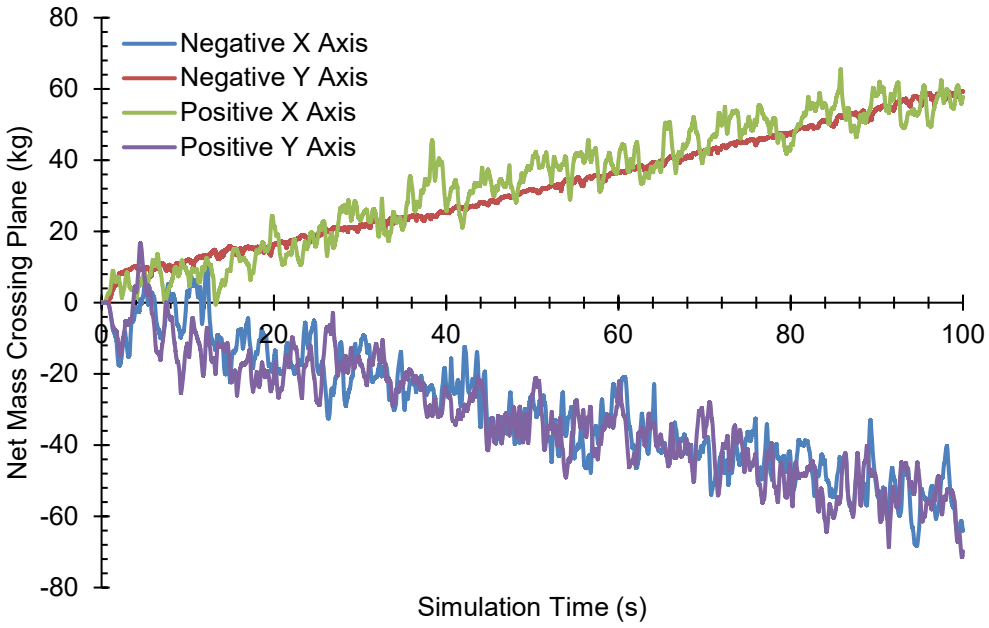

Figure 4-4. Raw data produced by CPFD simulation for particle circulation rate

4.2.4 Mesh Study

A study of the mesh influence was performed to determine the optimal mesh resolution without affecting the results. Three mesh resolutions were explored: 49,731 cells (coarse), 114,392 cells (medium) and 153,827 cells (fine). The circulation rate and the gas infiltration rate were calculated for the same set of operating conditions ($U = 2.0\ U_{mf}$, $V_j = 80$ m/s, $M_b = 1070$ kg, $P = 101$ kPa) for the three mesh resolutions. The circulation rate changes by 38.4% between the coarse and medium resolution, and 5.4% between the medium and fine resolutions. Similarly, the gas infiltration rate changes by 53.3% between the coarse and medium resolutions, and by 4.3% between the medium and fine resolutions. The medium mesh resolution was thus selected to ensure grid independent solution.

4.3 Results and discussion

4.3.1 Circulation Rate

The influence of superficial gas velocity, jet velocity, bed mass, and pressure on solids circulation rate are shown in Figure 4-5, Figure 4-6, and Figure 4-7. It should be noted, for the pressurized conditions, a constant U/U_{mf} of 3.5 was maintained at the bottom of the bed to allow for comparison between pressurized conditions. As the superficial gas velocity is increased, the circulation rate also increased (Figure 4-5). The nature of the increase is influenced by the jet velocity, with the lower jet velocity of 60 m/s resulting in a

non-linear increase in circulation rate, and the two higher jet velocities behaving in a more linear fashion. The influence of increasing jet velocity on particle circulation at any given superficial gas velocity is linear. The influence of bed mass (Figure 4-6) also results in a linear increase in circulation rate for the two lower superficial gas velocities. At the higher superficial gas velocity, bed masses above 273 kg result in a similar linear trend, but the circulation rate significantly decreases at the lowest bed mass. Similarly, circulation rate exhibits an increase with increasing pressure (Figure 4-7).

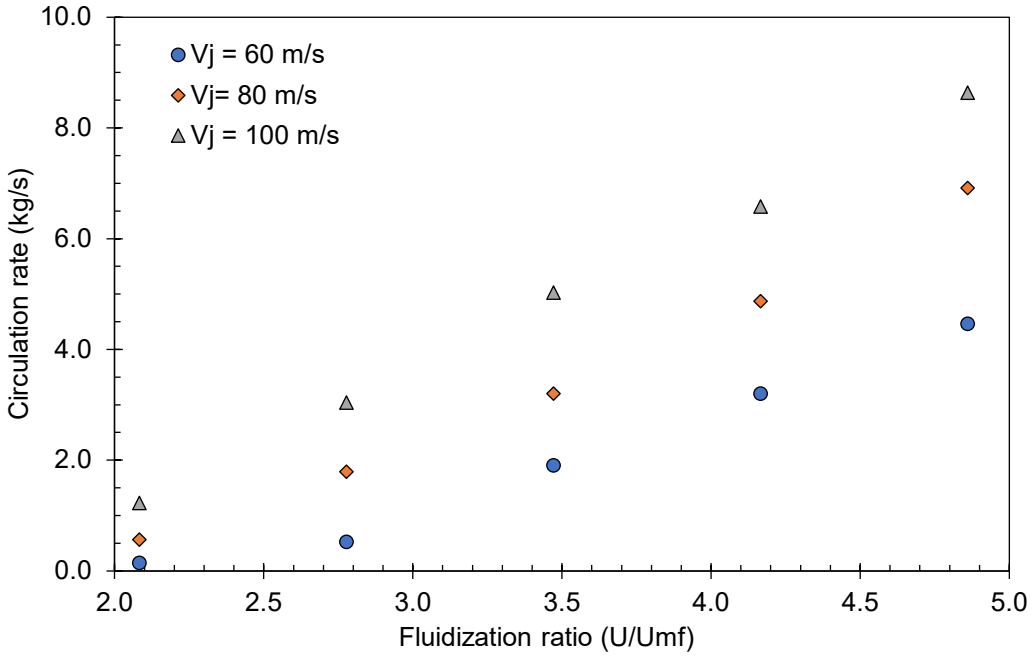

Figure 4-5. Solids circulation rate at varying superficial gas velocity and jet velocities. (M_b = 933 kg, P = 101 kPa).

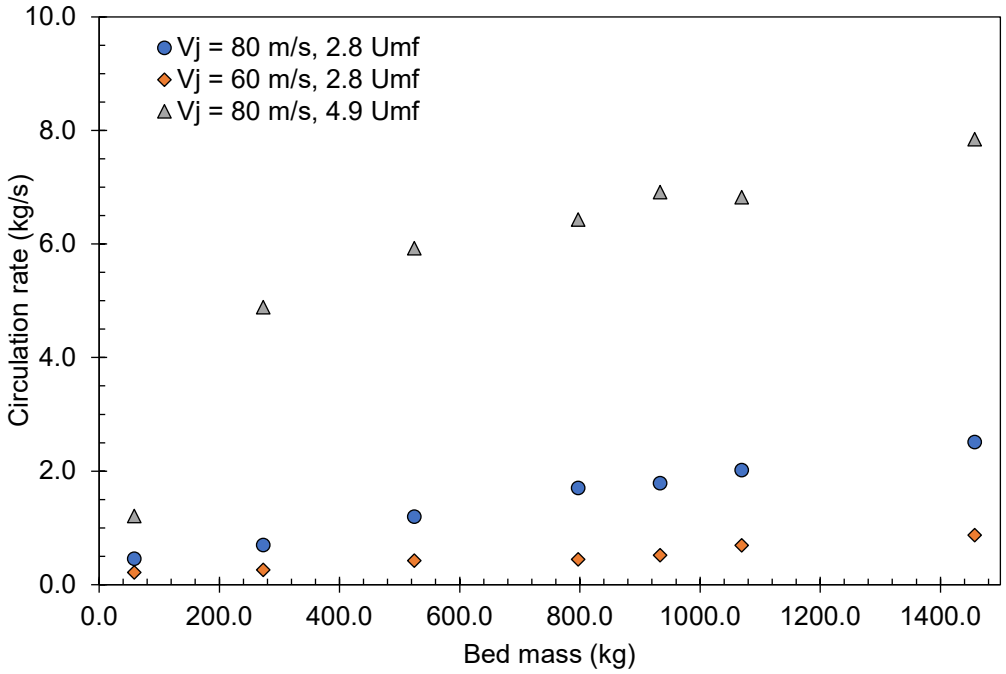

Figure 4-6. Solids circulation rate at varying solids loadings, and operating conditions (P = 101 kPa).

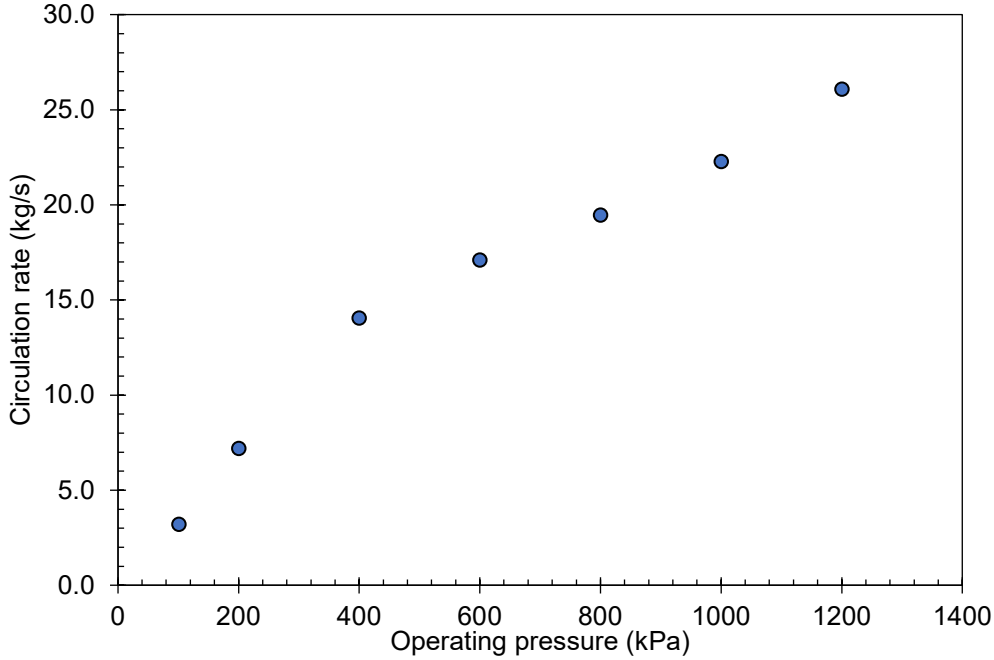

Figure 4-7. Solids circulation rate at varying operating pressures (M_b = 933 kg, 3.5 U_{mf}, V_j = 80 m/s).

The influences of all the operating conditions can be attributed to their respective effects on the rate of fluid momentum entering the system (Eq 4-12). The effects of superficial gas velocity and jet velocity directly impact the rate of fluid momentum entering the system. The influence of bed mass and operating pressure impact the rate of fluid momentum indirectly by affecting the density of the fluidization gas. Increasing

operating pressures directly increase the gas density (Eq 4-13), but for a change in bed mass the gas density changes as a result of the increasing pressure drop through the fluidized bed (Eq 4-14) since the pressure boundary condition is set constant at the top of the vessel. It should be noted that those conditions which had similar momentum rates, resulted in similar circulation rates, regardless of their unique operating conditions demonstrating that the circulation rate is influenced only by the momentum rate and how effectively that horizontal momentum is transferred to the particles.

$$\dot{p}_{in} = \dot{m}_f V_{jet} = A_c \rho_f U V_{jet} \quad [4\text{-}12]$$

$$\rho_{f,bottom} = \frac{MW_{air} P_{bottom}}{RT} = \frac{MW\left(P_{top} + \Delta P_{bed}\right)}{RT} \quad [4\text{-}13]$$

$$\Delta P_{bed} = \rho_f g \Delta H + (1-\varepsilon)(\rho_s - \rho_f) g \Delta H \approx (1-\varepsilon)\rho_s g \Delta H = \frac{M_s g}{A_c} \quad [4\text{-}14]$$

A plot of the entering fluid momentum rate against the particle circulation rate is shown in Figure 4-8 for all simulated cases showing a minimum amount of momentum (approximately 7.8 kg m/s^2) is required to initiate solids circulation. If the momentum rate is below this minimum threshold, circulation will not occur. After circulation begins, the circulation rate transitions between three regimes: 1) a regime in which the circulation rate increases rapidly with increases in momentum rate; 2) a regime of linear increase; and 3) a regime of nonlinear increase in which increasing the momentum rate has a diminishing impact on increasing the circulation rate. These regimes are thought be characterized by how the fluid momentum is transferred to the particles. Low momentum rates dissipate very quickly, forming gas bubbles near the tuyere plate which will not effectively transfer momentum to the solids [31]. Higher momentum rates can form fluid jets which will transfer their momentum more effectively to the solids, inducing higher circulation rates. This phenomenon is visualized in Figure 4-9, where circular regions of low particle volume fraction are formed at the low momentum rates ($< 10\ kg\ m/s^2$), meaning the fluid has not horizontally extended into the bed. At moderately higher momentum rates ($10\ kg\ m/s^2$ to $40\ kg\ m/s^2$) these regions of low particle volume fraction are present throughout the plate, alluding to the formation of horizontal fluid jets that remain distinct from each other. At the highest momentum rates ($> 50\ kg\ m/s^2$) these fluid jets have extended into one another forming large areas of high momentum transfer rates. The diminishing impact of increasing the momentum rates then likely arises from the lower volume of particles near the tuyere plate at higher momentum rates.

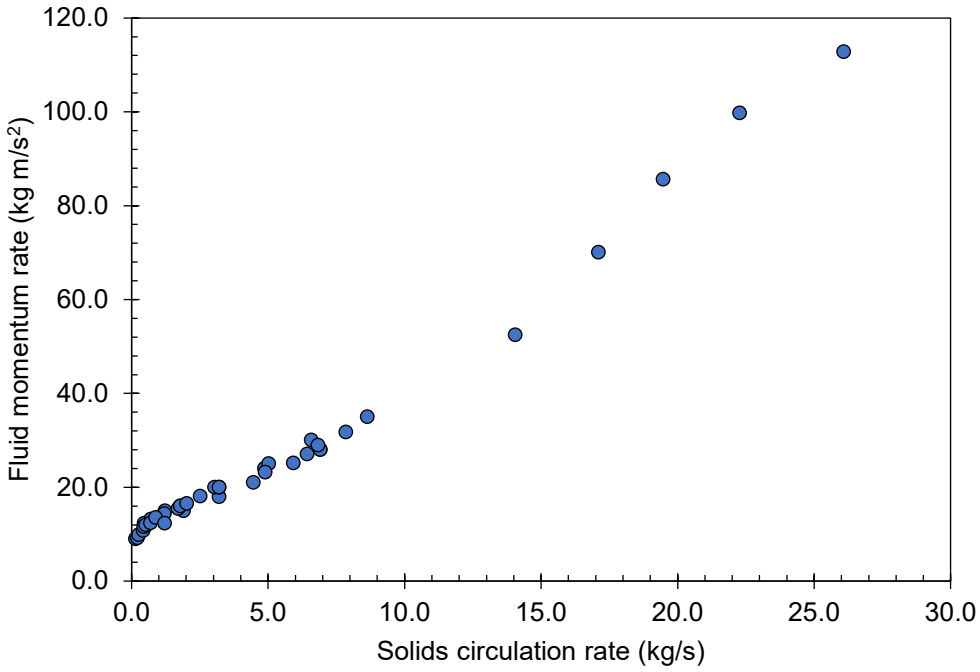

Figure 4-8. Circulation rate as a function of fluid momentum rate.

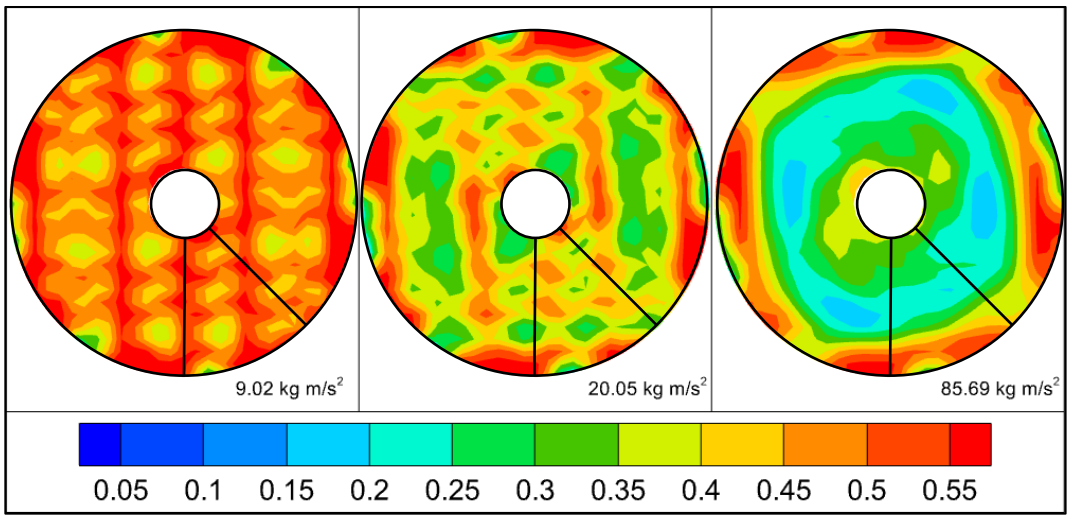

Figure 4-9. Time averaged particle volume fractions at three different momentum rates.

A fourth order polynomial function was fit to the relationship in Figure 4-8 to create a reduced order model relative to the CPFD model to allow for a simple method of predicting the required momentum rate to achieve a desired solids circulation rate. The function is presented in Eq 4-15 and resulted in an $R^2 = 0.998$. It should be noted that this function is only applicable to the range of conditions modeled.

$$\dot{p}_{in} = -9.30 \times 10^{-4} m_s^4 + 4.56 \times 10^{-2} m_s^3 - 6.10 \times 10^{-1} m_s^2 + 5.40 m_s + 7.80 \qquad [4\text{-}15]$$

4.3.2 Gas infiltration

The gas infiltration mass flow rate was found to be correlated to the solids circulation mass flow rate (Figure 4-10). As the solids circulate faster around the PFIR, the infiltration gases trapped in the bed interstitial voids will also circulate faster. The gas volume fraction near the tuyere plate increases with greater circulation rate further increasing the rate of gas infiltration resulting in a non-linear relationship. The large magnitude of the gas infiltration could prove problematic to certain applications, so efforts to mitigate this infiltration at higher circulation rates should be explored. Similar to Eq 4-15, a third order polynomial was fit to the data to create a reduced order model to aid in the prediction of the gas infiltration rate for a desired solids circulation rate. The polynomial is presented in Eq 4-16 and resulted in an R^2 = 0.992. Again, it should be noted that this function is only applicable to the range of conditions modeled.

$$m_{infiltration} = 1.44 \times 10^{-5} m_s^3 - 2.70 \times 10^{-5} m_s^2 + 8.06 \times 10^{-5} m_s \qquad [4\text{-}16]$$

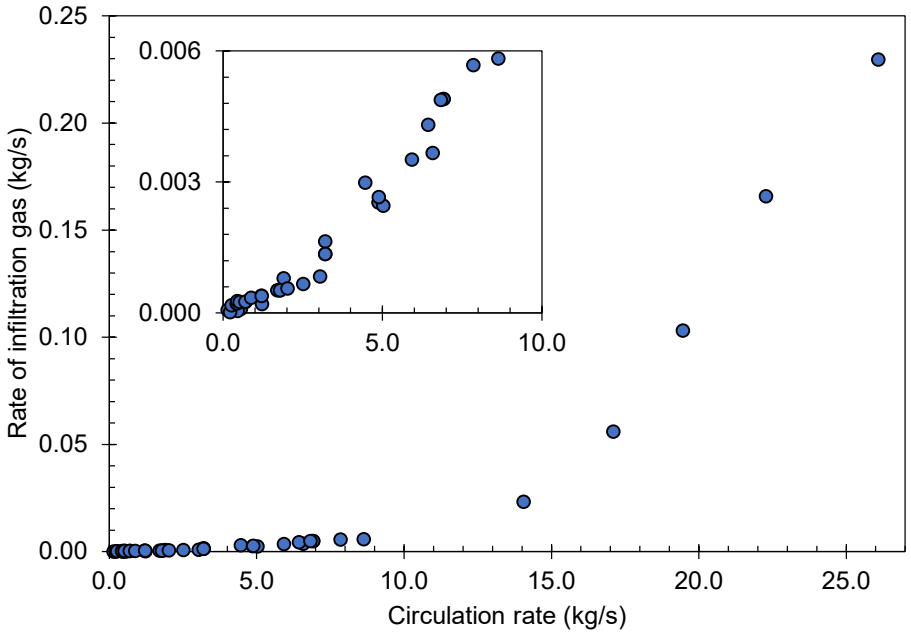

Figure 4-10. Gas infiltration mass flow rate as a function of solids circulation mass flow rate.

4.4 Conclusions

A new reactor geometry was proposed for chemical looping combustion. The PFIR consists of an annular fluidized region in which solids are circulated through two sections separated by baffles using angled tuyere

jets. A CPFD model of the PFIR was created to study the effects of superficial gas velocity, jet velocity, bed mass, and operating pressure on the solids circulation rate and gas infiltration rate between sections.

Solids circulation rate was found to be dependent on the rate of momentum entering through the fluidization gas, resulting in an increasing response of solids circulation rate with all investigated operating variables. Solids circulation was found to only begin when a minimum momentum rate was obtained. A fourth order function was fit to the CPFD data to allow for easier prediction of the required fluid momentum rate needed for a desired circulation rate. The gas infiltration rate was found to be related to the solids circulation flow rate, with more gas passing between reactor sections in the bed interstitial voids. A regression between the solids circulation mass flow rate and the gas infiltration mass flow rate was performed, allowing for a method of predicting the infiltration rate for a required circulation rate. These regressions would allow for more efficient investigation into designing the experimental PFIR unit.

The PFIR is a promising design option for CLC operations demonstrating high solids circulation rates. Further investigation into other important operating factors such as particle residence time distribution, and fluid residence time distributions should be conducted to continue PFIR development. Lastly, cold flow validation is required to confirm the quantitative results of the model.

Acknowledgments

This research was partially sponsored and funded by the Natural Sciences and Engineering Research Council (NSERC) of Canada. This research work was sponsored and partially funded by the Program for Energy Research and Development (PERD) of Natural Resources Canada, Government of Canada. Additional funding was provided by Hatch Ltd. and MITACs through the MITACs Accelerate program. The authors would like to thank Patrick Boisvert from NRCan CanmetENERGY Ottawa for sharing his advice and expertise in CFD modeling towards this work. The authors would also like to thank the staff at Hatch and CPFD Software for their continued help with this project.

References

[1] T. Mendiara, R. Pérez, A. Abad, L.F. De Diego, F. García-Labiano, P. Gayán, J. Adánez, Low-cost Fe-based oxygen carrier materials for the iG-CLC process with coal. 1, Ind. Eng. Chem. Res. 51 (2012) 16216–16229. https://doi.org/10.1021/ie302157y.

[2] T. Mattisson, M. Keller, C. Linderholm, P. Moldenhauer, M. Rydén, H. Leion, A. Lyngfelt, Chemical-looping technologies using circulating fluidized bed systems: Status of development, Fuel Process. Technol. 172 (2018) 1–12. https://doi.org/10.1016/j.fuproc.2017.11.016.

[3] A. Lyngfelt, Chemical Looping Combustion: Status and Development Challenges, Energy & Fuels. 34 (2020) 9077–9093. https://doi.org/10.1021/acs.energyfuels.0c01454.

[4] G.L. Schwebel, D. Filippou, G. Hudon, M. Tworkowski, A. Gipperich, W. Krumm, Experimental comparison of two different ilmenites in fluidized bed and fixed bed chemical-looping combustion, Appl. Energy. 113 (2014) 1902–1908. https://doi.org/10.1016/j.apenergy.2013.07.042.

[5] F.N. Ridha, M.A. Duchesne, X. Lu, D.Y. Lu, D. Filippou, R.W. Hughes, Characterization of an

ilmenite ore for pressurized chemical looping combustion, Appl. Energy. 163 (2016) 323–333. https://doi.org/10.1016/j.apenergy.2015.10.070.

[6] F. Mayer, A.R. Bidwe, A. Schopf, K. Taheri, M. Zieba, G. Scheffknecht, Comparison of a new micaceous iron oxide and ilmenite as oxygen carrier for Chemical looping combustion with respect to syngas conversion, Appl. Energy. 113 (2014) 1863–1868. https://doi.org/10.1016/j.apenergy.2013.04.056.

[7] H. Leion, A. Lyngfelt, M. Johansson, E. Jerndal, T. Mattisson, The use of ilmenite as an oxygen carrier in chemical-looping combustion, Chem. Eng. Res. Des. 86 (2008) 1017–1026. https://doi.org/10.1016/j.cherd.2008.03.019.

[8] A. Cuadrat, A. Abad, J. Adánez, L.F. De Diego, F. García-Labiano, P. Gayán, Behavior of ilmenite as oxygen carrier in chemical-looping combustion, Fuel Process. Technol. 94 (2012) 101–112. https://doi.org/10.1016/j.fuproc.2011.10.020.

[9] N. Berguerand, A. Lyngfelt, Design and operation of a 10 kWth chemical-looping combustor for solid fuels - Testing with South African coal, Fuel. 87 (2008) 2713–2726. https://doi.org/10.1016/j.fuel.2008.03.008.

[10] A. Cabello, R.W. Hughes, R.T. Symonds, S. Champagne, D.Y. Lu, E. Mostafavi, N. Manihpey, Economic Analysis of Pressurized Chemical Looping Combustion for SAGD Application, in: 5th Int. Conf. Chem. Looping, Park City, Utah, USA, 2018.

[11] R.T. Symonds, R.W. Hughes, D.Y. Lu, P. Navarri, O. Ashrafi, Systems analysis of pressurized chemical looping combustion for SAGD applications, Int. J. Greenh. Gas Control. 73 (2018) 111–123. https://doi.org/10.1016/j.ijggc.2018.03.008.

[12] J. Wolf, CO2 Mitigation in Advanced Power Cycles - Chemical Looping Combustion and Steam-Based Gasification, KTH Royal Institute of Technology, 2004.

[13] A. Nandy, C. Loha, S. Gu, P. Sarkar, M.K. Karmakar, P.K. Chatterjee, Present status and overview of Chemical Looping Combustion technology, Renew. Sustain. Energy Rev. 59 (2016) 597–619. https://doi.org/10.1016/j.rser.2016.01.003.

[14] J. Adanez, A. Abad, F. Garcia-Labiano, P. Gayan, L.F. De Diego, Progress in chemical-looping combustion and reforming technologies, Prog. Energy Combust. Sci. (2012). https://doi.org/10.1016/j.pecs.2011.09.001.

[15] B. Kronberger, E. Johansson, G. Löffer, T. Mattisson, A. Lyngfelt, H. Hofbauer, A two-compartment fluidized bed reactor for CO2 capture by chemical-looping combustion, Chem. Eng. Technol. 27 (2004) 1318–1326. https://doi.org/10.1002/ceat.200402137.

[16] B. Kronberger, A. Lyngfelt, G. Löffler, H. Hofbauer, Design and fluid dynamic analysis of a bench-scale combustion system with CO2 separation-chemical-looping combustion, Ind. Eng. Chem. Res. 44 (2005) 546–556. https://doi.org/10.1021/ie049670u.

[17] E. Johansson, A. Lyngfelt, T. Mattisson, F. Johnsson, Gas leakage measurements in a cold model of an interconnected fluidized bed for chemical-looping combustion, Powder Technol. 134 (2003) 210–217. https://doi.org/10.1016/S0032-5910(03)00125-6.

[18] P. Kolbitsch, T. Pröll, J. Bolhar-Nordenkampf, H. Hofbauer, Design of a chemical looping combustor using a dual circulating fluidized bed reactor system, Chem. Eng. Technol. 32 (2009) 398–403. https://doi.org/10.1002/ceat.200800378.

[19] H.R. Kim, D. Wang, L. Zeng, S. Bayham, A. Tong, E. Chung, M. V. Kathe, S. Luo, O. McGiveron, A. Wang, Z. Sun, D. Chen, L.S. Fan, Coal direct chemical looping combustion process: Design and operation of a 25-kWth sub-pilot unit, Fuel. 108 (2013) 370–384.

https://doi.org/10.1016/j.fuel.2012.12.038.

[20] J. Ströhle, M. Orth, B. Epple, Design and operation of a 1MWth chemical looping plant, Appl. Energy. 113 (2014) 1490–1495. https://doi.org/10.1016/j.apenergy.2013.09.008.

[21] A. Lyngfelt, C. Linderholm, Chemical-looping combustion of solid fuels - Technology overview and recent operational results in 100 kW unit, Energy Procedia. 63 (2014) 98–112. https://doi.org/10.1016/j.egypro.2014.11.011.

[22] I. Ahmed, H. De Lasa, CO2 Capture Using Chemical Looping Combustion from a Biomass-Derived Syngas Feedstock: Simulation of a Riser-Downer Scaled-Up Unit, Ind. Eng. Chem. Res. 59 (2020) 6900–6913. https://doi.org/10.1021/acs.iecr.9b05753.

[23] S. Noorman, M. Van Sint Annaland, H. Kuipers, Packed bed reactor technology for chemical-looping combustion, Ind. Eng. Chem. Res. 46 (2007) 4212–4220. https://doi.org/10.1021/ie061178i.

[24] S. Noorman, M. van Sint Annaland, J.A.M. Kuipers, Experimental validation of packed bed chemical-looping combustion, Chem. Eng. Sci. 65 (2010) 92–97. https://doi.org/10.1016/j.ces.2009.02.004.

[25] C. Chen, G.M. Bollas, Optimal design of combined cycle power plants with fixed-bed chemical-looping combustion reactors, AIChE J. 65 (2019). https://doi.org/10.1002/aic.16516.

[26] L. Han, G.M. Bollas, Dynamic optimization of fixed bed chemical-looping combustion processes, Energy. 112 (2016) 1107–1119. https://doi.org/10.1016/j.energy.2016.07.031.

[27] I.M. Dahl, E. Bakken, Y. Larring, A.I. Spjelkavik, S.F. Håkonsen, R. Blom, On the development of novel reactor concepts for chemical looping combustion, Energy Procedia. 1 (2009) 1513–1519. https://doi.org/10.1016/j.egypro.2009.01.198.

[28] S.F. Håkonsen, C.A. Grande, R. Blom, Rotating bed reactor for CLC: Bed characteristics dependencies on internal gas mixing, Appl. Energy. 113 (2014) 1952–1957. https://doi.org/10.1016/j.apenergy.2013.04.044.

[29] L.S. Fan, L. Zeng, S. Luo, Chemical-Looping Technology Platform, AIChE J. 59 (2015) 215–228. https://doi.org/10.1002/aic.

[30] L.S. Fan, L. Zeng, W. Wang, S. Luo, Chemical looping processes for CO2 capture and carbonaceous fuel conversion - Prospect and opportunity, Energy Environ. Sci. 5 (2012) 7254–7280. https://doi.org/10.1039/c2ee03198a.

[31] J.R. Grace, R. Di Felice, A. Di Renzo, X. Bi, N. Ellis, T. Li, Y. Xu, F. Fotovat, T.M. Knowlton, S. Reddy Karri, C. Wang, J. Zhu, P. Mehrani, A. Sowinski, D.E. Jia, A. Machecha-Botero, J. Shabanian, J. Chaouki, Y. Zhang, C. Briend, J. McMillan, C. Wu, Y. Cheng, N. Epstien, D. Pjontek, A. Donaldson, A. Macchi, Essentials of Fluidization Technology, 1st ed., Wiley-VCH, Weinheim, Germanu, 2020. https://doi.org/10.1002/9783527699483.

[32] F. Zerobin, S. Penthor, O. Bertsch, T. Pröll, Fluidized bed reactor design study for pressurized chemical looping combustion of natural gas, Powder Technol. 316 (2017) 569–577. https://doi.org/10.1016/j.powtec.2017.02.001.

[33] J. Adanez, A. Abad, F. Garcia-Labiano, P. Gayan, L.F. De Diego, Progress in chemical-looping combustion and reforming technologies, Prog. Energy Combust. Sci. 38 (2012) 215–282. https://doi.org/10.1016/j.pecs.2011.09.001.

[34] K. Adham, C. Harris, A. Kokourine, Plug Flow Reactor with Internal Recirculation Fluidized Bed, CA2951724, 2015.

[35] K. Adham, C. Harris, A. Kokourine, Modeling and Process Features of Plug Flow Reactor with

Internal Recirculation for Biomass Pyrolysis, J. Chem. Eng. Process Technol. 08 (2017) 353. https://doi.org/10.4172/2157-7048.1000353.

[36] Y. Shao, J. Gu, W. Zhong, A. Yu, Determination of minimum fluidization velocity in fluidized bed at elevated pressures and temperatures using CFD simulations, Powder Technol. 350 (2019) 81–90. https://doi.org/10.1016/j.powtec.2019.03.039.

[37] S. Karimipour, T. Pugsley, Application of the particle in cell approach for the simulation of bubbling fluidized beds of Geldart A particles, Powder Technol. 220 (2012) 63–69. https://doi.org/10.1016/j.powtec.2011.09.026.

[38] W. S. Amarasinghe, C. K. Jayarathna, B. S. Ahangama, B. M. E. Moldestad, L.-A. Tokheim, Experimental Study and CFD Modelling of Minimum Fluidization Velocity for Geldart A, B and D Particles, Int. J. Model. Optim. 7 (2017) 152–156. https://doi.org/10.7763/ijmo.2017.v7.575.

[39] C. Jayarathna, B. Moldestad, L.-A. Tokheima, Validation of results from Barracuda CFD modelling to predict the minimum fluidization velocity and the pressure drop of Geldart A particles, Proc. 58th Conf. Simul. Model. (SIMS 58) Reykjavik, Iceland, Sept. 25th – 27th, 2017. 138 (2017) 76–82. https://doi.org/10.3384/ecp1713876.

[40] F. Fotovat, A. Abbasi, R.J. Spiteri, H. de Lasa, J. Chaouki, A CPFD model for a bubbly biomass-sand fluidized bed, Powder Technol. 275 (2015) 39–50. https://doi.org/10.1016/j.powtec.2015.01.005.

[41] S. Vashisth, A.H. Ahmadi Motlagh, S. Tebianian, M. Salcudean, J.R. Grace, Comparison of numerical approaches to model FCC particles in gas-solid bubbling fluidized bed, Chem. Eng. Sci. 134 (2015) 269–286. https://doi.org/10.1016/j.ces.2015.05.001.

[42] Y. Zhang, Q. Wei, CPFD simulation of bed-to-wall heat transfer in a gas-solids bubbling fluidized bed with an immersed vertical tube, Chem. Eng. Process. - Process Intensif. 116 (2017) 17–28. https://doi.org/10.1016/j.cep.2017.03.007.

[43] J.M. Weber, K.J. Layfield, D.T. Van Essendelft, J.S. Mei, Fluid bed characterization using electrical capacitance volume tomography (ECVT), compared to CPFD software's barracuda, Powder Technol. 250 (2013) 138–146. https://doi.org/10.1016/j.powtec.2013.10.005.

[44] H.C. Park, H.S. Choi, Numerical study of the segregation of pyrolized char in a bubbling fluidized bed according to distributor configuration, Powder Technol. 355 (2019) 637–648. https://doi.org/10.1016/j.powtec.2019.07.084.

[45] C.B. Solnordal, V. Kenche, T.D. Hadley, Y. Feng, P.J. Witt, K.S. Lim, Simulation of an internally circulating fluidized bed using a multiphase particle-in-cell method, Powder Technol. 274 (2015) 123–134. https://doi.org/10.1016/j.powtec.2014.12.045.

[46] X. Shi, X. Lan, F. Liu, Y. Zhang, J. Gao, Effect of particle size distribution on hydrodynamics and solids back-mixing in CFB risers using CPFD simulation, Powder Technol. 266 (2014) 135–143. https://doi.org/10.1016/j.powtec.2014.06.025.

[47] X. Shi, R. Sun, X. Lan, F. Liu, Y. Zhang, J. Gao, CPFD simulation of solids residence time and back-mixing in CFB risers, Powder Technol. 271 (2015) 16–25. https://doi.org/10.1016/j.powtec.2014.11.011.

[48] Q. Wang, T. Niemi, J. Peltola, S. Kallio, H. Yang, J. Lu, L. Wei, Particle size distribution in CPFD modeling of gas-solid flows in a CFB riser, Particuology. 21 (2015) 107–117. https://doi.org/10.1016/j.partic.2014.06.009.

[49] Y. Zhang, F. Lei, S. Wang, X. Xu, Y. Xiao, A numerical study of gas-solid flow hydrodynamics in a riser under dense suspension upflow regime, Powder Technol. 280 (2015) 227–238.

https://doi.org/10.1016/j.powtec.2015.04.061.

[50] M. Nakhaei, C.E. Hessel, H. Wu, D. Grévain, S. Zakrzewski, L.S. Jensen, P. Glarborg, K. Dam-Johansen, Experimental and CPFD study of gas–solid flow in a cold pilot calciner, Powder Technol. 340 (2018) 99–115. https://doi.org/10.1016/j.powtec.2018.09.008.

[51] A. Lanza, M.A. Islam, H. de Lasa, Particle clusters and drag coefficients in gas-solid downer units, Chem. Eng. J. 200–202 (2012) 439–451. https://doi.org/10.1016/j.cej.2012.06.027.

[52] Q. Wang, H. Yang, P. Wang, J. Lu, Q. Liu, H. Zhang, L. Wei, M. Zhang, Application of CPFD method in the simulation of a circulating fluidized bed with a loop seal, part I-Determination of modeling parameters, Powder Technol. 253 (2014) 814–821. https://doi.org/10.1016/j.powtec.2013.11.041.

[53] Q. Wang, H. Yang, P. Wang, J. Lu, Q. Liu, H. Zhang, L. Wei, M. Zhang, Application of CPFD method in the simulation of a circulating fluidized bed with a loop seal Part II-Investigation of solids circulation, Powder Technol. 253 (2014) 822–828. https://doi.org/10.1016/j.powtec.2013.11.040.

[54] Q. Ma, F. Lei, Y. Xiao, Numerical analysis of operating conditions for establishing high-density circulating fluidized bed by CPFD method, Powder Technol. 338 (2018) 446–457. https://doi.org/10.1016/j.powtec.2018.07.012.

[55] Q. Tu, H. Wang, CPFD study of a full-loop three-dimensional pilot-scale circulating fluidized bed based on EMMS drag model, Powder Technol. 323 (2018) 534–547. https://doi.org/10.1016/j.powtec.2017.09.045.

[56] Y. Wu, L. Peng, L. Qin, M. Wang, J. Gao, X. Lan, Validation and application of CPFD models in simulating hydrodynamics and reactions in riser reactor with Geldart A particles, Powder Technol. 323 (2018) 269–283. https://doi.org/10.1016/j.powtec.2017.10.003.

[57] J.M. Parker, CFD model for the simulation of chemical looping combustion, Powder Technol. 265 (2014) 47–53. https://doi.org/10.1016/j.powtec.2014.01.027.

[58] J. Gu, Y. Shao, X. Liu, W. Zhong, A. Yu, Modelling of particle flow in a dual circulation fluidized bed by a Eulerian-Lagrangian approach, Powder Technol. 323 (2018) 433–447. https://doi.org/10.1016/j.ces.2018.08.008.

[59] M.A. Hamilton, K.J. Whitty, J.A.S. Lighty, Numerical simulation comparison of two reactor configurations for chemical looping combustion and chemical looping with oxygen uncoupling, J. Energy Resour. Technol. Trans. ASME. 138 (2016) 1–9. https://doi.org/10.1115/1.4033108.

[60] S. Kraft, F. Kirnbauer, H. Hofbauer, CPFD simulations of an industrial-sized dual fluidized bed steam gasification system of biomass with 8 MW fuel input, Appl. Energy. 190 (2017) 408–420. https://doi.org/10.1016/j.apenergy.2016.12.113.

[61] D.M. Snider, An Incompressible Three-Dimensional Multiphase Particle-in-Cell Model for Dense Particle Flows, J. Comput. Phys. 170 (2001) 523–549. https://doi.org/10.1006/jcph.2001.6747.

[62] D.M. Snider, P.J. O'Rourke, The Multiphase Particle In Cell (MP-PIC) Method for Dense Particle Flow, in: S. Pannala, M. Syamlal, T.J. O'Brien (Eds.), Comput. Gas-Solids Flows React. Syst. Theory, Methods, Pract., 1st ed., IGI Global, Hershey, PA, 2011. https://doi.org/10.1017/CBO9781107415324.004.

[63] M. J. Andrews and P.J. O'Rourke, The Multiphase Particle-in-Cell (MP-PIC) Method for Dense Particulate Flows, Int J Multiph. Flow. 22 (1996) 379–402.

[64] S.E. Harris, D.G. Crighton, Solitons, solitary waves, and voidage disturbances in gas-fluidized beds, J. Fluid Mech. 266 (1994) 243–276. https://doi.org/10.1017/S0022112094000996.

[65] C.J. McIntyre, CPFD Modeling of Novel Internally Circulating Bubbling Fluidized Bed for Chemical Looping Combustion, University of Ottawa, 2021.

Chapter 5 Conclusions and Recommendations

With rising greenhouse gas emissions increasing its severity and pace, new technologies must be implemented to mitigate the effects of climate change. PCLC is a relatively new carbon capture technology that has the potential to limit industrial CO_2 emissions from contributing to the greenhouse effect. The aim of this thesis was to provide key design parameters and insight for the development of a PCLC pilot scale system by CanmetENERGY-Ottawa (Ottawa, Ontario, Canada) and Hatch Ltd. (Mississauga, Ontario, Canada). This pilot facility implements the patented Plug Flow Internally-circulating Reactor (PFIR) concept to reduce capital and operating costs of the PCLC process, and ilmenite as the oxygen carrier. Specifically, this thesis provided information about the hydrodynamics and tube-to-bed heat transfer coefficient of ilmenite, explored the applicability of the CPFD modeling technique to high pressure bubbling fluidized beds, and used a CPFD model to investigate the solids circulation rate and gas infiltration in the PFIR.

A pilot scale high pressure fluidized bed was used to experimentally derive the minimum fluidization velocity, gas bubble characteristics, and tube-to-bed heat transfer coefficient of ilmenite at pressures up to 2000 kPa and various superficial gas velocities. The minimum fluidization velocities were compared to predictions of various literature constants for the Wen-Yu type correlation. The constants proposed by Saxena & Vogel [1] were found to align best with the smaller particles (Sauter mean less than 109 μm), while the the Chistester *et al.* [2] constants aligned best with the larger particle results (Sauter mean greater than 236 μm). The predictive nature of literature correlations was found to be heavily dependent on the shape-void function, and by extension the values of particle sphericity and bed voidage at minimum fluidization. The inconsistency between the small and large particle size distributions results from the difference in the voidage at minimum fluidization, with the small and large particles having void fractions of 0.50 and 0.47 at minimum fluidization, respectively. The gas bubble size was determined for the particles of 107 μm Sauter mean diameter at pressures of 101 kPa, 600 kPa, and 1200 kPa, and various superficial gas velocities between $1.1U_{mf}$ and $3.0U_{mf}$. Pressure was to marginally impact the gas bubble size relative to the superficial gas velocity. A comparison of literature correlations showed that the Mori & Wen [3] correlation aligned best with the experimental values. A similar response in pressure for the tube-to-bed heat transfer coefficient was found, with increasing pressure resulting in a marginal increase in the heat transfer coefficient. The heat transfer coefficient was also found to experience a maximum with superficial gas velocity. Comparing the experimental results to the Molerus *et al.* [4] and Grewal & Saxena [5] correlations resulted in general overpredictions, but the Molerus *et al.* [4] aligned well with atmospheric values.

The experimental results were used to validate a CPFD model of the high pressure fluidized bed. The model was created using the commercially available software Barracuda Virtual Reactor ® and validated against the experimental values for minimum fluidization velocity, bed expansion, and gas bubble size. The accuracy of the model at predicting minimum fluidization velocity was found to be dependent on the input value of the particle close packing factor. An analysis of different close packing factors ranging from 0.55 – 0.6 resulted in a value of 0.58 aligning well for all the simulated particle size distributions. A study of the bed expansion showed the model was able to properly predict the trends in bed expansion with increasing superficial gas velocity and pressure, but with a consistent under prediction of the experimental values. The validated model was also used to expand upon the experimental results by determining the gas bubble size distribution at various operating pressures, superficial gas velocities, and axial locations. The calculated mean bubble size from the distributions aligned well with experimental results and expected trends. A comparison of the axial bubble growth in the simulated column and the predicted bubble size growth by the Mori & Wen [3] correlation concluded that the correlation could be used with moderate accuracy to predict the mean bubble size; however, modification of the supporting correlations for initial and maximum bubble size is required.

The validated parameters of the above CPFD model were used in a model of a proposed cold flow PFIR experimental unit. The model was used to explore the effects of superficial gas velocity, tuyere jet velocity, bed height, and operating pressure. An increase of a given operating variable was found to increase the solids circulation rate due to their respective increases on the rate of fluid momentum. This relationship allowed for the creating of a design correlation between the entering fluid momentum rate and desired solids circulation. The rate of gas infiltration was found to be correlated to the rate of solids circulation due to gas carryover in the bed interstitial voids. Another correlation was determined to predict the rate of gas infiltration for a given solids circulation rate. The correlations should only be used in the range of modeled parameters (momentum rates between 9 and 113 kg m/s^2).

Overall, the results obtained in this work provided key design parameters for the PCLC pilot scale facility, presented a validation of CPFD as a design tool, and gave methods for predicting the required operating conditions for a desired solids circulation rate and the corresponding gas infiltration rate. Direct validation of the PFIR CPFD model is recommended using the cold flow PFIR unit once constructed. The modeling effort can be furthered by including reaction modeling of the PCLC system to the CPFD modeling using ilmenite as the oxygen carrier, and potentially other promising oxygen carrier candidates. Lastly, the pilot scale facility should continue with construction to further demonstrate the benefits of the PFIR, and PCLC on a large scale, as well as validate a hot flow CPFD model and allow for validated commercial scale simulations.

References

[1] J. Grace, Fluidized Bed Hydrodynamics, in: Handb. Multiph. Flow, McGraw-Hill, Washington,DC, 1982: p. 970.

[2] D.C. Chitester, R.M. Kornosky, L.S. Fan, J.P. Danko, Characteristics of fluidization at high pressure, Chem. Eng. Sci. (1984). https://doi.org/10.1016/0009-2509(84)80025-1.

[3] S. Mori, C.Y. Wen, Estimation of bubble diameter in gaseous fluidized beds, AIChE J. 21 (1975) 109–115. https://doi.org/10.1002/aic.690210114.

[4] O. Molerus, A. Burschka, S. Dietz, Particle migration at solid surfaces and heat transfer in bubbling fluidized beds-I. Particle migration measurement systems, Chem. Eng. Sci. 50 (1995) 871–877. https://doi.org/10.1016/0009-2509(94)00445-W.

[5] N.S. Grewal, S.C. Saxena, Heat transfer between a horizontal tube and a gas-solid fluidized bed, Int. J. Heat Mass Transf. 23 (1980) 1505–1519. https://doi.org/10.1016/0017-9310(80)90154-4.

Appendix A Experimental Apparatus

The high pressure fluidized bed system is housed at the University of Ottawa in the Chemical and Biological Engineering Undergraduate Laboratory. The unit consists of two parts: the column with auxiliary systems and an insertable tube bundle for heat transfer measurements. The following are pictures of the apparatus.

Figure A-1. Profile of the high pressure fluid bed column

Figure A-2. Close up view of distributor plate hole arrangement

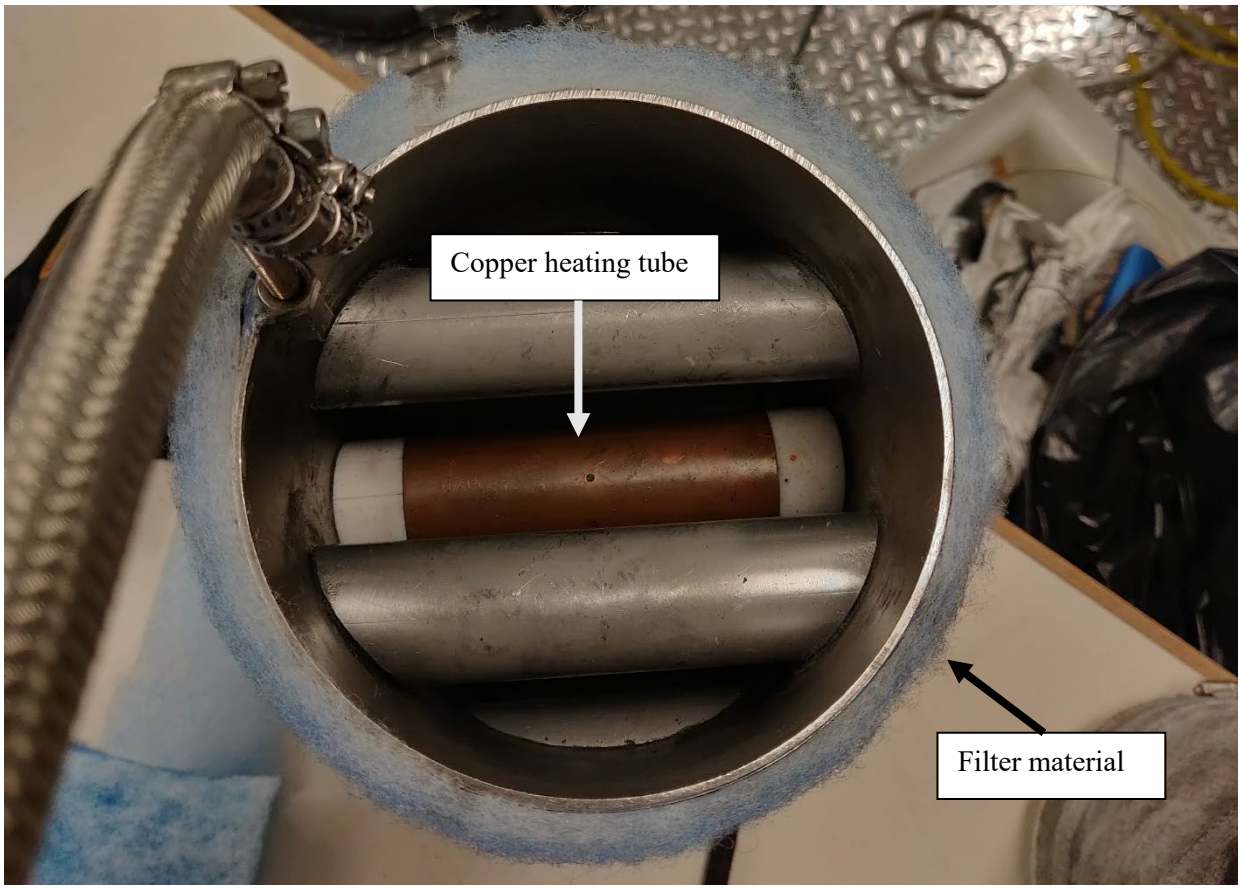

Figure A-3. Top view of insertable tube bank with copper heating tube visible. Filter material was used to seal the small gap between tube sleeve and column wall

Figure A-4. Side view of insertable tube bank apparatus

Appendix B High Pressure CPFD Model

The high pressure CPFD model modeled half the empty column with a flow boundary condition at the distributor plate and a pressure boundary condition at the top of the volume. Only half the column was modeled (1.5m) since the static bed height was a maximum of 0.5m and the superficial gas velocity was controlled to remain in the bubbling bed regime.

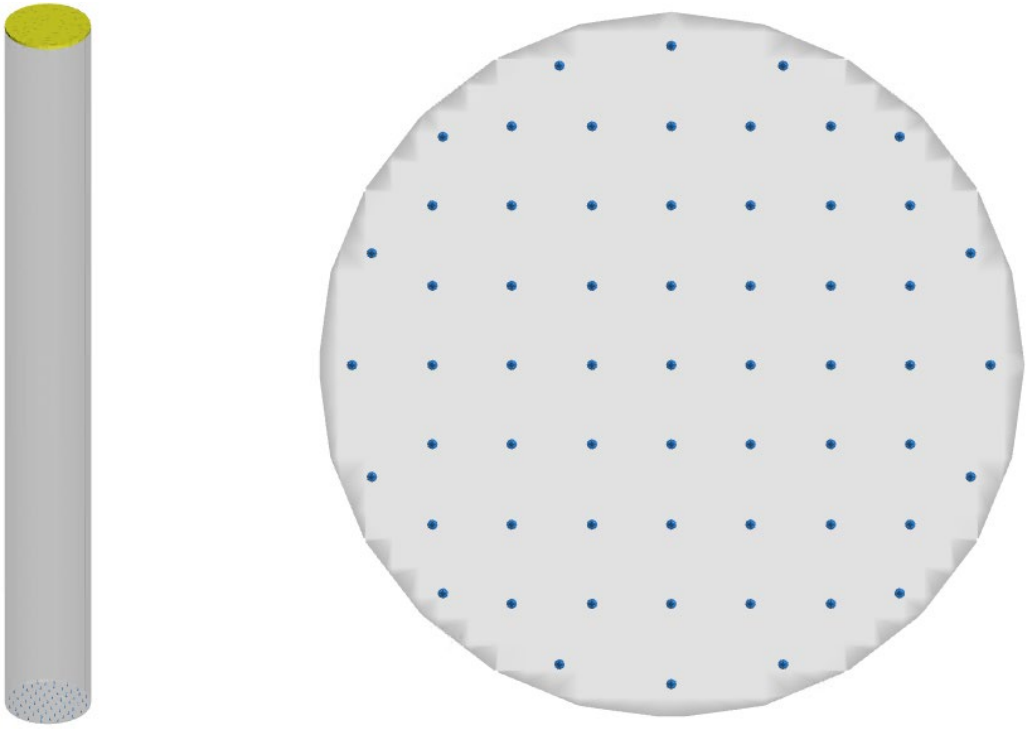

Figure B-1. Boundary conditions for the high pressure fluidized bed model. Yellow area is pressure boundary conditions; blue dots are vertical directional inject points at distributor hole locations

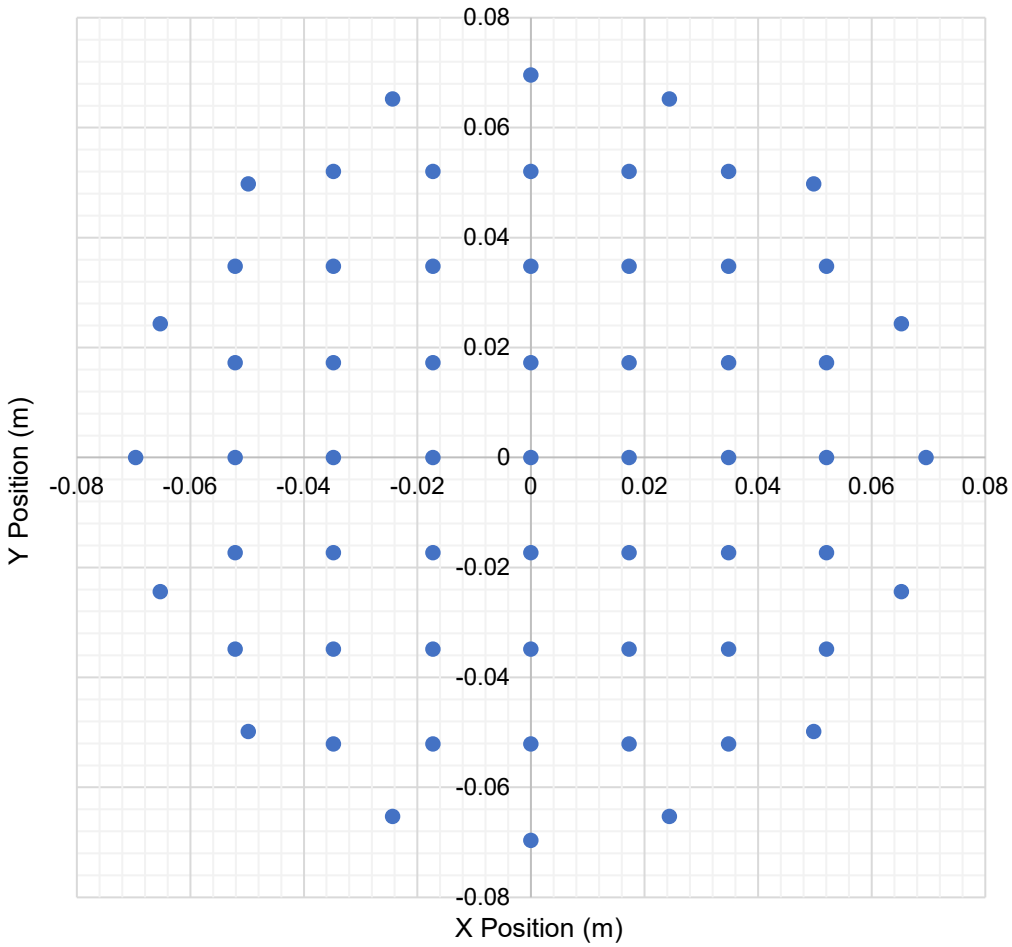

Figure B-2. X and Y positions of distributor plate injection points. Origin runs through center line of column

Appendix C PFIR CPFD Model

The PFIR CPFD model is based on a proposed design for a cold flow PFIR experimental unit. The flow boundary conditions are the fluid injection points. Separate injection points are defined for the fuel and air reactors to provide separate control of flow rates. The following describes how the model was setup, and how the circulation rate and gas infiltration rate were determined.

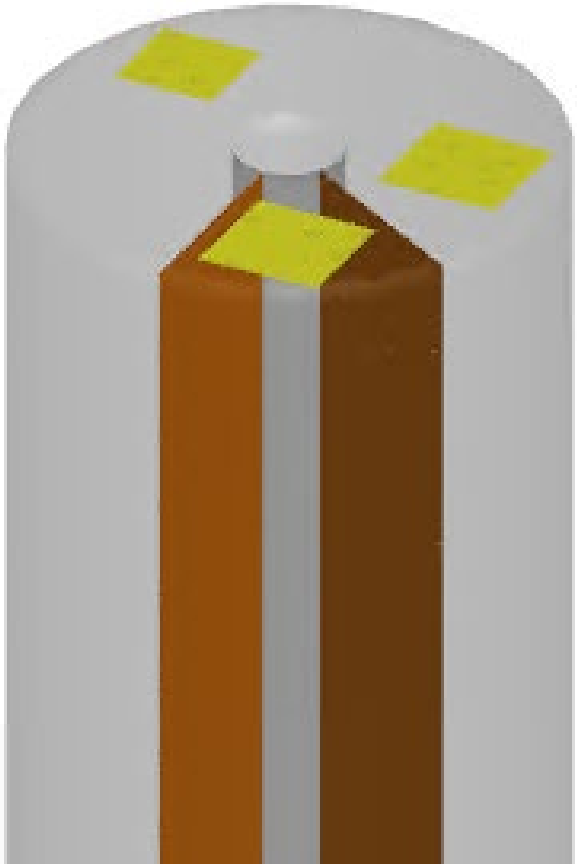

Figure C-1. Pressure boundary conditions: two in the air reactor, one in the fuel reactor. Note pressure values are the same at each location

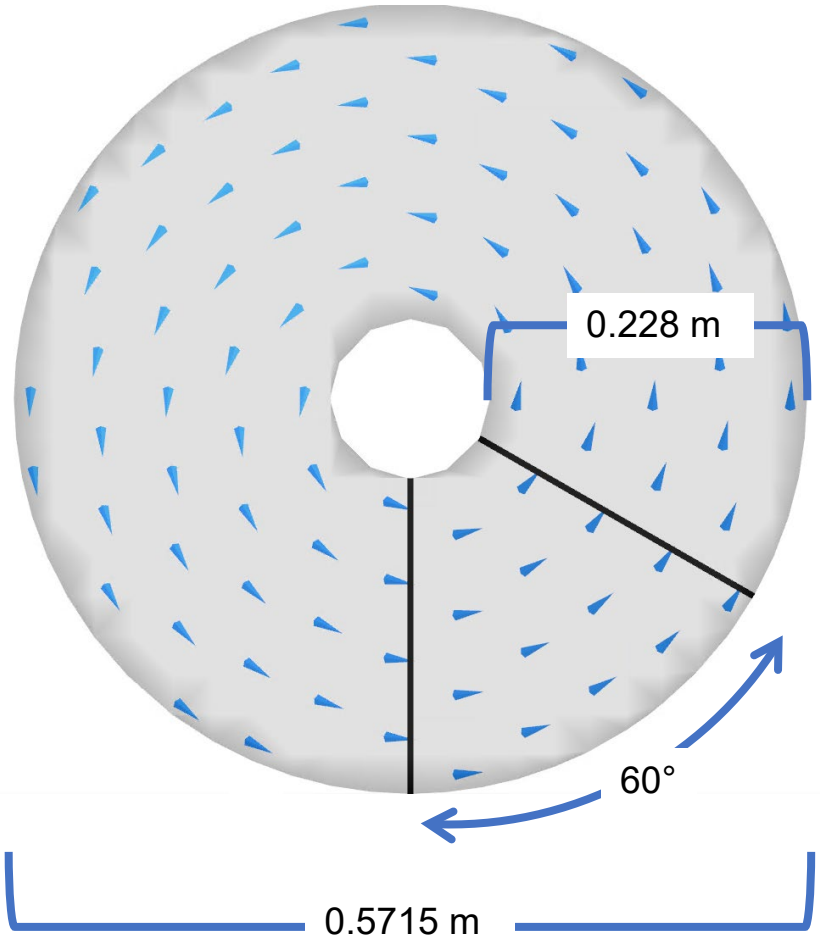

Figure C-2. Dimensions of PFIR cold flow CPFD model

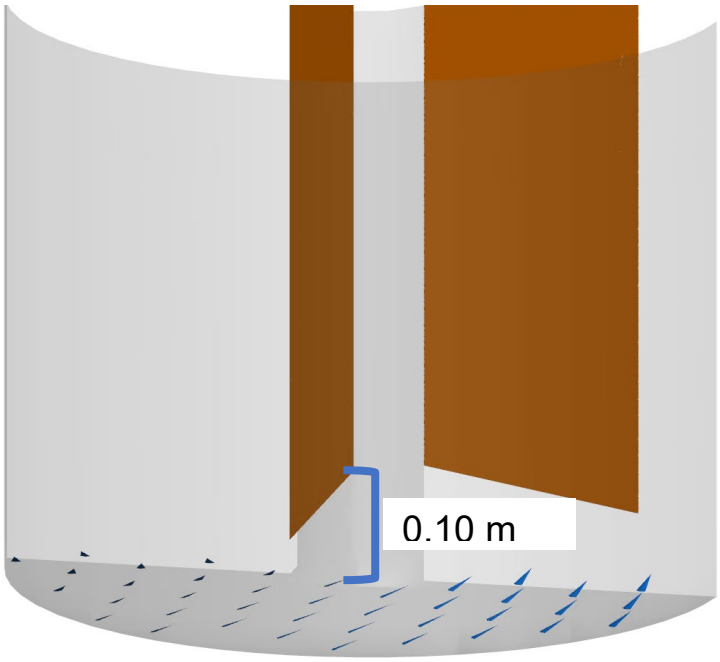

Figure C-3. Slot height of PFIR cold flow CPFD model

The circulation rate is defined as the amount of particle mass per unit time that rotates around the annulus of the reactor. It is measured through four flux planes inside the calculation volume located on the each of the cartesian axes (Positive X, Positive Y, Negative X, and Negative Y) – see Figure C-4. The planes cover the entirety of the fluid bed height.

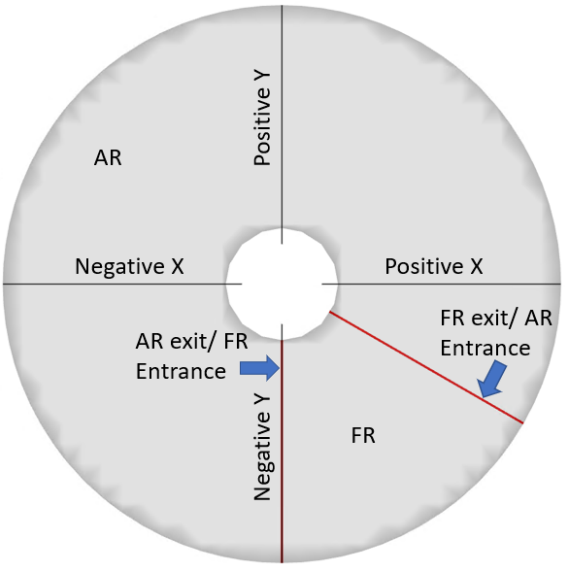

Figure C-4. Location of axis flux planes for measuring solids circulation rate

The time integrated particle mass vs simulation time is measured directly, which records the net cumulative amount of mass crossing the plane's location. If mass travels in the positive direction (relative to the X or Y axes) then the net cumulative amount of mass crossing the plane increases, and vice versa.

To obtain the single value input, the slope of the time integrated mass vs time is taken to obtain the mass flow rate of particles crossing a given plane (Figure C-5). This action is performed for each of the four axis planes. An average is taken of the absolute values of mass flow rate to obtain the single value output. An absolute value is needed since two planes will have negative mass flows due to the direction of particle flow.

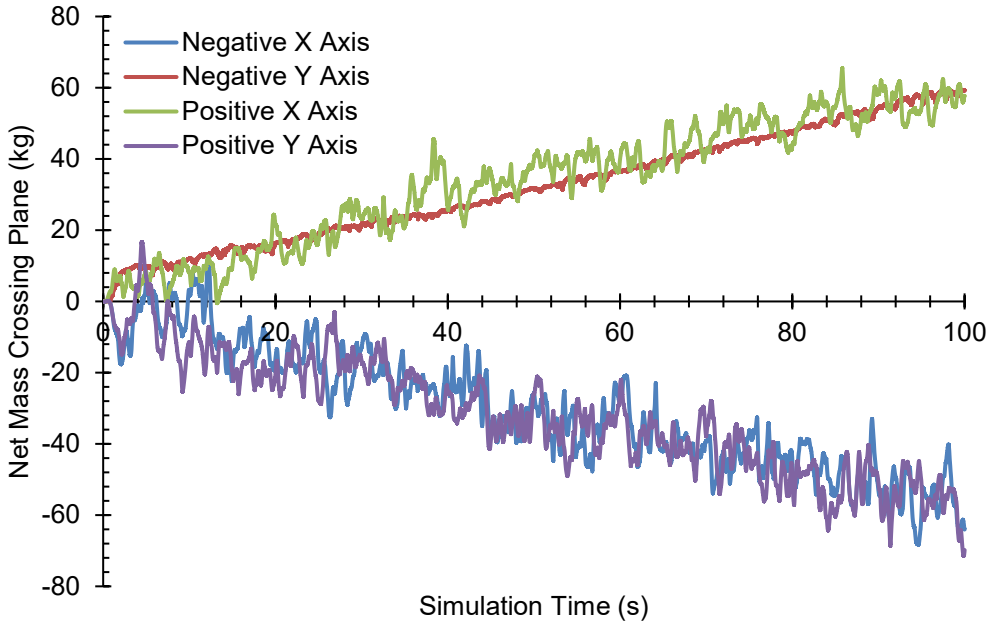

Figure C-5. Example of raw data produced by flux plane.

The rate of infiltration gas is measured from the FR entrance weir (Figure C-6). There is one flux plane that covers the underflow slot opening into the FR. The infiltration rate is calculated by taking the slope of the time integrated fluid mass crossing the plane vs time. Note, the air originating in the air reactor or fuel reactor sections are distinguishable from each other by the fact the model set up considers these two different species of air with identical properties. The air used differs only in name allowing for the separation to be determined in post processing.

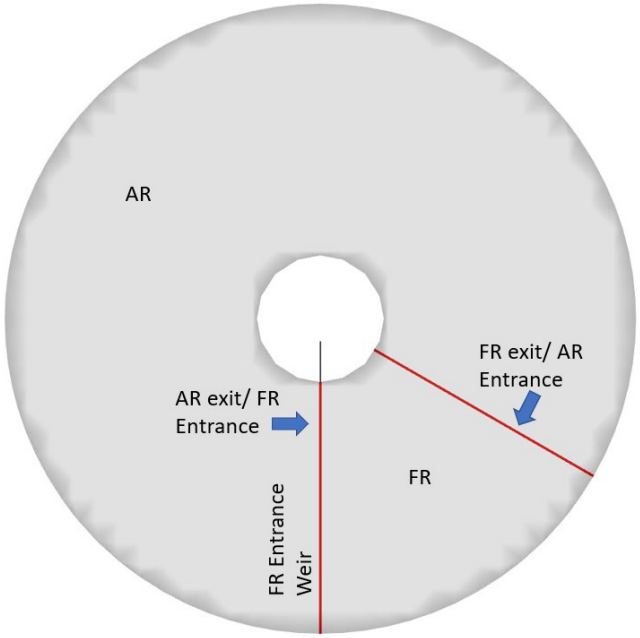

Figure C-6. Placement of the FR entrance (AR Exit) flux plane